University of Alberta

Using Nano-materials to Catalyze Magnesium Hydride for Hydrogen Storage

by

Babak Shalchi Amirkhiz

A thesis submitted to the Faculty of Graduate Studies and Research
in partial fulfillment of the requirements for the degree of

Doctor of Philosophy

in Materials Engineering

Department of Chemical and Materials Engineering

Spring 2011
Edmonton, Alberta

Dedication

To my mother Azita and my father Maghsoud; to my siblings Shahryar, Kaveh, Ghazaleh and Arian.
To the love of my life Laleh.

Abstract

We have designed and engineered bi-catalyst magnesium hydride composites with superior sorption performance to that of ball milled magnesium hydride catalyzed with the individual baseline catalysts. We have examined the effect of single-walled carbon nanotube (SWCNT)-metallic nanoparticle additions on the hydrogen desorption behavior of MgH_2 after high-energy co-milling. We showed the synergy between SWCNT's and metallic nanoparticles in catalyzing the sorption of magnesium hydride. The optimum microstructure for sorption, obtained after 1 h of co-milling, consists of highly defective SWCNTs in intimate contact with metallic nanoparticles and with the hydride. This microstructure is optimum, presumably because of the dense and uniform coverage of the defective SWCNTs on the MgH_2 surface. Cryo-stage transmission electron microscopy (TEM) analysis of the hydride powders revealed that they are nanocrystalline and in some cases multiply twinned. Since defects are an integral component of hydride-to-metal phase transformations, such analysis sheds new insight regarding the fundamental microstructural origins of the sorption enhancement due to mechanical milling. The nanocomposite shows markedly improved cycling as well. Activation energy analysis demonstrates that any catalytic effect due to the metallic nanoparticles is lost during cycling. Improved cycling performance is instead achieved as a result of the carbon allotropes preventing MgH_2 particle agglomeration and sintering. The nanocomposite received over 100 sorption cycles with fairly minor kinetic degradation.

We investigated the catalytic effect of Fe + Ti bi-metallic catalyst on the desorption kinetics of magnesium hydride. Sub-micron dimensions for MgH_2 particles and excellent nanoscale catalyst dispersion was achieved by high-energy milling. The composites containing Fe shows DSC desorption temperature of 170 ^oC lower than as-received MgH_2 powder, which makes it suitable to be cycled at relatively low temperature of 250 ^oC. The low cycling temperature also prevents the formation of Mg_2FeH_6. The ternary Mg-Fe-Ti composite shows best performance when compared to baseline ball milled magnesium hydride

with only one catalytic addition. With a very high BET surface area it also shows much less degradation during cycling. The synergy between Fe and Ti is demonstrated through use of TEM and by carefully measuring the activation energies of the baseline and the ternary composites.

Acknowledgements

This thesis is a work that could not be accomplished without help of others. First, I would like to thank my supervisor, David Mitlin, for unconditionally giving the resources and the freedom I required. I am grateful for the Help of Mitlin Group; many thanks to Mohsen Danaie, Julian Haagsma, Chris Harrower, Chris Holt, Peter Kalisvaart, Reza Mohammadi, Brian Olsen, Colin Ophus, Xuehai Tan and Beniamin Zahiri. I would like to thank the technicians and staff at National Institute for Nanotechnology (NINT) and University of Alberta. Thank you to Greg Popowich, Jian Chen and Mike Xia.

I also thank all of my other friends for their ethereal support. Lastly, I would like to thank my family for giving me all the support I needed.

Contents

1 Introduction **1**

1.1 Hydrogen as an energy carrier . . . 1

1.1.1 Economy of hydrogen storage . . . 1

1.1.2 Hydrogen storage media . . . 2

1.2 Metal hydrides . . . 2

1.2.1 Thermodynamics . . . 3

1.2.2 Kinetics . . . 6

1.3 Magnesium hydride . . . 13

1.3.1 Destabilization of Magnesium Hydride . . . 14

1.3.2 Catalyst for MgH_2 Sorption . . . 15

1.4 Thesis Objectives and Scope . . . 19

2 The Influence of SWCNT-Metallic Nanoparticle Mixtures on the Desorption Properties of Milled MgH_2 Powders **21**

2.1 Introduction . . . 21

2.2 Experimental Procedure . . . 23

2.3 Results . . . 28

2.4 Discussion . . . 35

2.5 Summary . . . 38

3 Hydrogen Sorption Cycling Stability and Microstructure of Single-Walled Carbon Nanotube (SWCNT) Magnesium Hydride Nanocomposites **39**

3.1 Introduction . . . 39

3.2 Experimental Procedure . . . 41

3.3 Results . . . 44

3.4 Discussion . . . 56

3.5 Summary . . . 58

4 Synergy of Elemental Fe and Ti Promoting Low Temperature Hydrogen Sorption Cycling of Magnesium **59**

4.1 Introduction . . . 59

4.2 Experimental Techniques . . . 60

4.2.1 Kinetics Measurements . . . 63

4.3 Results . . . 65

4.4 Discussion . . . 75

4.4.1 Kinetic analysis . . . 77

4.4.2 Role of Fe and Ti . . . 78

4.4.3 Role of FeTi compound . . . 79

4.4.4 Synergy of Fe and Ti . . . 80

4.5 Summary . . . 80

5 Conclusions **81**

Bibliography **84**

List of Figures

1.1 (a) PCT diagram for an idealized metal-hydrogen system (b) van't Hoff plot and heat of formation of hydride measurement 4

1.2 Potential energy curves for the activated or non-activated dissociation and chemisorption of hydrogen on a clean metal surface, followed by the endothermic or exothermic solution of atomic hydrogen into the bulk (adapted from [1] and [2]). 8

1.3 Effect of grain size on hydride formation. 14

2.1 (A) SEM micrograph of the as-received MgH_2 powder; (B) SEM micrograph of the as-received SWCNT-amorphous carbon-metallic nanoparticle mixtures; (C) HRTEM micrograph of the SWCNT-amorphous carbon-metallic nanoparticle mixture. (D) Z-contrast HADF micrograph of metallic nanoparticles in the as-received SWCNT mixture. 23

2.2 Constant heating rate DSC and TGA results for milled MgH_2 powder by itself and co-milled with 5wt.% SWCNT mixtures: (A) 1 hour milling; (B) 7 hours milling; The SWCNT mixtures were added either at the beginning of each milling cycle (M7hC7h, etc.), or in the last 30 minutes (M7hC30m, etc.). Constant heating rate DSC and TGA results for milled MgH_2 powder by itself and co-milled with 5wt.% SWCNT mixtures: (C) 20 hours milling. (D) Best performance TGA data for each milling time.(E) Isothermal TGA desorption results for milled MgH_2 powder by itself and (F) co-milled with 5wt.% SWCNT mixtures. 27

2.3 Particle size distributions for the baseline hydride, the hydride co-milled with the SWCNTs for the entire duration and the hydride where the SWCNTs were added during the last 30 minutes. (A) 1 hour milling; (B) 7 hours milling; (C) 20 hours milling. 29

2.4 Raw XRD results for the milled hydride and the hydride co-milled with the SWCNTs for the entire duration. 30

2.5 XRD IBA analysis grain size (A), and root mean square (rms) strain (B), for the baseline hydride and hydride co-milled with the SWCNTs for the entire duration. 30
2.6 (A): Bright field micrograph of several particles from the batch that was co-milled with SWCNTs for 1 hour. (B) and (C): Dark field and corresponding SAD of an individual hydride crystallite within the largest particle. 31
2.7 (A): Bright field micrograph of several MgH_2 particles from the batch that was co-milled with SWCNTs for 1 hour. (B) and (C): Dark field micrograph and corresponding SAD of the twins within the hydride grains (arrowed). . . 32
2.8 HRTEM images of SWCNTs attached to MgH_2 particles. A) MgH_2 + SWCNT composite co-milled for 30 minutes. B) MgH_2 + SWCNT composite co-milled for 60 minutes. Arrows in the image point to the SWCNTs, except for the top arrow in (A) which marks a metallic nanoparticle. 33
2.9 Bright field and Z-contrast HAADF STEM micrographs of metallic nanoparticles (arrowed) on the hydride powder surface after 72 hours of co-milling. EDXS confirmed that the lower arrowed particle is Mn-Fe based. 34
2.10 (A) Raman spectra for hydride - SWCNT mixtures co-milled for various durations; (B) G-band to D-band ratio as a function of milling time. 34
2.11 Constant heating rate analysis for activation energy of desorption (A) Ozawa TGA-based analysis using 80% reaction completion by weight. (B) Kissinger DSC-based analysis using maximum reaction rate. 35

3.1 A) BET specific surface area versus milling time, for both the SWCNT-MgH_2 system and for the MgH_2 baseline. Optimum dispersion of the SWCNTs on the MgH_2 surfaces is achieved after 1 hour of co-milling, as evidenced by a sharp peak in the BET surface area. B) A TEM micrograph that illustrates the dispersion on the SWNCTs on the MgH_2 metal surfaces. The arrows in the figure point to the regions where the MgH_2 is clearly in contact with the SWCNTs. 45
3.2 TGA 1 hour co-milled SWCNT-MgH_2 with mass 2 overlay and first order derivative of TG (DTG). 45
3.3 Van't Hoff plot for enthalpy of desorption comparing baseline MgH_2 and SWCNT-MgH_2 composites. The data was obtained from constant heating rate, variable pressure HP-DSC analysis. 46
3.4 representative absorption and desorption cycling data for the baseline MgH_2 powder (A and B) and for the SWCNT-MgH_2 composites (C and D). The cycling experiments were performed at 300 °C. With increased cycling the kinetics degrade but at different rates for the two systems. 47

3.5 Absorption and desorption (4 wt.% hydrogen) cycling data for the baseline MgH_2 powder and for the SWCNT-MgH_2 composites. The cycling experiments were performed at 300°C. With increased cycling the kinetics degrade but at different rates for the two systems. 48

3.6 Activation energy of desorption obtained via Kissinger analysis. The powder history and activation energy are given on the graph. 49

3.7 Grain size and lattice strain as a function of cycling. 49

3.8 TEM-obtained particle size distributions for the as-milled powders and for the sorption cycled MgH_2-SWCNT composites. It is not possible to analyze the post-cycled baseline MgH_2 powder due to extensive sintering of the particles. 50

3.9 (A) Scanning electron micrograph of several agglomerated/sintered MgH_2 particles after 10 cycles. (B) Bright field TEM micrograph of several sintered MgH_2 particles representative of the size distribution found in the baseline MgH_2 after 10 cycles. Arrows point to the sintered interface between two previously separate particles. 51

3.10 TEM micrographs highlighting the nanocrystalline microstructure of the baseline MgH_2 powder after 10 sorption cycles. A) Bright field micrograph of several differently oriented hydride particles. B) Dark field micrograph obtained using a portion of the 110 α-MgH_2 ring pattern highlighting numerous nanocrystalline grains. C) Corresponding selected area diffraction (SAD) pattern with a simulation insert. Arrows point to the same area in bright field and dark field micrographs. 52

3.11 TEM micrographs highlighting the nanoscale twins (arrowed) present in the baseline MgH_2 powder after 10 sorption cycles. A) Bright field micrograph. B) Dark field micrograph obtained using a portion of the 011 α-MgH_2 ring pattern highlighting the twins. C) Corresponding selected area diffraction (SAD) pattern with a simulation insert. 52

3.12 TEM micrographs highlighting a single larger a-MgH_2 crystallite in the SWCNT-MgH_2 composite after 20 sorption cycles. A) Bright field micrograph. B) Dark field micrograph obtained using a g =110 α-MgH_2 reflection. C) Corresponding selected area diffraction (SAD) pattern with a simulation insert. 54

3.13 TEM micrographs highlighting unsorbed Mg particles in the MgH_2-SWCNT composite after 20 sorption cycles. A) Bright field micrograph. B) Dark field micrograph obtained using a g =200 Mg reflection. C) Corresponding selected area diffraction (SAD) pattern with a simulation insert. 54

3.14 A and B) Z-contrast HAADF STEM micrographs of a metallic nanoparticle on the composite powder surface after 35 cycles. C) EDXS elemental maps of carbon, magnesium, cobalt, and nickel in the area marked by red square. The map demonstrates how the hydride particles remain encapsulated by carbon during the cycling. 55

3.15 Raman spectra of the MgH_2+SWCNT composites before and after cycling, indicating that the SWCNTs have survived 35 absorption/desorption cycles. 56

4.1 DSC curves showing the effect of different additives on desorption peak temperature of magnesium hydride. 61

4.2 (a) Sievert's absorption and desorption cycles of MgH_2-Ti10 sample. First cycles are the fastest. (b) Sievert's absorption and desorption cycles of MgH_2-Fe10 sample. On absorption the kinetics improves through cycling whereas on desorption it accelerates first and slowly degrades after 30 cycles. (c) Sievert's absorption and desorption cycles of MgH_2-Fe5Ti5 sample. On absorption the kinetics improves through cycling whereas on desorption it accelerates first and slowly degrades after 30 cycles. (d) Sievert's absorption and desorption cycles of MgH_2-(FeTi)10 sample. On desorption the kinetics improves through first 10 cycles (activation). On absorption the performance degrades from the start through the end of cycling. 62

4.3 Time to reach 3.6 wt % capacity for the studies samples. Max Capacities of the composites are as follows: 5.3 wt % for MgH_2-Ti10, 4.5 wt % for MgH_2-Fe5Ti5, 4.5 wt % for MgH_2-Fe10 and 4.25 wt % for MgH_2-(FeTi)10 . . 63

4.4 Pressure composition isotherms for MgH_2-Fe5Ti5 at 250 °C showing no thermodynamic change from that of pure magnesium / hydrogen system. The very similar graph was acquired for MgH_2-(FeTi)10 as well. 65

4.5 Activation energies before and after cycling measured using Kissinger analysis. 66

4.6 (a) X-ray diffraction patterns of the as-milled composites. (b) X-ray diffraction patterns of the as-cycled composites. 67

4.7 STEM - HAADF image (A) and STEM - bright field (BF) image of the mapped area (B) along with EDS elemental maps of Mg (C) and Fe (D) from a particle of MgH_2-Fe10 composite before cycling, showing uniform dispersion of Fe particles on Mg surface in nano scale. 68

4.8 STEM BF (A) and HAADF image of the mapped area (B) along with EDS elemental maps of Mg (C) and Fe (D) from a particle of MgH_2-Fe10 composite after 75 cycles showing uniform dispersion of Fe particles on Mg surface. . . . 69

4.9 STEM - BF image (A) and STEM - HAADF image (B) along with EDS elemental maps of Mg (C) and Ti (D) from a particle of MgH_2-Ti10 composite before cycling showing uniform dispersion of Ti particles on Mg surface. . . . 70
4.10 STEM - BF image (A) and STEM - HAADF image of the mapped area (B) along with EDS elemental maps of Mg (C) and Ti (D) from a particle of MgH_2-Ti10 composite after 75 cycles showing uniform dispersion of Ti particles on Mg surface. . . . 71
4.11 STEM - BF image (A) and EDS elemental maps of Mg (B), Fe (C) and Ti (D) from a particle of MgH_2-Fe5Ti5 composite showing uniform dispersion of Fe and Ti on Mg surface. . . . 72
4.12 STEM - HAADF image of the mapped area (A) along with EDS elemental maps of Mg (B), Fe (C) and Ti (D) from a particle of MgH_2-Fe5Ti5 composite after 115 cycles showing uniform dispersion of Fe and Ti on Mg surface. . . . 73
4.13 STEM - HAADF image (A) of the mapped area, EDS elemental maps of Mg (B), Fe (C) and Ti (D) from a particle of MgH_2-(FeTi)10 composite showing dispersion of FeTi particles on Mg surface. Fe and Ti appears on similar spots confirming their being in intermetallic compound form. . . . 74
4.14 STEM - HAADF image of the mapped area (A) and EDS elemental maps of Mg (B), Fe (C) and Ti (D) from a particle of MgH_2-(FeTi)10 composite after 115 cycles showing dispersion of FeTi particles on Mg surface. Fe and Ti appears on similar spots confirming their intermetallic state. . . . 75
4.15 Particle size distribution of post cycled composites. The mean particle size for post cycled samples are 326, 365, 200, and 246 nm for MgH_2-Ti10, MgH_2-Fe10, MgH_2-Fe5Ti5 and MgH_2-(FeTi)10, respectively. . . . 76
4.16 desorption kinetics data of MgH_2-Ti10 composite and corresponding JMA fits. The Avrami value is 3 for the first five cycles and it is 2 for the rest of cycles. . . . 78
4.17 JMA rate constant (k) values as a function of cycle number . . . 79

List of Tables

2.1 Crystallographic data used for generating electron diffraction simulations. . . 28

3.1 Crystallographic data used for generating electron diffraction simulations. . . 44

4.1 BET- surface area of different composites after milling. 65

1

Introduction

1.1 Hydrogen as an energy carrier

Finite sources of hydrocarbon energy along with their destructive effect on environment have led to an extensive research for a renewable, environment friendly, easy to handle, reliable and safe source of energy to replace fossil fuels. Hydrogen is considered to be one of the best alternative energy sources due to its abundance, easy synthesis, and non-polluting nature. The problem with hydrogen is safe storage and easy handling.

Hydrogen is an energy carrier and like electricity can be produced from a variety of fossil fuels and other primary energy sources. Electricity can also be used to produce hydrogen through electrolysis of water. With the highest heating value per mass of all chemical fuels, hydrogen can be used as the fuel for electricity generation via either combustion methods or fuel cells. Hydrogen occurs in the form of water and hydrocarbons on earth.

Like any energy transformation, production of hydrogen from primary energy sources includes some energy loss. This is due to its flexibility, efficiency and absence of pollution at the point of end use that makes hydrogen highly promising for future use similar to electricity.

1.1.1 Economy of hydrogen storage

In order for a hydrogen economy to produce overall CO_2 emissions reductions, any hydrogen production process must make CO_2 emissions less harmful through carbon capture or similar technologies; use non-emitting fuel sources such as nuclear, wind, or other renewable power; and/or offset CO_2 emissions with comparatively higher efficiency.

The least expensive source for a centralized hydrogen supply is fossil fuel processed at large centralized facilities, with appropriate consideration of life-cycle emissions [3]. Such an infrastructure will have to overcome significant cost and structural challenges to become economically viable. Other hydrogen production technologies, such as nuclear thermochemical processes, could considerably lower life-cycle emissions, and presumably costs; however,

they still need extensive research and development.

Another economical challenge against hydrogen fueled vehicles is the refueling infrastructure. Complexity and cost of developing such infrastructure and the relative simplicity of vehicle design for the hydrogen fuel cell must be economical as opposed to onboard produced hydrogen fueled vehicle (by reforming hydrocarbons onboard) with combustion engines [3].

1.1.2 Hydrogen storage media

The next issue facing the hydrogen economy is hydrogen storage. Hydrogen has a low density as a gas and the costs of liquefaction are very high. The largest hydrogen storage challenges relate to transportation applications in which fuel cell vehicle (FCV) design constraints, such as weight, volume, and efficiency, limit the amount of hydrogen that can be stored onboard a vehicle. A suitable storage medium for hydrogen must meet these criteria: high storage capacity, moderate sorption and desorption temperatures and pressures which necessitate low heat of hydride formation, low cost, low weight, and high stability against O_2 and moisture for long cycle life. Hydrogen storage costs for fuel cells must fall to about $2 per kilowatt hour, from the current estimate of about $8 per kilowatt hour for a system with compressed storage tank of about 35 MPa pressure [4].

Hydrogen can be stored as pure gas in form of pressurized gas or cryogenic liquid, or can be physically absorbed (physisorption) in carbon materials. Hydrogen can be chemically stored (chemisorption) in form of metal hydrides or complex hydrides, or produced onboard the vehicle by reforming methanol or gasoline [3]. The reported storage capacities of carbon materials scatter widely between 0.2 and 10 wt% [5, 6], and high reported storage capacities could not independently be reproduced [7]. Today's consensus is that although having acceptable reversibility, carbon materials cannot store enough hydrogen needed for automotive application [8].

Hydrogen can also be stored in some metals in form of metal hydrides. Metal hydrides have higher volumetric density (e.g. 110 kg H_2 m^{-3} for MgH_2) than hydrogen gas ($<$40 kg H_2 m^{-3}) or liquid hydrogen (71 kg H_2 m^{-3}) [1].

1.2 Metal hydrides

Hydrogen can react with some metals at elevated temperatures and pressures to form metal hydrides. Metal hydrides appear to be a convenient alternative storage method to conventional means of storage. They are a safe, low-pressure and stable alternative for pressurized hydrogen. Metal hydrides have the largest volumetric storage capacity which is up to 60% more than liquid hydrogen [9]. Interestingly, low density metals like Mg and Al have massive capacity of hydrogen. The problem with Mg and Al based hydrogen storage systems is that, the hydride they form is very stable in room temperature, and the kinetics of sorption

is poor even at high temperatures. To overcome these problems, one can either refine the structure or add a proper catalyst.

The metal hydride formed may be different in nature and fall between one of the major categories distinguished: saline (ionic) hydrides, covalent (molecular) hydrides, and metallic hydrides [10]. Binary transition metals form metallic hydrides while metals from alkaline and earth alkaline groups make ionic hydrides. Transition hydrides of the form MH_n deviate largely from stoichiometric compositions (n=1, 2, 3). For the types MH and MH_2 and MH_3 the lattice structure is that of the metal with hydrogen atoms sitting at tetrahedral or octahedral interstitial sites or a combination of both [1]

It is possible to tailor the properties of metallic hydrides of form AB_xH_n where A is a rare earth or alkaline earth metal that has a tendency to form a hydride and B is a transition metal that forms an unstable hydride. The hydrides with A:B ratios of x=0.5, 1, 2, 5 are shown to form hydrides with hydrogen to metal ratio of up to two [1].

At low hydrogen concentrations of less than 0.1 at.% H, the solid solution α-phase forms with hydrogen dissolving exothermally in the host metal lattice. At higher concentrations of hydrogen the hydride phase starts to nucleate and grow which causes lattice expansion in the order of 10-20% (as opposed to 2-3 $Å^3$ per hydrogen atom in the α-phase). The stress buildup at the $\alpha - \beta$-phase boundary might cause decrepitation of brittle host metals such as an intermetallic compound [1]. Most hydrides have either a rather low storage capacity or have shown very poor absorption/desorption kinetics. Also, metal hydrides require activation (in order to desorb hydrogen) at high temperature and hydrogen pressure. However, hydrogen concentration in metal hydrides is even larger than that in liquid hydrogen e.g. 6.7 atoms H/mol x10^{-22} in MgH_2 compared to 4.2 in liquid hydrogen [9]. Thermodynamic stability, kinetics and hydrogen capacity of metal hydrides are of critical importance for they use as hydrogen media. Reversible hydrogen hydrogen-metal systems with high hydrogen content that can absorb and desorb hydrogen at low pressures and temperatures can be used as hydrogen storage media.

1.2.1 Thermodynamics

The thermodynamics of hydride formation from gaseous hydrogen is described by pressure - composition isotherms (Figure 1.1). As hydrogen is dissolving in α-phase, the pressure increases with the concentration until it reaches the point where α-phase starts forming. From this point there is a plateau in the isotherm where the pressure does not change (equilibrium pressure, P_{eq}) until conversion of α-phase to β-phase is completed. Nucleation and growth of hydride phase may occur at free surfaces, inter-grain boundaries, and within the bulk. A flat plateau represents a reversible absorption/desorption of hydrogen; although it is seldom the case. An experimentally driven sloping plateau in most of the cases is due

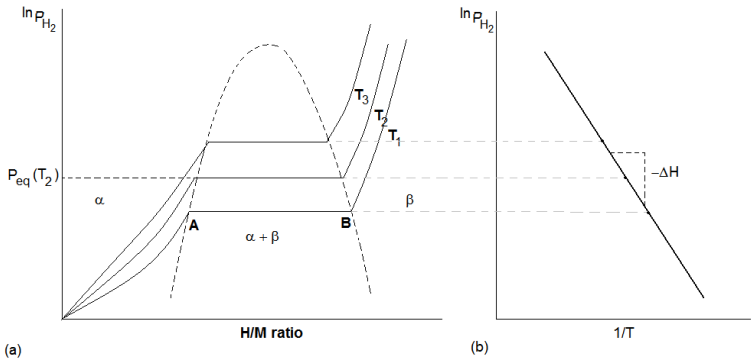

Figure 1.1: (a) PCT diagram for an idealized metal-hydrogen system (b) van't Hoff plot and heat of formation of hydride measurement

to non-equilibrium conditions imposed by low kinetics; however, when in true equilibrium, a sloping plateau is due to imperfections in lattice and thus existence of slightly different potentials for crystallographically identical interstitial sites [11]. The length of the plateau, on the other hand, represents the hydrogen content of the hydride.

In pure β-phase the pressure steeply increases with the concentration. Above the critical temperature T_c where the two phase region ends, the conversion of α-phase to β-phase is continuous. The difference in thermodynamics information derived from absorption and from desorption is called hysteresis [10]. It might be because of non-equilibrium conditions; however, in general it is attributed to loss of inelastic lattice expansion occurring in hydrogen absorption [11]. The p-c isotherms of nanocrystalline alloys (with grain size of less than about 50 nm) differ from the polycrystalline with an enhancement of solid state solubility [12].

The Van't Hoff equation relates the equilibrium pressure with the enthalpy and the entropy of hydride formation:

$$ln(\frac{p_{eq}}{p_o})\Big|_T = -\frac{\Delta H_{\alpha\to\beta}}{RT}\Big|_T + \frac{\Delta S_{\alpha\to\beta}}{R}\Big|_T \tag{1.1}$$

Since the major attributing factor to the change in the entropy is the dissociation of molecular hydrogen into dissolved hydrogen atoms it can be approximated to the standard entropy of hydrogen (S_o=-130 J.K^{-1}mole^{-1} H_2), thus for metal-hydrogen systems ΔS=-130 J.K^{-1}mole^{-1} H_2. The enthalpy term shows the stability of the metal hydride bonds. Based on Van't Hoff equation, in order to have a metal hydride that has an equilibrium pressure of 1 atmosphere at room temperature, the enthalpy of hydride formation is measured as ΔH=-39 kJ.mole^{-1}H_2. For an endothermic release of hydrogen if the absolute value of enthalpy is higher than this amount, heat should be delivered from an external source to the system. For example for magnesium hydride the heat of hydride formation is ΔH=-76 kJ.mole^{-1}H_2 which makes it too stable to be desorbed at room temperature.

Here a derivation of the thermodynamic equations governing the dissolution of hydrogen into a host metal lattice and consequently forming the metal hydride phase, based on basic thermodynamics relations is given. Hydrogen gas in thermal equilibrium with hydrogen dissolved in a metal can be expressed by the reaction:

$$M + \frac{1}{2}xH_2 = MH_x \tag{1.2}$$

When the gaseous hydrogen is in equilibrium with the solid solution, the chemical potential of the molecular hydrogen gas μ_g is equal to the chemical potential of hydrogen in solid solution μ_α:

$$\frac{1}{2}\mu_g(p,T) = \mu_\alpha(p,T,x). \tag{1.3}$$

For working pressures under about 100 bar, which is the case in actual sorption tests, hydrogen can be considered as an ideal gas. From statistical thermodynamics the chemical potential of an ideal gas is

$$\mu_g(p,T) = kTln(\frac{p}{p_\circ}) - \frac{1}{2}E_d \tag{1.4}$$

where

$$p_\circ = \frac{8(\pi kT)^{\frac{7}{2}}M^{\frac{5}{2}}r_\circ^2}{h^5} \tag{1.5}$$

and k is the Boltzmann constant, E_d is the dissociation energy of an H_2 molecule, M is the mass of a H_2 molecule, r_o is the molecular distance between H atoms, and h is Planck's constant. By convention, the enthalpy and entropy are defined relative to the standard pressure p_o given by equation 1.5. At the temperature of 7.55 K (p_o = 1.013x105 Pa). The Gibb's free energy of each of x hydrogen atoms (per metal atom) in a solid solution can be expressed in terms of the enthalpy H_α and entropy S_α of solution

$$G_\alpha = H_\alpha - TS_\alpha. \tag{1.6}$$

The entropy S_α consists of the excess entropy of solution $S_{\alpha e}$ and the partial ideal configurational entropy $S_{\alpha i}$

$$S_\alpha = S_{\alpha e} + S_{\alpha i}. \tag{1.7}$$

For x number of hydrogen per metal atoms occupying r number of interstitial cites per metal atoms, the configurational entropy of hydrogen in a crystal, $S_{\alpha i}$ may be written as

$$S_{\alpha i} = -k.ln(\frac{r!}{x!(r-x)!}). \tag{1.8}$$

Using Sterling's approximation (ln(n!) = n ln(n) - n), and $S_{\alpha i}$ becomes

$$S_{\alpha i} = krln(\frac{r}{r-x}) - kxln(\frac{x}{r-x}). \tag{1.9}$$

Therefore, from equations 1.6, 1.7 and 1.9 the chemical potential can be rewritten as

$$\mu_\alpha(p,T,x) = \frac{\partial G_\alpha}{\partial x} = h_\alpha - Ts_{\alpha e} + kTln(\frac{x}{r-x}) \tag{1.10}$$

where h_α is the partial enthalpy and $s_{\alpha e}$ is the non-configurational part of the partial entropy of hydrogen in solution. For low hydrogen concentrations, where x $\ll$ r

$$ln(\frac{x}{r-x}) \rightarrow lnx - lnr \tag{1.11}$$

so, the equation 1.10 can be rewritten as

$$\mu_\alpha(p,T,x) = h_\alpha - Ts_{\alpha e} + kTlnx - kTlnr. \tag{1.12}$$

From equation 1.3, equations 1.4 and 1.12 can be equated:

$$kTln(\frac{p}{p_\circ}) - \frac{1}{2}E_d = h_\alpha - Ts_{\alpha e} + kTlnx - kTlnr. \tag{1.13}$$

This is Sievert's law stating that for dilute solutions concentration of hydrogen is proportional to the square root of pressure

$$x = \Psi(T)\sqrt{(\frac{p}{p_o})} \tag{1.14}$$

where

$$\Psi(T) = exp(\frac{Ts_{\alpha e} - h_\alpha + kTlnr - \frac{1}{2}E_d}{kT}) \tag{1.15}$$

As can be seen in the model PCT diagram of Figure 1.1, in many cases at higher concentrations and below a critical temperature, there is a miscibility gap that atomic hydrogen can not be dissolved in the metal lattice and a new hydride phase forms which corresponds to the plateau of the PCT diagram in Figure 1.1. In the plateau range of the concentrations the solid solution is in equilibrium with the gaseous hydrogen and the hydride phase. the presence of the three phases of α and β and gaseous H_2 should satisfy the condition of balances chemical potentials as follows

$$\frac{1}{2}\mu_g(p,T) = \mu_\alpha(p,T,x) = \mu_\beta(p,T,x). \tag{1.16}$$

This equation leads to the Van't Hoff equation for equilibrium pressure $P_{eq}(T)$ in terms of the enthalpy and the entropy of the $\alpha \rightarrow \beta$ phase transformation which is already seen in equation 1.1. Based on the Van't Hoff equation the enthalpy and entropy of hydride formation may be determined experimentally from the slope and intercept of a van't Hoff plot of $ln(P_{eq})$ versus $1/T$ as shown in Figure 1.1.

1.2.2 Kinetics

The reaction of metallic elements with hydrogen consists of five different steps: physisorption (adsorption), diffusion, chemisorption (recombination), surface penetration, diffusion and hydride formation (decomposition) [13, 14]. Desorption may be considered as the reverse process. The slowest step is the bottleneck for the kinetics of the sorption or desorption. It should be noted that the slowest step is not necessarily the same for both absorption and

desorption processes. At each step the kinetic curve has its characteristic form which can be formulated based on the amount of transformed phase versus time. If a good fit with a specific kinetic equation is obtained, the rate limiting step can be deduced. The suitable catalyst may be found regarding the limiting step of physical and chemical absorbtion (desorption) [13]. Activation energies of desorption process is calculated based on kinetic rate constants derived from kinetic curves of at least two different temperatures [14].

Hydrogen Interaction with the Surface

There is considerable adsorption of hydrogen on the surface of certain metals at cryogenic temperatures. As the temperature increases, the adsorption decreases to a minimum at temperatures between -180 ^{o}C and 0 ^{o}C and subsequently increases to a maximum and then diminishes again at higher temperatures [15]. The first type of adsorption that occurs at low temperatures is attributed to van der Waals forces. The second type of adsorption has been called chemisorption or sometimes *activated* adsorption. In chemisorption the hydrogen molecule is dissociated into atoms after a certain *activation* energy is provided. This type of activated adsorption is termed absorption. There is an activation energy for adsorption (physisorption) and a quite different one for absorption (chemisorption).

During hydrogen absorption or desorption, hydrogen atoms have to pass through the surface of the metal. When absorbing, hydrogen must be in its atomic form beyond the surface to be transported into and out of the bulk. When desorbing, pairs of atomic hydrogen meet and reassociate at the surface to leave the surface in molecular form (hydrogen gas). Since the surface properties play a very important role in the kinetics of sorption, understanding the interaction of hydrogen with the surface of a metal is very important. However, the fact that the surface properties of the metal may be substantially different than those of the bulk, due to the discontinuity of the lattice at the surface, complicates the problem. Surface layer consists of the atomic region which shows different properties from those of the bulk. For a clean single crystal, the surface layer is generally no thicker than the first three or four monolayers. Oxidized, contaminated, or multiphase materials may have a surface layer as thick as ∼10 nm. As shown in Figure 1.2 far from the metal surface, the potential of a hydrogen molecule and of two hydrogen atoms are separated by the dissociation energy ($H_2 \rightarrow 2H$, E_{Diss} = 435 kJ.mol^{-1} H_2). The van der Waals force leads to the physisorbed state ($E_P \approx$ 10 kJ.mol^{-1}H) approximately one hydrogen molecule radius ($\approx$ 0.2 nm) from the surface. Closer to the surface, the hydrogen has to overcome an activation barrier for dissociation and subsequently formation of the M-H bond. Hydrogen atoms sharing their electron with the metal atoms at the surface are then in the chemisorbed state ($E_C \approx$ 50 kJ.mol^{-1}H. The chemisorbed hydrogen atoms can jump through the host metal lattice in an endothermic or exothermic diffusion process [1, 2]. Following is a further discussion of

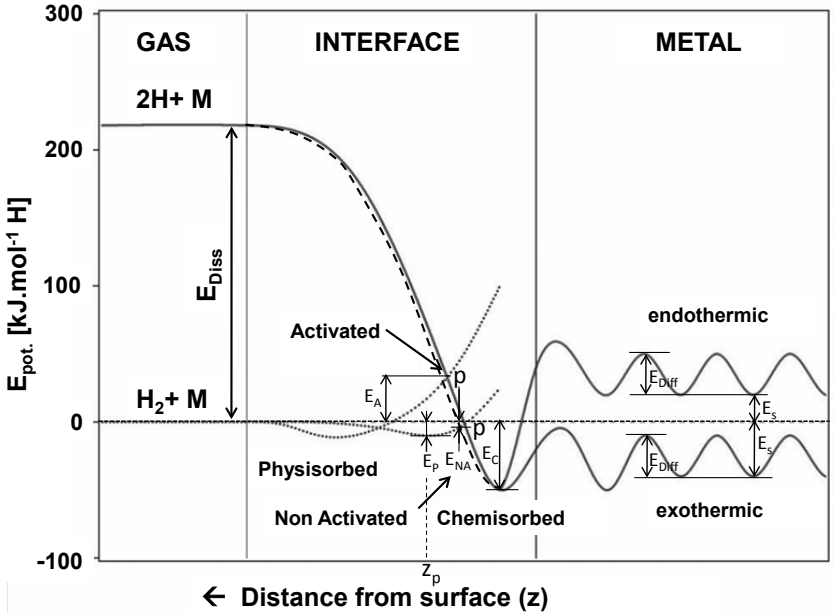

Figure 1.2: Potential energy curves for the activated or non-activated dissociation and chemisorption of hydrogen on a clean metal surface, followed by the endothermic or exothermic solution of atomic hydrogen into the bulk (adapted from [1] and [2]).

physisorption and chemisorption phenomena.

Physisorption. Let us consider a hydrogen molecule infinitely far away from the surface which is assumed to be ideal. The H_2 molecule now approaches the surface along the reaction coordinate, z, perpendicular to the surface plane. The situation can very conveniently be described in terms of the well-known one-dimensional Lennard-Jones potential energy diagram [15] which is shown in Figure 1.2. There will be only small attractive interaction forces of van der Waals origin as the H, molecule is sufficiently close to the surface giving rise to a shallow interaction potential (depth E_p) at a distance z_p from the surface. The interaction between the hydrogen molecule and the surface are very small; ranging between 3.5 and 15 kJ.mol^{-1}, depending on the system [2].

Chemisorption. If the molecule of hydrogen is dissociated into the atoms on the surface a different interaction pattern is observed; since the dissociation energy has to be spent on the system first, the potential energy curve in Figure 1.2 starts 435 kJ above the energy zero level. The H atoms tend to form chemical bonds with the surface material. As seen in the chemisorption curve of the Figure 1.2 strong attractive interaction forces lead to a pronounced lowering of the potential energy of the system as the H atoms are brought close to the surface. The depth of the potential well (E_c) ranges between 500 and 600 kJ.mol^{-1}

representing the energy content of a single hydrogen - surface-atom bond [2]. This quantity is per hydrogen atom and gained twice per hydrogen molecule. The superposition of the physisorptive and the atomic interaction potential energy curves yields a crossover point P which may lie above or below the energy zero level. In the case where the point of intersection is below E = 0, spontaneous dissociation will occur at P without any need for additional energy; a small amount of energy shown as E_{NA} is released and H atoms then readily enter the so-called *chemisorption* potential energy well and the heat of chemisorption, E_c is released and can be measured in an experiment quite easily. This is the *non-activated* adsorption of hydrogen, which is observed in the interaction of H, with high-index planes of transition metal surfaces such as Ni, Pd or Pt. The well-known activation of hydrogen over Raney-nickel or platinum black are examples of spontaneous dissociation of hydrogen molecules. The energy balance of this exothermic process is as follows: One gains the heat of adsorption, E_{ad} (depicted as E_{NA} in Figure 1.2) and twice the energy of a H-metal bond, E_{M-H}, whereas the heat of dissociation, E_{Diss}, must be spent on the system. Accordingly, the experimental determination of the heat of adsorption allows the Me-H bond energy to be calculated:

$$E_{M-H} = \frac{1}{2}(E_{Diss} + E_{ad}) \tag{1.17}$$

Interestingly, in spite of quite large differences in the heats of adsorption, the various systems are not much different in terms of E_{M-H}. The values range around 2.6 eV for the H-M binding energy. This highlights the similarity of binding mechanism of hydrogen to many metals as has been confirmed theoretically [16].

The other case of the interaction is where the intersection of the two potential energy curves of physisorption and chemisorption is above E = 0. This situation is called *activated* adsorption. The system has to be provided with an extra amount of energy (*activation* energy) in order for the dissociation to happen. In this case the dissociation/recombination reaction is slow and may be the rate limiting step of the absorption and desorption. In reality, a clean surface of the metal is usually not the case. The surface of the metals is usually passivated by oxygen, which prevents the dissociation of molecular hydrogen and the diffusion of atomic hydrogen into the bulk.

Kinetic Measurements

Activation Energy Measurement Methods. When a reaction occurs in differential thermal analysis (DTA),the change in the thermal properties of the sample is reflected by a deflection or a peak. If an activation energy is needed for the reaction to proceed, it occurs at a rate varying with temperature and the position of the peak changes with the heating rate if other experimental parameters maintained fixed. Note that it is assumed that the temperature of maximum deflection (the peak) in differential thermal analysis is also the

temperature at which the reaction rate is maximum. This variation in peak temperature could be used to determine the activation energy of the reaction for first order reactions. Kissinger analysis [17] can be employed to measure the activation energy of reaction. The method developed by Kissinger allows for obtaining the activation energy of a chemical reaction of any order by considering the variation of the peak temperature. The fact that the conversion at the maximum rate of conversion is constant and independent of the heating rate in the case of linear heating, if the rate constant follows the Arrhenius law, makes this method widely applicable. The Kissinger analysis can be expressed in the following form:

$$\ln \frac{\phi}{T_f^2} = \ln \frac{Rk_o}{E} - \frac{E}{RT_f} \tag{1.18}$$

where ϕ is the heating rate, T_f is the absolute temperature at the maximum reaction rate, E is the activation energy, k_o is the pre-exponential term for the rate constant $k = k_o \exp(-E/RT)$ and R is the gas constant. The activation energy is obtained from a linear plot of $\ln(\phi/T_f^2)$ versus $1/T_f$. For this analysis, the heating rates used were 5, 10, 20, and 25 °C min^{-1}. Thermogravimetric analysis data can also be used to obtain the activation energy of the reactions. In a thermogravimetric analysis the weight change of the sample is recorded at a constant heating rate. In the methods based on thermogravimetric data to measure the activation energy of the reaction the rate of weight change or decomposition has the following form:

$$-\frac{dW}{dt} = Aexp(-\frac{\Delta E}{RT})W^n \tag{1.19}$$

where W is the fractional residual weight of the sample, T is absolute temperature, R is the gas constant, t is time, A is a preexponent factor, ΔE is activation energy and n is the order of reaction. The fraction of residual weight is expressed as a function of a structural quantity that changes by temperature such as a broken bond, etc.

$$W = f(x) \tag{1.20}$$

where the change in x is shown by kinetic equation of the form

$$-\frac{dx}{dt} = Aexp(-\frac{\Delta E}{RT})g(x) \tag{1.21}$$

integration over time gives

$$-\int_{x_o}^{x} \frac{dx}{g(x)} = A\int_{t_o}^{t} exp(-\frac{\Delta E}{RT})dt. \tag{1.22}$$

In most cases the weight change can be described by equation 1.19 where $x = W$. For a 0th order reaction $g(x) = 1$ thus $\int \frac{dx}{dg} = W$ and for a 1st order reaction $g(x) = W$ thus $\int \frac{dx}{dg} = lnW$; similarly for a 2nd order reaction $g(x) = W^2$ thus $\int \frac{dx}{dg} = -\frac{1}{W}$, and so on. When the temperature of the sample is raised at a constant rate, a, change in x is given by:

$$-\int_{x_o}^{x} \frac{dx}{g(x)} = \frac{A}{a}\int_{0}^{T} exp(-\frac{\Delta E}{RT})dT \tag{1.23}$$

note that at t_0 the rate of reaction is negligible. Doyle [18] has expressed and tabulated the values of $\int_0^T exp(-\frac{\Delta E}{RT})dT$ as p function:

$$\frac{\Delta E}{R}\ p(\frac{\Delta E}{RT}) = \int_0^T exp(-\frac{\Delta E}{RT})dT. \tag{1.24}$$

Based on Doyle's approximation for $p(y)$ given in 1.34 $p(\frac{\Delta E}{RT})$ can be approximated as:

$$logp(\frac{\Delta E}{RT}) \doteqdot -2.315 - 0.4567\frac{\Delta E}{RT}. \tag{1.25}$$

For a given value of W, as I mentioned earlier, the left side of the equation 1.23 is a constant that does not depend on the heating rate. Thus for a fraction residual weight of W_1 at T_1 for the heating rate of a_1 and W_2 at T_2 for the heating rate of a_2 and so on, we will have:

$$\frac{A\Delta E}{a_1 R}p(\frac{\Delta E}{RT_1}) = \frac{A\Delta E}{a_2 R}p(\frac{\Delta E}{RT_2}) = ... \tag{1.26}$$

using equation 1.25 we have:

$$-\ log(a1) - 0.4567\frac{\Delta E}{RT_1} = -log(a2) - 0.4567\frac{\Delta E}{RT_2} = ... \tag{1.27}$$

Thus, for a given value of W, the plots of a values versus the reciprocal absolute temperature gives a straight line, slope of which gives the activation energy [19]. In other words, according to the Ozawa method an Arrhenius chemical reaction can be expressed in the following simplified form:

$$log\phi + 0.4567\frac{\Delta E}{RT} = constant \tag{1.28}$$

where T is the absolute temperature at a certain constant amount of conversion and Φ is the heating rate. Therefore the activation energy for the process may be obtained by plotting log ϕ versus $\frac{1}{T}$. There are numerous isoconversion methods for measuring the activation energy of the reaction as well; since they all originated from a common fundamental equation they have common features. The derivation of the isoconversion equations from the fundamental equation is given here. The fundamental equation is

$$C = F(\theta) \tag{1.29}$$

where C, θ and $F(\theta)$ are respectively the conversion, the reduced time and an eigen-valued function of the reduced time. The reduced time is given by

$$\theta = \int exp(-\frac{\Delta E}{RT})dt \tag{1.30}$$

where $\Delta E, R, T$ and t are the activation energy, the gas constant, the absolute temperature and the time respectively. Therefore, the Arrhenius law is assumed to be valid, with the rate constant k being given

$$k = Aexp(-\frac{\Delta E}{RT}). \tag{1.31}$$

Equation 1.29 holds for a growth process from pre-existing nuclei [20]. At a given conversion, where F(θ) is a constant

$$\theta = constant \tag{1.32}$$

For linear heating at a constant rate Φ from a temperature where the rate of conversion is negligible, θ is given by

$$\theta = \frac{\Delta E}{\Phi R}\ p(\frac{\Delta E}{RT}) \tag{1.33}$$

where p is a function proposed by Doyle for approximation of the equation of thermogravimetric data plot [18]. There are two approximation for the p function:

$$logp(y) = -2.315 - 0.4567y \quad for \quad 60 \geq y \geq 20 \tag{1.34}$$

and

$$p(y) = \frac{exp(-y)}{y^2} \quad for \quad 50 \geq y \geq 20 \tag{1.35}$$

By combining equations 1.32 and 1.34, the Ozawa method is obtained, i.e. the equation 1.28; and by combining equations 1.32 and 1.35, the equation for Kissinger method is obtained as:

$$\frac{ln\Phi}{T^2} + \frac{\Delta E}{RT} = constant \tag{1.36}$$

Kinetic Models.A large number of kinetic models have been derived to explain solid-state phase transformations in metal-hydride systems. For MgH_2 the kinetic rate limiting step is typically either the dissociation/ recombination (chemisorption) transition between hydrogen gas and hydrogen atoms on the material surface [21, 22] or the nucleation and growth (NG) of the hydride during absorption or the metal phase during desorption [21, 23]. When hydriding involves a phase transformation from α to β, nucleation and growth is usually the dominant kinetic process [24]. Mintz and Zeiri have reviewed the most important NG models for hydrogen storage [25]; the two most applicable functional forms are the contracting volume (CV) models and the model developed by Avrami [26], based on the works of Kolmogorov, Johnson and Mehl [27]. The latter is typically referred to as the JMA or KJMA. The equation for the CV model is given by

$$f = 1 - (1 - kt)^{\eta} \tag{1.37}$$

where f is the fraction of the material undergone the $\alpha \rightarrow \beta$ transformation, k is the rate constant, η is a constant related to the dimensionality of the growth process; with $\eta = 3$ for three-dimensional and $\eta = 2$ for two dimensional growth, and t is time. For this model the assumption is that the initial nucleation on the surface is fast compared to the overall kinetics of growth and the surface nucleation layer is thin compared to the particle diameter [28, 22].

JMA analysis assumes random and constant nucleation rate or constant nuclei number, infinite sample volume and hard impingement between nuclei of the new phase [29]. The central equation of this model is given by

$$f = 1 - \exp(-(kt)^{\eta}) \tag{1.38}$$

where f is the fraction of the material undergone the $\alpha \rightarrow \beta$ transformation, k is the rate constant, η is a constant related to the dimensionality of the growth process, referred to as the Avrami exponent and t is time. For a constant number of nuclei, the value of η is typically interpreted as $\eta = \frac{d}{m}$ for constant nuclei number and as $\eta = \frac{d}{m} + 1$ for constant nucleation rate, where d is the growth dimensionality and $m = 1$ for interface-controlled and $m = 2$ for diffusion-controlled growth [24, 30]. For example, assuming a constant number of nuclei, $\eta = 3$ represents three dimensional - interface controlled growth and $\eta = 1.5$ correlates with three dimensional - diffusion controlled growth, etc [24]. Here the assumptions are that the initial size of a nucleus is small compared to that of the particle, the nucleation and growth of the new phase begins randomly in the bulk and at the surface, and there is sufficient number of nuclei of the new phase within each particle.

1.3 Magnesium hydride

Because of its high hydrogen content, low weight and low price, magnesium hydride is an attractive media for hydrogen storage. The pressure of hydrogen gas in equilibrium with MgH_2 is low (1bar at 280°C); it means that from thermodynamics point of view Mg might react readily with hydrogen at room temperature. However, the kinetics of this reaction is very low [31]; so that at 300°C, the hydrogen absorption of magnesium is rather slow [13]. Amongst the kinetics limiting factors, formation of magnesium oxide and magnesium hydroxide which block hydrogen diffusion through the surface layer are very significant. Activation is done by annealing at high temperature which causes breaking of these layers due to differences in thermal expansion coefficient of Mg and its oxide and hydroxide [31]. The process of breaking the passive layer has been termed the first-stage activation [24]. Cycling the material (successive absorption/desorption) results in kinetics improvement over about ten first cycles which has been attributed to reduction in particle size; the process has been termed second-stage activation [24].

Since the diffusion of hydrogen atoms is faster through the grain boundaries, where there is lower density of host material, reducing the grain size by ball milling results in a higher density of grain boundaries and faster diffusion of hydrogen atoms to the bulk. Grain boundaries, may also act as heterogeneous nucleation sites for formation or decomposition of hydride phase (Figure 1.3) [13]. Moreover, as the diffusion rate of hydrogen in magnesium

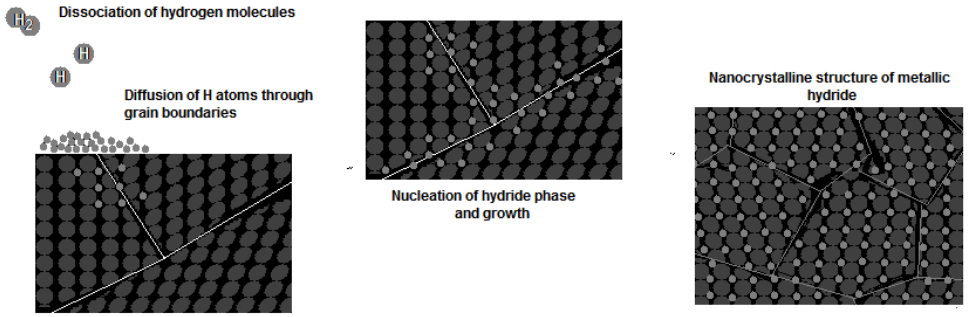

Figure 1.3: Effect of grain size on hydride formation.

hydride is much more slower than in Mg, since a shell of hydride is first formed along the grain boundaries and makes it difficult for further diffusion of hydrogen and formation of further hydride phase, the higher the fraction of grain boundaries is, the less the fraction of Mg inside grains will be; this results in a faster hydride formation [13]. Similarly, desorption of hydride will be faster as well. Also, particle size, which determines the surface reaction rate and hydrogen diffusion distance, is also a key kinetics factor [32].

Ball Milling. Ball milling is a rather inexpensive and efficient route to produce nanocrystalline structure. The disadvantages of ball milling are the contamination induced by the milling media or the atmosphere of milling, and sometimes agglomeration of the soft particles. The mechanism of formation of nanocrystalline structure through ball milling is explained elsewhere [33]. General peak broadening in x-ray diffraction patterns due to reduction in grain size is a typical phenomenon [33, 34]. It is shown that increasing milling time will continuously enhance the kinetics of desorption of magnesium hydride up to a certain degree [13].

1.3.1 Destabilization of Magnesium Hydride

First efforts in destabilizing magnesium hydride by alloying, were made famous by the same two authors 40 years ago [35, 36]. In the first approach Reilly and Wiswall used the Mg-Cu system to show that upon desorption the net heat of MgH_2 formation is reduced by the enthalpy of the intermetallic $MgCu_2$ reaction [35]. The generic representation of the net enthalpy for the dissociation of the hydride and the formation of the intermetallic may be written as a mole-fraction normalized arithmetic subtraction: $\Delta H(system) = \Delta H(hydride) - \Delta H(intermetallic)$. Miedema and co-workers extended this method to a variety of binary and ternary transition metal hydrides [10, 37] and was termed rule of reversed stability. By transforming an intermetallic to a compound alloy hydride (with a lower heat of formation than the binary hydride) it is also possible to reduce the heat of hydride formation. The

Mg-Ni system was used in this case: $Mg_2Ni + 2H \Rightarrow Mg_2NiH_4$ [36]. A detailed theory for calculating and predicting the heat of hydride formation for such ternary compounds may be found in [38]. Unfortunately, this approach often has kinetic limitations due to the difficulty of phase nucleation. This was recently demonstrated for the Mg-Si system, where the net heat of hydride formation was reduced to the desired range by the formation of $MgSi_2$, but the kinetics was too slow for the system to be useful [39]. Intermetallic compounds of transition metals are also considered for destabilizing materials for magnesium (hydride) through the rule of reversed stability; however, no significant change in the thermodynamics were achieved for these composites [40, 41, 42, 43].

1.3.2 Catalyst for MgH_2 Sorption

A suitable catalyst may speed up physical van der Waals adsorption of hydrogen at the surface or its chemisorption as well as diffusion through the bulk of material. Furthermore, catalyst may enhance the hydrogen atoms penetration through the passive film of oxide or hydroxide on the surface to the bulk of material. This is of essential importance for Mg, because of low probability of hydrogen molecules adsorption on the surface (10^{-6}) [13]. Zaluski et al. showed that powders with catalyst do not require activation [31]. For better catalytic result, the catalyst should disperse smoothly on the fine grains of Mg and it should not be encapsulated inside the Mg particles. It is shown that milling of magnesium hydride is a more effective way than milling magnesium as the latter is softer and may develop extensive agglomeration and cold welding [44]

Carbon Materials as Catalyst for MgH_2

Graphite is the most studied carbon allotrope used as catalyst additive to Mg. In a series of reports Imamura showed that graphite by itself has a little effect in the kinetics of Mg sorption in ball milled composites; however, when mixed with organic additives might be quite effective [45, 46]. He proposed role of dangling C-atoms formed from decomposition of graphite during milling as sites for H uptake. In some studies however, MgH_2 composites containing graphite showed better sorption properties; which is attributed to charge transfer between carbon in graphite and Mg before graphite is destroyed [47, 48]. In another study the effect of graphite per se is shown to be only in preventing agglomeration of MgH_2 particles [49].

Effect of addition of carbon nanotubes (CNTs) to metal hydrides, mostly MgH_2, is studied by a number of researchers [47, 48, 50, 51, 52, 53]. Through these studies one can conclude that after a certain degree of milling, depending on the severity of milling, CNTs lose their effect due to destruction of their structure and formation of amorphous carbon. Moreover, although in some studies the effect of pure CNTs is presented [47, 48, 50], the

effect of residual metal particles left from production process of CNTs, although in a very low amount, is sometimes neglected [50, 51]. It is shown in some studies that there is a synergistic effect between CNTs and transition metal (TM) particles on the kinetics improvement of Mg sorption [52, 53]. Furthermore, in most of these studies, CNT is shown to have a positive effect on sorption kinetics of metal hydrides; however there are reports on their decelerating the kinetics [47, 48].

The mechanism through which CNTs improve the kinetics is proposed as their aggregating through grain boundaries of the matrix, acting as hydrogen diffusion routes [53] or their acting as hydrogen pumps [51]. However, in some of the works on MgH_2/carbon material studies the effect of residual metal particles in carbon materials, despite being very effective, has been underestimated or merely neglected. No comparison between multiwalled carbon nanotubes (MWCNTs) and single walled carbon nanotubes (SWCNTs) has been reported.

An important issue in all these metal hydride/CNT composite studies, which is sometimes underestimated, is the effect of milling on the structure of CNTs. Raman spectroscopy is a powerful means to characterize the structure of carbon nanotubes [54]. In a Raman spectrum G-band around 1582 cm^{-1} is a direct evidence of graphite bands between carbon atoms which exists in CNTs as well. Also, D-band at 1350 cm^{-1} whose frequency changes by 53 cm^{-1} as a result of changing laser excitation energy by 1 eV, is representative of structural defects in the structure of CNT. Using Raman spectroscopy, it is shown that in ball milled carbon material/MgH_2 composites structural damages are more severe in the case of graphite compared to MWCNT [47].

The effect of milling on the structure of SWCNTs and MWCNTs has been studied through XRD, Raman spectroscopy, TEM and BET analysis [55, 56]. The structural changes are similar in both cases and can be summarize as follows: initial increase in surface area due to opening of the tubes and then decreased due to entanglement of CNTs into bundles and gradual formation of amorphous carbon [55, 56]; since d_{002} XRD peak intensifies, the D band of Raman spectra intensifies, and Raman quality factor of SWCNTs decreases, indicating that SWCNTs collapse into graphene sheets forming multilayered polyaromatic carbon material [55]. A similar effect can be expected for MWCNTs. No change in outer diameter of MWCNT is observed [56].

The practical sorption temperatures achieved for MgH_2 - CNT composites are barely lower than 300 ^oC. The annealing temperature for magnesium is as low as 150-200 ^oC. Thus, the important question is whether these composites can maintain their performance through cycling at these high temperatures. This issue especially arises where after desorption and formation of Mg, grains tend to coalesce and become larger and eventually the nanocrystalline structure, achieved by high energy ball milling, anneals out. Although MgH_2 is known as a high capacity - cycleable metal hydride, there is a little known on the

effect of cycling on sorption kinetics of ball milled MgH_2; and the works done on this matter are mostly on ball milled mixtures of Mg and TM or TM oxide catalyst [57, 58, 59].

Unfortunately there is a little consensus in the literature on the effect of annealing of the microstructure on cycling kinetics. It is shown that as grain growth occurs through annealing, sorption takes place in two regimes: a fast sorption regime attributed to nano-crystallites, and a very slow regime, attributed to large grown grains; which is due to long diffusion paths and formation of hydride shell in those grains [59]. In contrast, Schimmel et al. believe that defects and distortion in the microstructure of the nano-grains of ball-milled MgH_2 do not play a decisive role in the kinetic improvement of these composites; since through cycling, as these defects are annealed out, the composites still maintain their fast kinetics [60]. They attributed the kinetic improvement to the particle size and high surface area achieved through ball-milling.

Lillo-Ródenas et al. [61] showed that addition of carbon materials can accelerate the desorption kinetics of MgH_2 at 300 ^oC; and in case of metal particle containing carbon materials this improvement is much more significant. Contrary to their own results, they claimed that cycling has a little influence on the performance of the MgH_2/carbon material composites.

It has been shown that covering metallic particles by layers of graphite can protect them from environmental effects [62]. Moreover, carbon is reported to micro-confine lithium borohydride/MgH_2 mixtures [63] or lithium borohydride particles [64, 65] in form of SWCNTs and prevent them from agglomeration and sintering. Through addition of SWCNTs, not only the kinetic was improved, the cycling ability was also enhanced. It is worth mentioning that the working temperature of these mixtures was above 400 ^oC and confinement of particles within a layer of carbon (SWCNTs) seemed very effective in preventing the particles from sintering. However, in these reports there is no discussion on the effect of ball milling on SWCNTs.

Chapter 2 shows how TM containing SWCNTs can improve the kinetics of MgH_2 by lowering the activation energy of desorption through a synergy between the carbon material and metallic nano-particles. The thermal stability over cycling of the optimum composite and its performance is discussed in Chapter 3.

Transition Metals as Catalysts for MgH_2 Sorption

Transition metals have been particularly studied theoretically and experimentally as suitable catalysts for sorption of magnesium (hydride). Most research efforts have been directed at improving the kinetics by mixing MgH_2 with different catalysts using high-energy ball-milling to achieve uniform dispersion of the catalyst. Also, it is known that milling has intrinsic effects on the activation energy for desorption and can reduce its value by up to

50% in the first desorption cycle through formation of deformation twins [66]. It is shown that co-milling of 3d-metal catalysts with MgH_2 may result in lower activation energies and faster sorption kinetics; however the thermodynamics remains unchanged [67, 68, 69, 70]. Hydride former 3d metals such as Ti and V are shown to prevent the oxidation of these metals and preserve their catalytic activity [67]. Fe is proposed as a strong catalyst towards hydrogen sorption of magnesium [40, 41, 68, 70, 71]. It is visually shown, with the aid of SEM, that the kinetics of MgH_2 desorption changes drastically in the presence of Fe catalyst particles; the nucleation of Mg phase occurs in the interface of MgH_2 and Fe [28]. However, different sample preparation might result in different degrees of catalytic effect depending on the degree of dispersion that can be achieved [31].

Intermetallic compounds of transition metals are also considered as catalysts or destabilizing materials for magnesium (hydride). Efforts have been made to destabilize magnesium hydride through the rule of reversed stability; however, no significant change in the thermodynamics were achieved for these composites [40, 41, 42, 43]. Also in Mg-Fe systems, prolonged cycling at temperatures higher than 300 ^oC eventually resulted in formation of Mg_2FeH_6. The resulting material demonstrated high cycling stability at temperatures as high as 350 ^oC, as opposed to magnesium which is attributed to reduced sintering of magnesium [72]. It is worth mentioning that in works on Mg_2FeH_6 there is sometimes a significant amount of leftover Fe, of which the catalytic activity is sometimes neglected [73].

The FeTi intermetallic compound has also been proposed as a catalyst towards hydrogen sorption of magnesium [40, 41, 42, 43, 74, 75, 76]. In some of these works the effect of residual Fe or Ti is overlooked and the entire catalytic effect is merely attributed to certain FeTi or FeTi(Mn) phases [43, 75, 76]. FeTi directly reacts with hydrogen to form $FeTiH_{\sim 1}$ at room temperature and 10 atm hydrogen equilibrium pressure and form $FeTiH_{\sim 2}$ at a higher but not defined plateau pressure [77, 78]. In order to absorb hydrogen though, FeTi should be activated for several times at high temperatures in vacuum and subsequently annealed under hydrogen and finally exposed to high pressure hydrogen after cooling to room temperature [78, 79]. In order to activate the FeTi, annealing the samples at high temperature and/or ball milling the composites under hydrogen pressure is incorporated. This has often involved the decomposition of the catalyst phase and the formation of Fe (and/or Ti) [43, 76], or in some cases there is unreacted Fe [75] or Ti [42] from the intermetallic synthesis process. Excess amount of Ti usually results in formation of titanium hydride which is too stable to desorb in most of the cycling regimes. However, nanocrystalline FeTi, can readily absorb hydrogen with no activation required [78].

Perfect dispersion of the secondary phase can be achieved using sputtering. Zahiri et al. [74] showed that a ternary magnesium based composite prepared by co-sputtering of magnesium, titanium and iron have exceptionally better cycling performance in terms of

both the kinetics and stability against degradation compared to the baseline magnesium or binary Mg-Ti and Mg-Fe sputtered films. They attributed these improvements to possible formation of a semi-crystalline/amorphous FeTi phase or synergistic catalytic effect of titanium and iron. Chapter 4 shows how Fe and Ti can synergistically improve the sorption cycling of MgH_2.

1.4 Thesis Objectives and Scope

The main focus of this thesis is the hydrogen sorption kinetics of catalyzed nano-crystalline magnesium hydride. In this work, I try to illustrate how two different catalysts can synergetically improve the kinetics of hydrogen sorption of magnesium hydride, what is the optimum mixture of the ternary composites and how they perform during sorption cycling. Moreover, the role of each governing parameter on the final behavior of the products is illustrated. Transmission electron microscopy and also X-ray diffraction were used as powerful means to track the microstructural changes resulting from high energy ball milling and hydrogen sorption cycling. Calorimetry and Sievert's techniques were used to measure the sorption kinetics. The grain size analysis was obtained using X-ray methods; to measure the activation energy of desorption for the composites, Ozawa and/or Kissinger methods were incorporated. To have an image of the size of the particles of the products, a variety of techniques such as light scattering, BET surface area, and optical techniques were used.

Chapter 2 describes how TM containing SWCNTs can improve the kinetics of MgH_2 by lowering the activation energy of desorption through a synergy between the carbon material and metallic nano-particles. The optimum mixture of MgH_2 and TM containing SWCNTs is proposed.

Chapter 3 presents the results of our study on the thermal stability over cycling of one hour milled MgH_2 / 5 wt% SWCNT as the optimum composite introduced in Chapter 2. This chapter also illustrates how the TM particles lose their activity during cycling and how SWCNTs can effectively improve the sorption stability of the composite.

In Chapter 4 I present the hydrogen cycling behavior of ball-milled MgH_2-Ti, MgH_2-Fe, MgH_2-Fe-Ti and MgH_2-FeTi mixtures. I show how Fe and Ti can synergistically improve the sorption cycling of MgH_2. To show the synergy, Kissinger analysis was used to measure the activation energies of desorption for all the studied composites before and after cycling. Also, nucleation and growth kinetic models were incorporated to find the rate limiting mechanisms governing the kinetic behavior of the composites.

2

The Influence of SWCNT-Metallic Nanoparticle Mixtures on the Desorption Properties of Milled MgH_2 Powders

Material in this chapter has been published in:
Amirkhiz B, Danaie M, Mitlin D. Nanotechnol. 2009;20:204016.

2.1 Introduction

Rather than acting as a storage media, single-walled (SW) and multi-walled (MW) carbon nanotubes (CNT's) are increasingly being utilized to improve the elevated temperature hydrogen sorption kinetics of magnesium and other hydride forming materials. The first study on the subject was by Chen et al. [51]. The authors mixed metallic magnesium with 5 or 20 weight percent large diameter ($>$ 50 nm) MWCNTs and with 0.5wt.% Zr and 3wt.% Ni powders. They then reactively ball milled the composites under a hydrogen atmosphere. The authors found that the 20wt.% MWCNT composite had unacceptably low gravimetric capacity while the 5wt.% one was similar to the normal capacity of magnesium powders. The authors observed an accelerated sorption rate with the 5wt.% MWCNT composite and prolonged cycling stability.

Dehouche et al. [52] examined the effect of additions of single walled carbon nanotubes (SWCNTs), graphite and activated carbon on the sorption kinetics of Ti/Zr doped Na_3AlH_6 hydride. The nanotubes were purified and co-mechanically milled with the alanates. The authors found that the addition of SWCNTs promoted the formation of Na3AlH6, as compared to the same alanate mixture milled without them. They found that doping the alanate with the SWCNTs yielded improved adsorption and desorption kinetics relative to the graphite and activated carbon-doped composites. The sorption enhancement was attributed to the

high hydrogen diffusivity through the nanotube matrix and enhanced thermal energy transfer. Another group looking at the effect of adding various carbon structures on the sorption performance of Ti-doped sodium alanates reached a similar conclusion regarding the SWCNTs being the optimum catalytic structure [80]. The authors provided a different explanation for this effect, attributing it to enhanced hydrogen spillover mechanism driven by the unique structure of the SWCNTs. No microstructural characterization was performed in that study.

Wu et al. [81] examined the effect of using SWCNT on the adsorption and desorption behavior of MgH_2. The authors added either as-prepared 5wt.% (SWCNT-40wt.% Fe/Co/Ni particle) mixtures, also containing amorphous carbon and other carbon structures, or purified SWCNTs to MgH_2. They co-milled the composites and tested their hydrogen sorption. Since milling was performed in stainless steel vials, some Fe contamination (0.5 - 0.8wt.%) was also present in the samples. The workers observed that while both types of additions accelerated the sorption kinetics, the as-prepared SWCNTs worked better, presumably due to the presence of the metallic particles used for the SWCNT growth. Interestingly, scanning electron microscopy (SEM) and limited transmission electron microscopy (TEM) analysis of the post-milled composites failed to detect any presence of the SWCNTs. In another manuscript, the same group also looked at a variety of additions to MgH_2, including purified SWCNTs (metal content $<$ 1wt.%), graphite, activated carbon, boron nitride nanotubes, fullerenes and asbestos [50]. The authors reported that the sorption kinetics are improved by the addition of SWCNTs followed by co-milling. Scanning electron microscopy (SEM) analysis of the MgH_2-SWCNT composites, which were co-milled for 10 hours, did not reveal the presence of intact nanotube structures.

Subsequent studies with either SWCNT or MWCNT reported similar kinetic enhancements with the additions of SWCNTs, providing a variety of explanations for this effect [47, 50, 53, 61, 82, 83]. However, in all cases, many unknowns remain regarding the final processed microstructure and how it affects sorption. In fact, there is considerable disagreement in literature regarding what is the microstructure of an "optimized" hydride-CNT composite, as well as to the factors leading to performance degradation. A large part of this controversy stems from the complexity of the system, where the ultimate sorption behaviour depends on multiple microstructural parameters. Not only do the defectiveness and the morphology of the nanotubes evolve during mechanical milling, but so may the particle size, the grain size and the degree of strain in the hydride powders. To our knowledge, there has not been a systematic study that separates the influence of CNTs on the evolution of the hydride microstructure during milling from the concomitant milling-induced changes in the CNTs themselves.

In this study we seek to systematically examine how co-milling effects the MgH_2 and

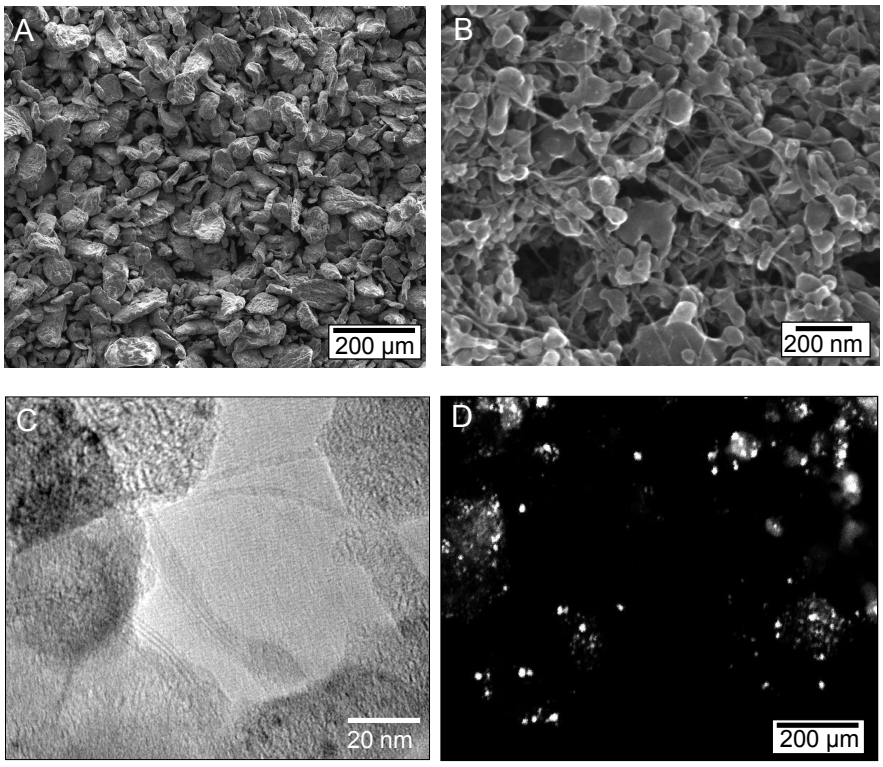

Figure 2.1: (A) SEM micrograph of the as-received MgH_2 powder; (B) SEM micrograph of the as-received SWCNT-amorphous carbon-metallic nanoparticle mixtures; (C) HRTEM micrograph of the SWCNT-amorphous carbon-metallic nanoparticle mixture. (D) Z-contrast HADF micrograph of metallic nanoparticles in the as-received SWCNT mixture.

SWCNT microstructure, using identically milled MgH_2 powders as a baseline. In addition to "conventional" hydride characterization methods, we utilize cryogenic-stage TEM to elucidate the magnesium hydride microstructure. In parallel, we seek to establish a clear relationship between the milled microstructures and the hydrogen desorption properties.

2.2 Experimental Procedure

Magnesium hydride (MgH_2) powder was purchased from Gelest Inc® with 97wt.% purity, the balance being magnesium. SWCNTs were fabricated using an induction thermal process [84] and were utilized in their as-processed state. The composition of the material was determined to be approximately 60wt.% amorphous carbon, 30wt.% SWCNTs with various bundle sizes (individual SWCNT have a diameter of about 1.4 nm), and 10wt.% of metallic nanoparticles (alloys containing Y-Co-Ni or Fe-Mn) used for SWCNT growth. Independent analysis confirmed these weight ratios and alloy content. Since the SWCNTs all came from the same batch, the catalyst makeup of each hydride-SWCNT composite sample should be nearly identical.

Figure 2.1 shows the as-received materials used in this study. Figure 2.1A is a SEM micrograph of the as-received MgH_2 powder. The particle maximum dimensions are in the sub-100 μm range. A quantitative particle size distribution of the milled powders will be provided in Figure 2.3. Figure 2.1B shows a SEM micrograph of the as-produced amorphous carbon - SWCNT - metallic nanoparticle mixture. Some of the coarser SWCNT bundles are visible in the micrographs though most of the metallic nanoparticles, being in the sub 25 nm range, are not. Figure 2.1C shows HRTEM micrographs of the mixture. Visible in the image are several SWCNT bundles of various sizes along with a small metallic nanoparticle. Figure 2.1D shows a Z-contrast high angle annular dark field (HAADF) TEM micrograph of the metallic nanoparticles in the as-received SWCNT mixture. This micrograph shows a typical size and morphology distribution of the SWCNT growth catalytic nanoparticles in the as-received composite.

We combined the hydride powders with 5wt.% of the (amorphous carbon - SWCNT - metallic nanoparticle), using the pure MgH_2 powder as a baseline. For purpose of brevity, in this study we refer to this exact mixture as MgH_2 - SWCNT composites, with the understanding that they also contain amorphous carbon and metal particles. The composite was milled for 30 minutes in a Fritsch Pulverisette 6 planetary mono-mill. We used 10:1 ball to powder weight ratio, with agate balls and vial, at 650 rpm rotation speed. Milling and all the sample handling were done inside a high purity argon filled glovebox with amount of oxygen and water vapour of less than 0.1 ppm.

The SWCNTs were co-milled with the MgH_2 powder for either the entire duration or only for a certain number of minutes right at the end of the milling cycle. For the baseline analysis, the as-received MgH_2 powder, without the SWCNTs, was milled at identical conditions. The labelling scheme for the samples was the following: M stands for milled MgH_2 powder; following M is the amount of time of the milling; C means that carbon nanotubes were also co-milled with the hydride; following C is the amount of time that the carbon nanotubes were co-milled. For example, M1h means the MgH_2 powder, without the SWCNTs, was milled for 1 hour. M1hC1h indicates that the hydride was co-milled with the SWCNTs for 1 hour, while M1hC30m indicates that the hydride was milled for 1 hour with the SWCNTs were added in the last 30 minutes. MgH_2 powders were milled at various durations ranging from 30 minutes to 72 hours. MgH_2-SWCNT composites were co-milled at times up to 72 hours. The 72 hour milled samples showed some magnesium oxide formation, and was deemed unsuitable for direct comparison with the rest of the batches.

We used a simultaneous differential scanning calorimeter (DSC) and thermogravimetric analyzer (TGA) (SDT Q600, TA Instruments) to monitor the desorption behavior of the powder samples. During thermal analysis, the powders were held in alumina cups and heated to 600 °C with 10 °C/min heating rate. Additional isothermal desorption tests

were performed at 300 °C. The analysis was performed under constant flow of high-purity (99.998% pure) argon to prevent oxidation.

Kissinger [85] and Ozawa [20] methods were employed to measure the activation energy of desorption. The method developed by Kissinger allows for obtaining the activation energy for a chemical reaction of any order by considering the variation of the temperature at the maximum reaction rate. In the case of endothermic hydride to metal transformation, the maximum reaction rate is straightforward to obtain from the constant heating rate DSC data and corresponds to the minimum of the desorption DSC peak. The Kissinger analysis can be expressed in the following form:

$$\frac{d(\ln \phi/T_m^2)}{d(1/T_m)} + \frac{E}{R} = const. \tag{2.1}$$

where ϕ is heating rate, T_m is the absolute temperature at the maximum reaction rate, E is the activation energy and R is the gas constant. The activation energy is obtained from a linear plot of $ln(\phi/T_m^2)$ versus $1/T_m$.

According to the Ozawa method an Arrhenius chemical reaction can be expressed in the following simplified form:

$$\log \phi + 0.4567\frac{\Delta E}{RT} = const. \tag{2.2}$$

where T is the absolute temperature at a certain amount of conversion. Therefore the activation energy for the process may be obtained by plotting $\log \phi$ versus $1/T$. Here we used the constant heating rate TGA analysis to obtain the temperature at 80 wt% MgH_2 to Mg conversion. For both types of analyses the heating rates used were 10, 20, 25 and 30 degrees per minute.

For a qualitative analysis of the as-received powders we used scanning electron microscopy (SEM). We used Hitachi S-4800 SEM operating at 7 kV accelerating voltage, and imaging using secondary electron signal. The powder samples where mounted on conductive carbon tape onto SEM stubs in an argon glove box before microscopy session.

We used a Malvern 2000SM Mastersizer laser scattering particle size analysis system to obtain quantitative MgH_2 particle size distributions. The manufacturer specified resolution range of the system was sub-μm to 2 mm. An anhydrous alcohol reagent (Anhydrous Ethyl Alcohol 90% ± 1% v/v; Methyl Alcohol approx. 5% v/v; 2-Propanol approx. 5% v/v as dispersant), was used as suspension media. All samples were ultrasonicated for equal durations prior to measurement. All measurements were performed in same stirring speed and obscuration level.

We used a Bruker-AXS, D8 Discover diffractometer system with an area detector and Cu-K radiation for X-ray diffraction (XRD) experiments. X-ray diffraction was used for general phase identification. XRD spectra were also analyzed for grain and lattice strain

measurement. Integral breadth analysis (IBA) was utilized for de-convoluting the broadening effects of grain size and lattice strain for the powders. Using the following relation [86].

$$(\delta 2\theta)^2/\tan^2\theta_0 = K\lambda/D(\delta 2\theta/\tan\theta_0 \sin\theta_0) + 16e^2 \tag{2.3}$$

and plotting $(\delta 2\theta)^2$ versus $(\delta 2\theta/\tan\theta_0 \sin\theta_0)$, where $\delta 2\theta$ is the integral breadth of the peaks, and θ_0 is the position of the peak maximum. K is a constant taken as 0.9 and λ is the x-ray wavelength (1.54). The grain size (D) and microstrain (root mean squared strain) (e) can be calculated from the fitted line slope and ordinate intercept, respectively. The strain peak broadening is due to the presence of dislocations in the material. We used the first three α-MgH_2 peaks for the analysis. These peaks were well resolved from the peaks of other potentially present phases, e.g. magnesium and magnesium oxide. Peak fitting was performed on EVA^{TM} commercial software. Instrumentation broadening was automatically accounted for in the analysis. While this type of analysis is useful for predicting general trends during milling, the exact grain size values should be interpreted cautiously. This is because the presence of twins and stacking faults in the microstructure results in a reduced measured grain size D, relative to what one would directly observe using TEM [87].

TEM analysis was performed using the JEOL 2010 and JEOL 2200FS microscopes, both operating at 200kV accelerating voltage. The TEM analysis of α-MgH_2 was performed using a cryogenic holder held near 90 K. This was done to significantly increase the stability time of the hydride powder under the electron beam. At cryogenic temperature, sample degradation occurred relatively slowly. Even in the milled sample, negligible weakening of the reflections occurred after several minutes of beam exposure of one area, which was long enough to do the analysis. TEM samples were prepared inside argon-filled glovebox, by dry dispersion of the powders on amorphous carbon grids, directly before the TEM session. We used the commercial software, Desktop Microscopist^{TM}, for simulating experimental electron diffraction patterns. The crystallographic data reported in [88] as well as data from the XRD database on EVA software were used for generating the simulations (data tabulated in Table 2.1). In the simulation, hydrogen superlattice reflections were excluded since their intensity is significantly less than that of the magnesium.

HRTEM analysis was used to investigate the presence and the morphology of SWCNTs in the co-milled powders. We also used Raman spectroscopy to track the structural changes of the SWCNTs versus ball milling time. Raman spectra of the MgH_2 - SWCNT composites were obtained with a HORIBA iHR550 using 770.5 nm at 6.63W, collected in the backscattering geometry at room temperature.

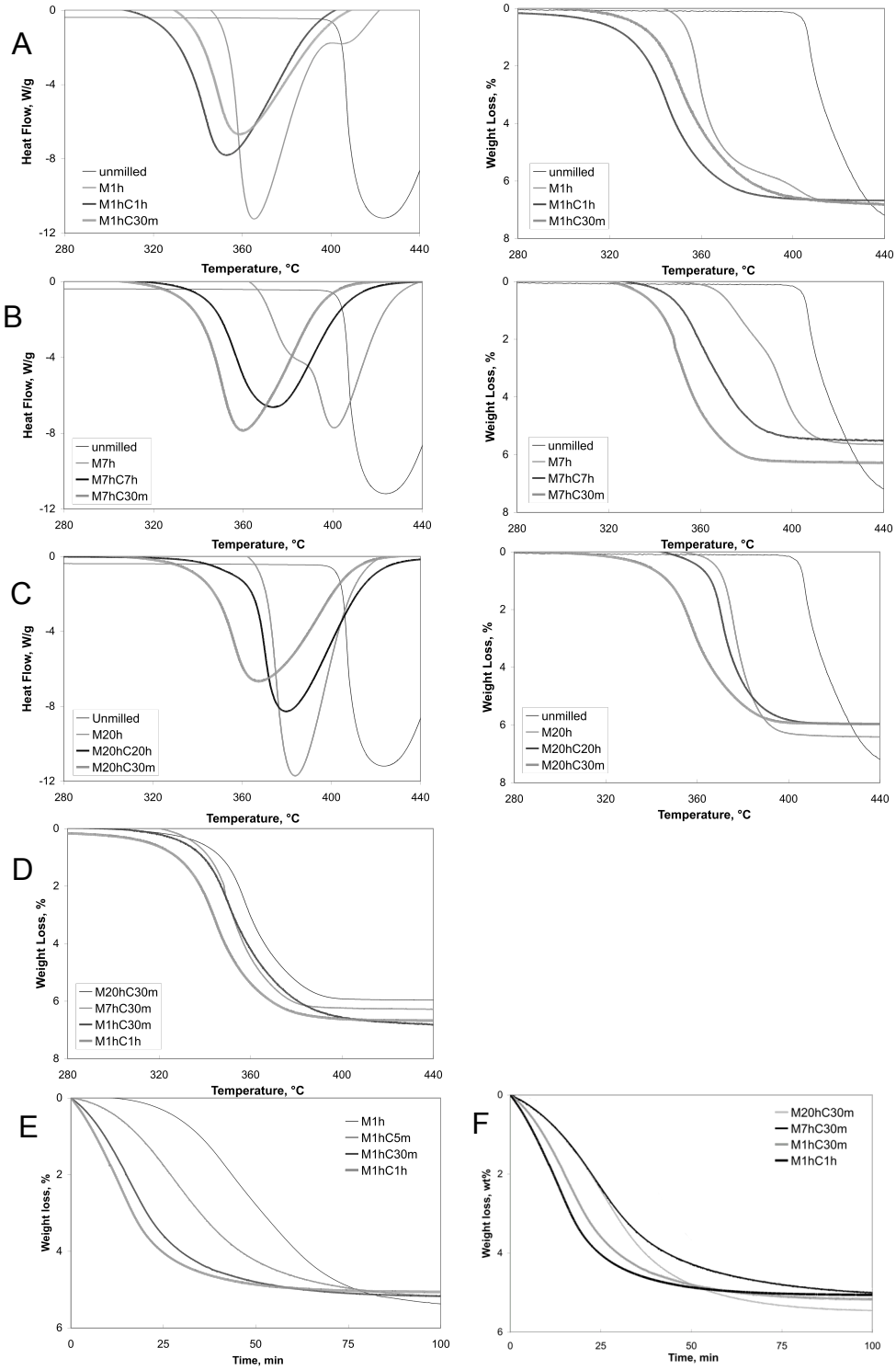

Figure 2.2: Constant heating rate DSC and TGA results for milled MgH_2 powder by itself and co-milled with 5wt.% SWCNT mixtures: (A) 1 hour milling; (B) 7 hours milling; The SWCNT mixtures were added either at the beginning of each milling cycle (M7hC7h, etc.), or in the last 30 minutes (M7hC30m, etc.). Constant heating rate DSC and TGA results for milled MgH_2 powder by itself and co-milled with 5wt.% SWCNT mixtures: (C) 20 hours milling. (D) Best performance TGA data for each milling time.(E) Isothermal TGA desorption results for milled MgH_2 powder by itself and (F) co-milled with 5wt.% SWCNT mixtures.

Table 2.1: Crystallographic data used for generating electron diffraction simulations.

Phase	Space Group	Unit Cell (nm)			Wyckoff Positions
		a	b	c	
α-MgH_2	$P4_2/mnm$ (136)	0.45176	0.45176	0.30206	Mg (2a): 0, 0, 0 H(4f): 0.304, 0.304, 0
γ-MgH_2	Pbcn (60)	0.45246	0.54442	0.49285	Mg (4c): 0, 0.3313, 0.25 H(8d): 0.2727, 0.1089, 0.0794
Mg	$P6_3/mmc$ (194)	0.32095	0.32095	0.52107	Mg (c2): 0, 0, 0
MgO	Fm-3m (225)	0.4227	0.4227	0.4227	Mg (4a): 0, 0, 0 O(4b): 0.5, 0.5, 0.5

2.3 Results

Figure 2.2 shows the constant heating rate differential scanning calorimetry (DSC) and thermal gravimetric analysis (TGA) results for the MgH_2 - SWCNT composites, as well as the baseline as-received and milled MgH_2. The heating rate used for all specimens was 10 °C/min. The DSC endothermic peaks agree with the TGA results in terms of detecting the onset of hydrogen desorption. Integrating the endothermic peaks yields values in the range of 75 kJ/mole hydrogen, associated with the decomposition of α-MgH_2 to Mg and H_2 [89]. Figure 2.2A shows the 1 hour milled data. Judging from the DSC results, the as-received MgH_2 powder begins hydrogen desorption at over 400 °C. The milled MgH_2 powder begins to desorb near 350 °C. The best performance is achieved in the 1 hour co-milled powders, where hydrogen evolution begins to occur below 320 °C. Samples milled for a total of 1 hour, but with the SWCNTs added at the last 30 minutes, display an intermediate performance between the two.

Figure 2.2B demonstrates that the 7 hour co-milled powder performs better than 7 hour milled baseline MgH_2, which performs better than the as-received MgH_2. However, optimum properties are obtained in the samples where just the MgH_2 was milled for 6.5 hours followed by co-milling during the last half an hour. The difference in the performance of the 20 hour (Figure 2.2C) co-milled batches and that of the milled MgH_2 baseline is fairly small. Both desorb better than the as-received powder. Adding the SWCNTs in the last 30 minutes of milling provides for the best overall desorption enhancement. Figure 2.2D shows the best kinetics of each milling time. The fastest constant heating rate desorption is achieved for the 1 hour co-milled powders. Within the times tested, no additional benefits are observed as a result of additional milling. In the case of the 7 and 20 hour batches, adding the SWCNTs during the last 30 minutes provides for significantly enhanced desorption over the co-milled powders.

Figures 2.2E and 2.2F show isothermal 300 °C TGA results for the milled powders. Figure 2.2E demonstrates that for the milling duration of 1 hour, co-milling with the SWCNTs is optimum. The additions of SWCNTs in the last 5 and 30 minutes of milling are not

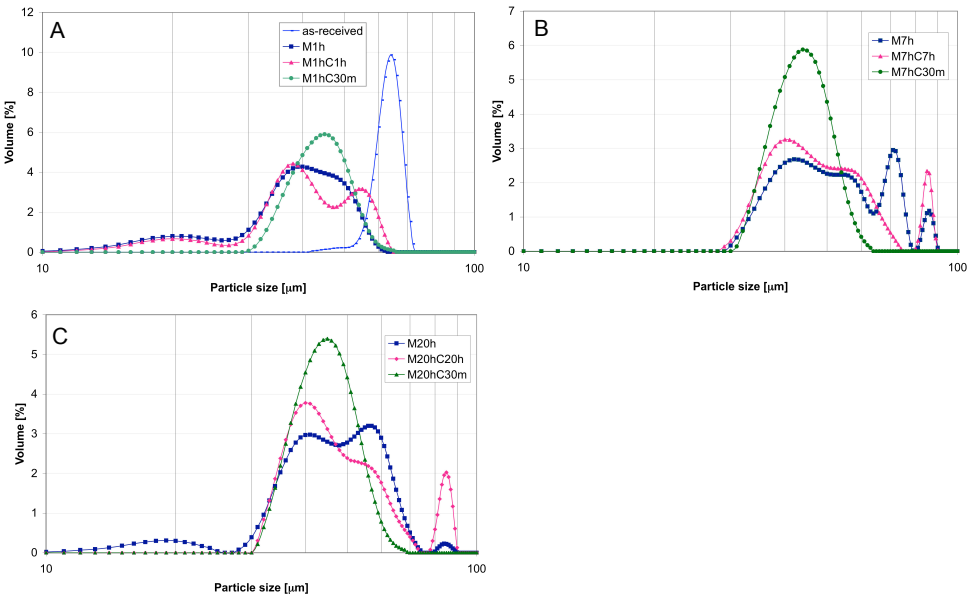

Figure 2.3: Particle size distributions for the baseline hydride, the hydride co-milled with the SWCNTs for the entire duration and the hydride where the SWCNTs were added during the last 30 minutes. (A) 1 hour milling; (B) 7 hours milling; (C) 20 hours milling.

as effective. Figure 2F shows the best-of-the-lot isothermal results, again confirming that the 1 hour co-milled powders are optimum. Milling for longer times, with or without the SWCNTs, actually degrades the performance.

Finally, it is important to indicate that the results obtained here may not necessarily represent the most optimized process conditions. Other variations on co-milling, such as milling for 1 hour followed by co-milling for 1 hour, may yield even lower desorption temperatures. Variations in the respective weight ratios of the two powders may also affect the kinetics. What we observe here though are some systematic trends that we will now correlate to the microstructure of the composites.

Figures 2.3A - C show the particle size distributions of the milled powders, as a function of milling time. The SWCNTs were too small to be detected by this measurement technique and don't show up in the distribution. Some hydride particles are also finer than what is resolvable by the instrument, since they are thin enough to be electron transparent for TEM analysis. However, these particles are in the minority. The results are fairly consistent: Milling reduces the particle size while introducing a multi-modal particle size distribution into the powders. Co-milling for the entire duration does not produce any obvious trends in the size distributions, still resulting in multi-modal curves. Adding the SWCNTs in the 30 minutes has the effect of de-agglomerating the powders.

Figures 2.3A - C indicate that the batches where the SWCNTs were added in the last 30 minutes have a monomodal size distribution, whereas the baseline and the co-milled powders

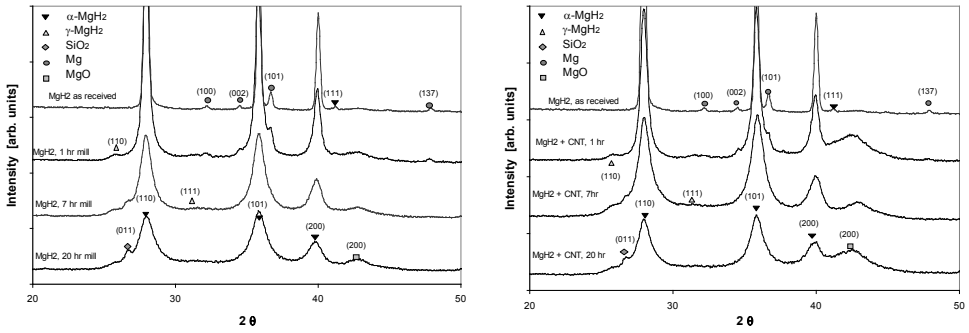

Figure 2.4: Raw XRD results for the milled hydride and the hydride co-milled with the SWCNTs for the entire duration.

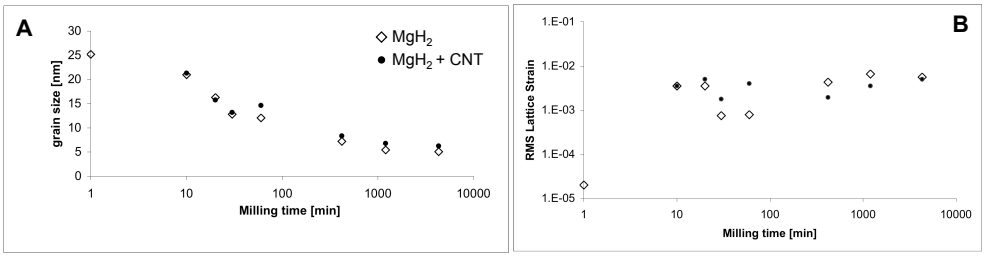

Figure 2.5: XRD IBA analysis grain size (A), and root mean square (rms) strain (B), for the baseline hydride and hydride co-milled with the SWCNTs for the entire duration.

are multimodal. The SWCNTs effectively act as a "lubricant" for the milling process, de-agglomerating powders that would be otherwise mechanically stuck together. The SWCNT bundles are sheared during the milling process, acting as a lubricant similar to the action of graphite. Once the SWCNT structures are destroyed, and only the amorphous carbon remains, the de-agglomeration effect is lost.

Figures 2.4A and 2.4B show the raw XRD data for the milled powders, with and without the SWCNTs respectively. The vast majority of the powder is composed of the thermodynamically stable α-MgH_2. The as-received powder also contains a small amount of Mg. With prolonged milling the α-MgH_2 peaks broaden. Milling for 1 hour and longer promotes the formation of the metastable γ-MgH_2 phase. Judging from the relative peak intensities, the amount of this phase is fairly minor and is quite similar for the baseline and the SWCNT containing powders. Overall it can be concluded that the addition of SWCNTs does not affect the diffraction patterns in any appreciable way. This means that the SWCNTs do not promote a formation of any new phases nor do they change the width or the relative intensity of the magnesium hydride diffraction peaks. As will shown in the next set of figures, the grain size and the microstrain in the MgH_2 is also independent of the SWCNT presence. This also clearly indicates that SWCNTs do not accelerate the sorption kinetics by changing the MgH_2 microstructure.

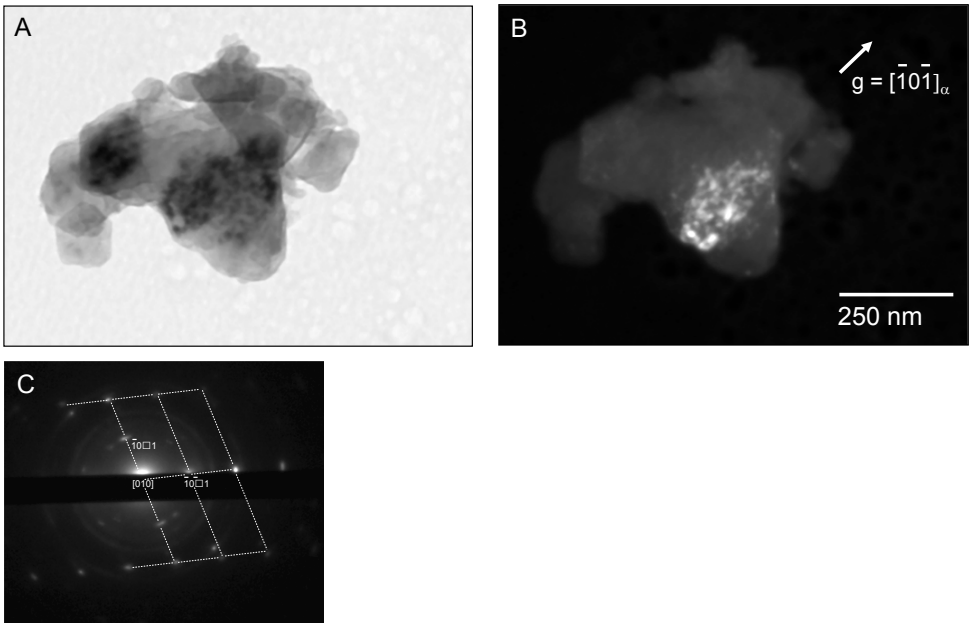

Figure 2.6: (A): Bright field micrograph of several particles from the batch that was co-milled with SWCNTs for 1 hour. (B) and (C): Dark field and corresponding SAD of an individual hydride crystallite within the largest particle.

Figure 2.5A shows the IBA grain diameter, obtained from the XRD curves, as a function of milling time. The as-received MgH_2 powder starts out nanocrystalline. Milling further reduces the grain size, with no discernable difference between the baseline MgH_2 or the MgH_2 - SWCNT mixtures. Figure 2.5B indicates that milling does introduce significant rms lattice strain into the microstructure. However, neither prolonged milling nor the presence of SWCNTs affects the amount of strain past the initial 10 minutes of milling.

Figures 2.6 and 2.7 illustrate the two predominant microstructural features observed in α-MgH_2 via TEM. First, most of the observed hydride powder particles were polycrystalline, with nanoscale grain sizes. Second, the larger hydride grains were multiply twinned. To our knowledge, this second observation has never been reported in literature. These two features were identically present in the baseline and the co-milled powders. Since the hydride powder was very unstable at room temperature under the electron beam, it is only through the use of a cryogenic sample stage that we were able to make these observations.

Figures 2.6A and 2.6B show bright field and dark field TEM micrographs of the 1 hour SWCNT co-milled MgH_2 powder. The large α-MgH_2 grain imaged in Figure 6B was obtained using the g = $[\text{-}10\text{-}1]_\alpha$ reflection, shown in Figure 2.6C. Occasionally, it was possible to image the entire particle in dark field using a single reflection. However, more often the particles were polycrystalline with grain sizes roughly on the same order of magnitude as determined by XRD analysis. The grain in Figure 2.6B shows mottled (non-uniform, blocky) contrast, previously reported for highly deformed ionic minerals such as phyllosil-

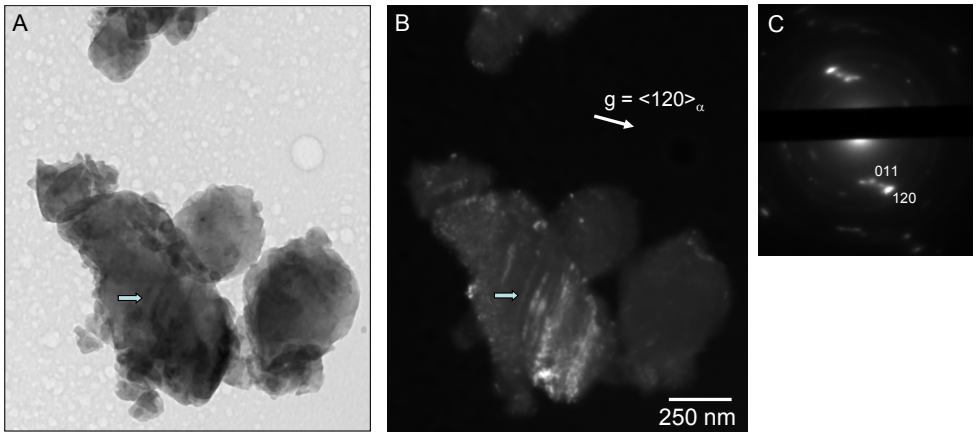

Figure 2.7: (A): Bright field micrograph of several MgH_2 particles from the batch that was co-milled with SWCNTs for 1 hour. (B) and (C): Dark field micrograph and corresponding SAD of the twins within the hydride grains (arrowed).

icates [90, 91]. It is tempting to indicate that this is the first direct observation of the high dislocation content in the magnesium hydride induced by the milling process. This observation would also confirm much of what has been surmised from indirect XRD-based evidence regarding the effects of milling on the hydride microstructures. However, electron beam damage may also be responsible for such contrast and more work is needed to separate the two effects. Figures 2.7A - 2.7C provide an example of a multiply twinned structure observed in the larger hydride crystallites. The density of twins varied from grain to grain, with the smaller crystallites normally not containing any at all. The twins were virtually undetectable in bright field mode but showed up clearly in dark-field. The dark field micrograph in Figure 2.7B was obtained using the g = $<120>_\alpha$ type reflection. Since the grain was far from a symmetric zone axis, the relative spot spacing was used to identify the labeled g vectors. Researchers generally assume that mechanical milling of magnesium hydride induces strain and grain size reduction. This may be the first evidence to show that mechanical milling also induces deformation twins. If mechanical milling did introduce twinning into the α-MgH_2 microstructure, it would, in a fundamental way, change the understanding of sorption kinetics in this important material. In fact, we believe that the twin interfaces in addition to the dislocation cores act as the fast paths for hydrogen diffusion out of the system. The twinned interface may also be point of initiation for the α-MgH_2 to Mg transformation. However a more systematic study is needed to conclusively confirm both hypotheses. It can now be stated that all the α-MgH_2 microstructural features of the two materials, including the grain size, strain and twin content, are unaffected by the presence of SWCNTs.

Finally, we should point out that the microstructures shown in Figures 2.6 and 2.7 are clearly from the hydride rather than the desorbed magnesium or MgO. While upon

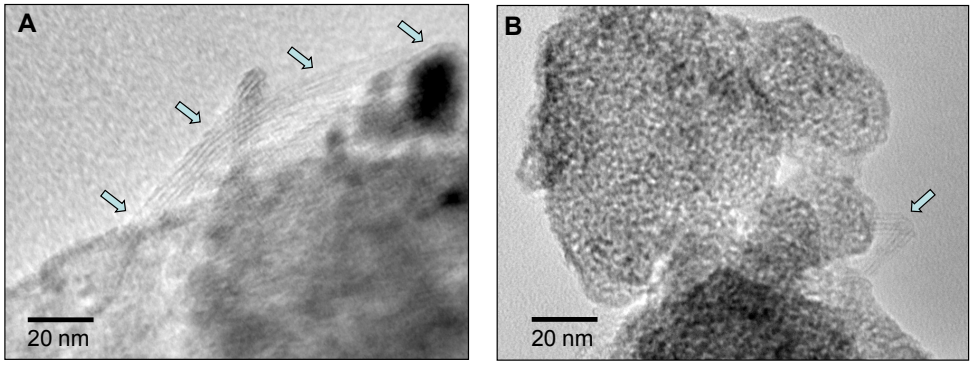

Figure 2.8: HRTEM images of SWCNTs attached to MgH_2 particles. A) MgH_2 + SWCNT composite co-milled for 30 minutes. B) MgH_2 + SWCNT composite co-milled for 60 minutes. Arrows in the image point to the SWCNTs, except for the top arrow in (A) which marks a metallic nanoparticle.

prolonged beam exposure the hydride did transform, the process was straightforward to track: Single grains of α-MgH_2 that were tens or even hundreds of nanometers in diameter would transform to a dense distribution of randomly oriented crystallites that were on the scale of single nanometers.

Figure 2.8A shows a HRTEM micrograph of several SWCNTs (arrowed) and a metallic nanoparticle (arrowed) attached to a hydride particle, obtained from a batch that was co-milled for 30 minutes. After 30 minutes of co-milling, the SWCNTs, with long sections still intact, covered the MgH_2 grains. After 1 hour of milling (Figure 2.8B), SWCNTs were still detectable covering the hydride particles. However, their sections were now much shorter and the bundles appeared broken (arrowed). Extensive search for SWCNTs in the 7 hour co-milled powders did not yield any evidence of their existence. Only amorphous carbon and metallic nanoparticles were detected. Both were lining the surfaces of the hydride particles.

Figure 2.9 shows a bright field and a Z-contrast high angle annular dark field (HAADF) TEM micrograph of the 72 hour co-milled powders. The microstructure was purposely over-milled to examine the evolution of the size/morphology of the microstructure as a function of milling. These samples show no trace of any graphitic bonds in the carbon, but clearly show the presence of metallic nanoparticles. Three such remaining nanoparticles are arrowed in Figure 2.9B. The composition of the largest of the three particles was determined by EDXS to be Mn-Fe based. A comparison of the sizes and morphologies of the metallic particles in the as-received SWCNTs (Figure 2.1D) with the particles shown here yields no obvious trend in their size or morphology evolution. Hence, we can conclude that while milling drastically affects the structure of the SWCNTs, the metallic nanoparticle phase appears fairly unaffected. This may be explained by the fact that the particles are largely encapsulated by carbon that prevents nanoparticle agglomeration or significant alloying with the hydride.

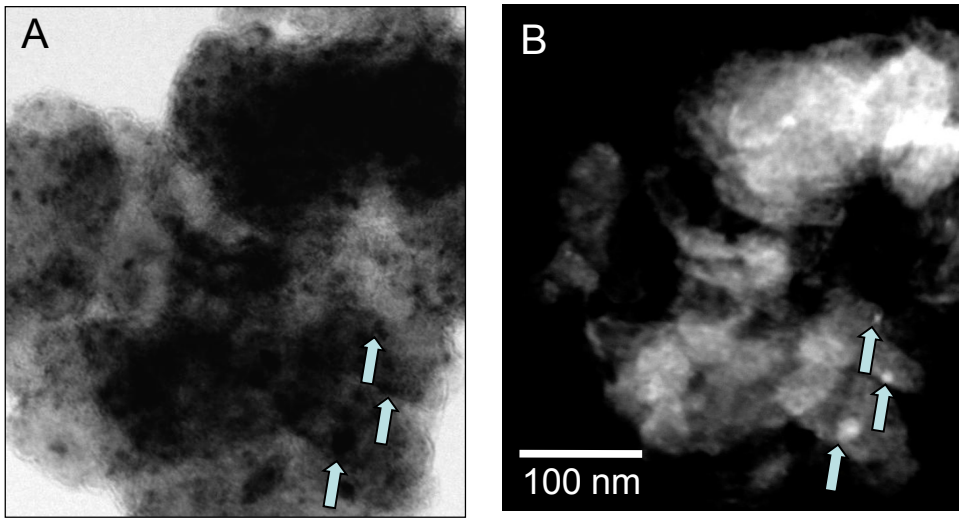

Figure 2.9: Bright field and Z-contrast HAADF STEM micrographs of metallic nanoparticles (arrowed) on the hydride powder surface after 72 hours of co-milling. EDXS confirmed that the lower arrowed particle is Mn-Fe based.

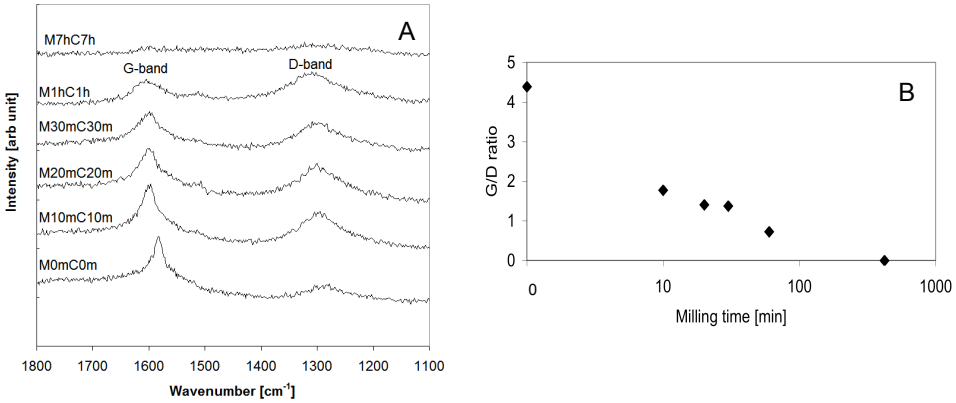

Figure 2.10: (A) Raman spectra for hydride - SWCNT mixtures co-milled for various durations; (B) G-band to D-band ratio as a function of milling time.

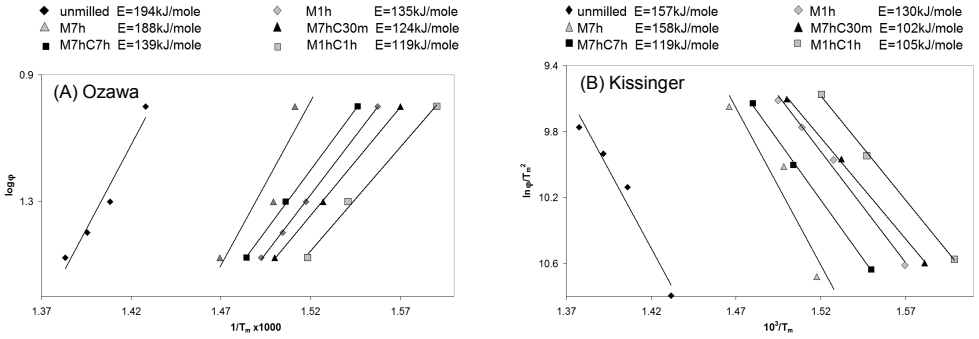

Figure 2.11: Constant heating rate analysis for activation energy of desorption (A) Ozawa TGA-based analysis using 80% reaction completion by weight. (B) Kissinger DSC-based analysis using maximum reaction rate.

Figure 2.10A shows the Raman spectroscopy results for the MgH_2-SWCNT composites as a function of milling time. The spectra clearly shows a peak around 1580 cm^{-1} corresponding to the graphite C-C bands (G-band) that are characteristic of the structure in SWCNTs [54]. The increase in intensity of the D-band, around 1330 cm^{-1}, is an indication of the formation of defects in the structure of SWCNTs [47, 55, 92]. The spectrum after co-milling for 7 hours was similar to that of amorphous carbon. Figure 2.10B shows a plot of the intensity ratio of the G versus the D band, also as a function of the milling time. The ratios in Figure 2.10B were calculated from the data in Figure 2.10A, using the maximum intensities of the two bands. Both figures confirm the conclusion that prolonged milling damages and then entirely destroys the SWCNT structure.

2.4 Discussion

We now have enough information regarding the co-milled microstructures to discuss the role of the SWCNT-metallic nanoparticle additions on the sorption behavior of MgH_2. The dissociation of MgH_2 is known to be sluggish even when appreciable thermodynamic driving force exists. The origin of the kinetic sluggishness is still somewhat debatable, being attributed to several rate-limiting mechanisms: 1) the slowness of the Mg-MgH_2 phase boundary movement due to the slow diffusivity of the hydrogen ions both through the hydride and through the metal [22, 93, 94, 95, 96]; 2) the diffusion of hydrogen along a metal-MgH_2 interface [97, 98]; 3) surface passivation/poisoning due to adsorbed oxygen or sulfur - containing species [99]. 4) the high activation energy of hydrogen dissociation/re-association on a MgH_2 surface [100]; This debate may be to some extent artificial since the degree to which mechanism is the rate limiting one fundamentally depends on the surface preparation and on the bulk microstructure, which vary from experiment to experiment.

Figures 2.11A and 2.11B show desorption activation energy plots obtained from the

Ozawa and the Kissinger analysis, respectively. Though there is an absolute value difference between the two forms of analysis, the trends are fairly consistent. The activation energies may be roughly separated into three classes: The baseline hydride powders and the seven hour milled hydride powders have by far the highest activation energies for desorption. The one hour co-milled powders and the powders that were milled for seven hours with the SWCNTs added during the last 30 minutes possess the lowest activation energies. The one-hour milled magnesium hydride and the seven hour co-milled powders have intermediate values of activation energies. This analysis confirms our previous conclusions that optimum catalytic function is achieved when the SWCNTs are well dispersed throughout the microstructure and are defective. However even in the over-milled state (M7hC7h) some catalytic enhancement is still achieved.

We have shown that the addition of SWCNTs does not influence the amount of grain boundary area, or the dislocation content of the hydride. This can be seen from Figure 2.5. There is also no discernable difference in the twin density with or without the SWCNTs. It is unlikely that the SWCNTs influence the rate of grain boundary or bulk hydrogen diffusion. The SWCNTs would have to be embedded in the hydride particles and have to traverse at least half the thickness of the structure. From our TEM results we see that in the optimum processing condition (1 hour milling) the SWCNTs are truly nanoscale in length and cover the hydride surface. Even if it was indeed possible to embed SWCNTs into the MgH_2 matrix, there are simply no carbon structures that are even remotely on the same scale as the hydride particles. It is also quite unlikely that it would be possible to create a continuous path of broken SWCNTs throughout the bulk of the hydride. Thus, we conclude that the addition of SWCNTs does not influence 1) the rate of the Mg-MgH_2 phase boundary movement or 2) the diffusion of hydrogen along a metal-MgH_2 interface.

Experimental results show that the particle size differences at most have a secondary influence on the temperature where appreciably hydrogen desorption begins. There also does not seem to be a clear trend in the shape of the DSC endothermic peaks being related to width of the particle size distributions. For example, in the case of the 1 hour milled samples, the co-milled powders show more than 30 degree lower onset of desorption relative to the milled baseline. Yet the particle size distribution of the 1 hour co-milled and the baseline powders quite similar. In fact, the main difference between the two is that the co-milled powder shows a secondary peak centered around 55 microns. On the side of the small particles, the two distributions are almost identical. One could argue that in the one hour milled powders the wider size distribution leads to a wider DSC peak. However, this trend is reversed in the 20 hour milled powders. Examining the DSC heat evolution curves for the 20 hour milled samples shows that the sharpest endothermic peak (the baseline hydride) occurs for the powder batch with the widest size distribution (volume fraction peaks centered at

20 μm, 40 μm, 57 μm and 85 μm). Conversely, the widest DSC peak (SWCNTs added in the last 30 minutes) occurs for the batch with the narrowest distribution (a single volume fraction peak centered at 45 μm).

What is observed is that the optimum desorption properties are achieved when the SWCNTs are well dispersed, contain defects and are in contact with the metallic nanoparticles. The desorption properties of both the baseline and the co-milled powders do get worse with increasing milling time, which may be in part due to increasing oxide formation. However it is the desorption enhancement due to the SWCNTs that is reduced when the hydride-SWCNT composites are overmilled and the SWCNTs are destroyed. This could be seen by considering the maximum reaction rate as corresponding to the trough of the endothermic peaks. For example, in the 7 hour milled samples the baseline hydride reaction peak is roughly at 400 °C. If the SWCNTs are added in the last 30 minutes, in which case they survive the milling cycle but are dispersed and damaged, the endothermic peak is at 360 °C. If the SWCNTs and the hydride are co-milled for 7 hours, resulting the complete destruction of the SWCNT structure, the peak is at 375 °C. Since the samples were not removed from the glove box at any point of the milling, the total oxide in each batch should be identical. The remaining catalytic enhancement in the 7 hour (and the 20 hour) co-milled samples relative to the pure hydride baseline is due to the metallic nanoparticles which survive the milling.

We can now conclude that it is SWCNTs presence, in a defective state and coupled to a metal catalyst, which promotes enhanced desorption kinetics. There may be several scenarios by which the SWCNT-metal combinations may be effective. One is that the defective SWCNTs in intimate contact with the hydride particles may act as preferential pathways for hydrogen past the surface of hydroxide. This would relate to decreasing the influence of mechanism 3) surface passivation/poisoning due to adsorbed oxygen containing species. Even in nominally inert environments, α-MgH_2 is always covered by a layer of hydroxide several nanometers in scale [101]. Individual and bundles of SWCNTs could penetrate this thin hydroxide shell, acting as "hydrogen pumps" to move the atoms to the surface. The optimum co-milling time of 1 hour may then be the duration required to firmly embed the SWCNTs into the hydride particles. SWCNTs containing defects would have additional diffusion paths as well. Additionally, the defective SWCNT-metal combination may be catalytically optimum. This would relate to reducing 4) the significant activation energy of hydrogen dissociation/re-association on the surface of a MgH_2 particle. It is well known that the activation energy for hydrogen recombination on pure α-MgH_2 is quite high. The literature quoted values include 144 kJ/mol, 172 kJ/mol, or even 323 kJ/mol (see reference [100] and the citations therein). This is an energy barrier at least twice as high as the heat of formation of the hydride itself (75kJ/mol) [89]. The SWCNT-metal

nanoparticle couples, which cover the hydride surface, may act as preferential low energy sites for hydrogen re-association. The metallic nanoparticles used for SWCNT growth are also known to be catalytic for splitting hydrogen, and their contact with the SWCNTs may be synergistic. Recent Density Functional Theory (DFT) calculations on hydrogen interaction with transition metal-SWCNT combinations support this scenario [82].

2.5 Summary

We examined the role of a combination of SWCNTs and metallic nanoparticles on the hydrogen desorption properties of MgH_2 powders. A nanocomposite of these was created by high energy co-milling for various durations. SWCNT-metallic nanoparticle additions catalyze the desorption of hydrogen, lowering the onset temperature by more than 30 °C over those of identically milled pure MgH_2 powders. However, co-milling for longer than one hour degrades this effect, essentially yielding a similar sorption performance in the pure and the composite powders.

Using Raman spectroscopy and HRTEM analysis, we show that a significant portion of SWCNTs do survive up to 1 hour of milling, though becoming broken and defective in the process. At longer milling times the SWCNTs are completely destroyed and the enhancement is largely lost despite the continued presence of the metallic particles. X-ray diffraction analysis of the α-MgH_2 grain size and strain, and laser scattering analysis of the α-MgH_2 particle size, indicates that the addition of the SWCNT-metallic nanoparticles does not appreciably affect these parameters during milling. Cryo-stage TEM analysis confirmed that the majority of the hydride powder particles were polycrystalline, with nanoscale grain sizes. TEM also revealed that the larger hydride crystallites are multiply twinned. Ozawa and Kissinger constant heating rate analysis conclusively demonstrated that in the optimum processed condition (1hour co-milled) the activation energy for hydrogen desorption is the lowest. Through the process of elimination it can be concluded that the catalytic effect of the SWCNTs is a result of one or a combination of the following effects: During mechanical milling the SWCNTs penetrate the thin surface hydroxide shell and act as "hydrogen pumps"; or the surface dispersed and damaged SWCNTs reduce the high activation energy of hydrogen re-association on the MgH_2 surface.

3

Hydrogen Sorption Cycling Stability and Microstructure of Single-Walled Carbon Nanotube (SWCNT) Magnesium Hydride Nanocomposites

Material in this chapter has been published in:
Amirkhiz B, Danaie M, Barnes M, Simard B, Mitlin D. J Phys Chem C. 2010;114:3265-3275.

3.1 Introduction

Composite metal-carbon nanostructures are a subject of increasing scientific inquiry due to their realized and potential hydrogen storage properties. A "traditional" use of carbon-metal nanostructures is for enhanced cryogenic hydrogen physisorption e.g. [102, 103, 104, 105, 106, 107, 108]. However a recent approach that has achieved notable experimental success is the use of such nanostructures to enhance the kinetics of elevated temperature hydrogen chemisorption in metal and chemical hydrides. Early work on the addition of graphite to promote hydrogenation of magnesium was performed by Imamura and co-workers [45, 109]. Shortly afterwards Bouaricha et al. used a variety of carbon structures to enhance hydriding in Mg_2Ni, Mg, Ti, V and FeTi metals [110, 111]. Subsequent studies purposely combined metallic nanocatalysts with graphite to obtain a synergistic catalytic effect [112, 113]. Of the various carbon structures and allotropes two approaches have shown to be the most successful in enhancing the sorption kinetics. The first approach is the utilization of nanoporous/nanoscaffolded carbon structures for size confinement of the hydride phases e.g. [114, 115, 116, 117]. The second methodology, which is the subject of this study, involves

using carbon nanotubes (CNTs), usually combined with metallic nanoparticles, to enhance the sorption kinetics [52, 53, 61, 64, 65, 81, 82, 80, 118, 119, 120]. In all cases a kinetic sorption enhancement was reported following the co-milling of the powders. For magnesium hydride the summary below covers the pertinent literature.

Wu et al. [81] examined the effects of using purified versus metal-containing (as-prepared) CNTs on the absorption/desorption properties of mechanically-milled magnesium hydride. The authors found that the hydrogen desorption temperature was reduced by as much as 70°C with the incorporation of the as-prepared CNTs into the system. The purified nanotubes were not as effective, lowering the endothermic peak temperature by 40°C relative to the baseline. Using the kinetic Kissinger analysis the authors reported that the activation energy for desorption was lowered from 126 kJ/mol for the baseline MgH_2 powder, to 96 kJ/mol for composite containing the metallic particles and CNTs. The activation energy for the hydride powder containing only the purified nanotubes was effectively the same as of the baseline.

Yao et al. [82] examined the co-catalytic effect of metal (FeTi) nanoparticles and CNTs on the sorption properties of magnesium hydride, using both experiments and Density Functional Theory (DFT). The authors reported a clear synergistic effect on the kinetics of using both catalytic additions versus the one or the other. In addition to the physical contributions that the CNTs had in facilitating mechanical milling, the authors proposed a chemical catalytic role as well. The hypothesized mechanism was essentially that the metallic nanoparticles enhancing hydrogen dissociation(reassociation) whereas the nanotubes provide fast diffusion surfaces/ channels for the hydrogen atoms to enter(exit) the magnesium (magnesium hydride) matrix. At temperatures above 300 °C, the carbon was also predicted to be somewhat catalytic towards hydrogen dissociation. In a subsequent manuscript the same group of authors showed a similar, though even more enhanced, synergistic effect when V-Ti nanoparticles were combined with the CNTs [53].

Lillo-Rodenas and coworkers investigated the addition of a variety of carbon allotropes mixed with Ni or Fe nanoparticles to magnesium hydride [61]. The authors also examined the effect of limited absorption/desorption cycling (up to 5 cycles) on the microstructure and the sorption behavior. They reported enhanced desorption kinetics particularly in the carbon nanofiber containing samples. The multi-walled carbon nanotube (MWCNTs) composites had the peak temperature of decomposition decrease by approximately 20 °C relative to the baseline hydride powder, while the composites with the nanofibers had a temperature reduction of 40 °C. The authors conclusively showed that there was no relationship between the surface area of the carbon materials and the decomposition temperature, since the very high surface area of activated carbon was only marginally effective in changing the desorption characteristics. Another key point that the authors demonstrated was that for a

given carbon material (nanofibers) the metal loading tremendously influences their efficacy. Since the total metal nanoparticle loading was less than 0.4 wt.%, which by itself would not have been enough to achieve a substantial kinetic enhancement, a catalytic synergy was confirmed.

Recent work on the microstructure-sorption properties relations in the CNT - magnesium hydride system was performed by [118]. For microstructural analysis the authors utilized cryogenically cooled sample stage transmission electron microscopy (TEM). This kept the samples at 90K and allowed for direct analysis of the hydride while incurring minimal electron beam-induced artifacts. The researchers found that single walled carbon nanotubes (SWCNT)-metallic nanoparticle additions catalyze desorption of hydrogen, lowering the activation energy by as much as 25 kJ/mol over those of identically milled pure MgH_2 powders. These optimum desorption properties were achieved after 1 hour of high-energy co-milling of the hydride and the SWCNTs. At longer milling times the SWCNTs were completely destroyed and the enhancement was largely lost despite the continued presence of the metallic particles of the same scale as in the as-received materials.

While kinetic improvements in the initial desorption(absorption) behavior are promising results, a viable catalytic system must function through numerous hydrogen absorption/desorption cycles. In the case of the SWCNT (+ amorphous carbon) metal hydride system this issue has received only limited attention. It is thus the goal of the current work. In parallel to characterizing the hydrogen sorption kinetics of SWCNT - magnesium hydride nanocomposites through numerous hydrogenation/dehydrogenation cycles, we aim to elucidate the fundamental surface and bulk microstructural features responsible for the observed trends. By acquiring an in-depth understanding of the structure in these nanomaterials, it will be possible to design and synthesize improved formulations.

3.2 Experimental Procedure

Magnesium hydride (MgH_2) powder was purchased from Gelest® Inc with 97 wt.% purity, the balance being magnesium. Single wall carbon nanotubes (SWCNTs) were fabricated using laser-ablation method [84] and were utilized in their as-processed state. The batches were actually a mixture of approximately 60 wt.% amorphous carbon, 30 wt.% SWCNTs with various wall widths, and 10 wt.% of metallic (alloys containing various combinations of Co, Ni, Fe and Y) nano-particles used for growing the SWCNTs (provider specification). In-house Thermal Gravimetric Analysis (TGA) under air was used to confirm these weight ratios. We combined the hydride powders with 5 wt.% of the mixture (amorphous carbon, SWCNTs, transition metal nano-particles,). For sake of brevity, in this study we refer to this exact mixture as SWCNT - encapsulated MgH_2, with the understanding that the hydride is also covered with amorphous carbon and with metal particles. The mixture was milled

for different durations in a Fritsch Pulverisette 6 planetary mono-mill. We used 10:1 ball to powder weight ratio, with agate balls and vial at 650 rpm rotation speed. Milling and all sample handling were done inside a high-purity argon filled glovebox with the amount of oxygen and water vapor present less than 0.1ppm. The SWCNTs were co-milled with the MgH_2 powder for various durations, though only the 1 hour co-milled samples (optimum properties) were used for sorption cycling. For the baseline analysis the as-received MgH_2 powder was milled for 1 hour.

Volumetric absorption and desorption measurements were performed using a Sievert's hydrogen sorption analysis system (Hy-Energy LLC. PCTPro 2000). All the measurements were carried out at 300°C. Two types of pressures were employed. The MgH_2 and SWCNT-MgH_2 powders that were analyzed for 10 and 35 cycles respectively, were absorbed at a starting pressure of 10 bar (finishing at 7 bar) and desorbed at a starting pressure near 0.1 bar (finishing at 0.4 bar). These are also the specimens that received all the subsequent microstructural characterization. As a follow up to the initial work, we performed extended cycling on the SWCNT-MgH_2 system. Hydrogen was absorbed at a starting pressure of 11 bar (finishing at 4 bar) and desorbed at a starting pressure of 0.04 bar (finishing at 0.2 bar). No additional microstructural characterization was performed on these specimens.

In addition we also used a simultaneous differential scanning calorimeter (DSC) and thermogravimetric analyzer (TGA) (SDT Q600, TA Instruments) to ascertain the hydrogen desorption kinetics. The analysis was performed under constant flow of high-purity (99.998% pure) argon to prevent oxidation. Kissinger analysis [85] was employed to measure the activation energy of desorption. The method developed by Kissinger allows for obtaining the activation energy for a chemical reaction of any order by considering the variation of the temperature at the maximum reaction rate. In the case of endothermic hydride to metal transformation, the maximum reaction rate is straightforward to obtain from the constant heating rate DSC data and corresponds to the minimum of the desorption DSC peak. The Kissinger analysis can be expressed in the following form:

$$\frac{d(\ln \phi/T_m^2)}{d(1/T_m)} + \frac{E}{R} = const \tag{3.1}$$

where ϕ is heating rate, T_m is the absolute temperature at the maximum reaction rate, E is the activation energy and R is the gas constant. The activation energy is obtained from a linear plot of $\ln \phi/T_m^2$ versus $1/T_m$. For this analysis the heating rates used were 10, 20, 25 and 30 degrees per minute.

The effect of co-milling SWCNTs on hydrogen desorption thermodynamics of MgH_2 was investigated using a high-pressure differential scanning calorimetry technique (HP-DSC) used by [121]. The technique relies on heating the samples at various pressures at a sufficiently slow rate that the onset of desorption occurs at an equilibrium temperature as

dictated by the van't Hoff equation:

$$\ln p/p_o = \Delta H/RT - \Delta S/R \tag{3.2}$$

where p is the pressure and p_0 is 1 atm., ΔH is the enthalpy of hydride formation for MgH_2 and ΔS is -130 J/molK. Since desorption in MgH_2 is a single chemical reaction process with no intermediate states, by monitoring the onset of desorption (endothermic) for at least three hydrogen pressures it is possible to obtain relatively accurate values of ΔH. We used a TA Instruments Q20P dedicated pressure DSC system and performed the test at 0.5 °C/min.

To analyze the released gas and confirm negligible hydrocarbon evolution during dehydrogenation we combined mass spectroscopy with thermal gravimetric analyzer and studied the gas evolution. The samples were analyzed on a Netzsch TG/MS/FTIR system (Netzsch TG 209 F1 Iris® coupled to an Aëolos QMS403C mass spectrometer and a Bruker Tensor 27 Fourier Transform Infrared spectrometer via a TGA A588 TGA-IR module) under a flow of ultra high pure argon (99.9993%) to avoid oxidation during the runs. The powders were analyzed in an aluminum oxide crucible and any residual oxygen atmosphere was removed by repeated chamber evacuation and argon gas refill. Powders were heated from ambient temperature to 550 °C at a heating rate of 10 °C per minute, with a 20 minute hold at 120 °C and a 30 minute bake at 550 °C. The mass spectroscopy of evolved gasses was measured from a mass range of 1 to 50 mass units.

To analyze the surface area of the composites and compare them to that of as-milled MgH_2 samples, a Quantachrome Autosorb 1 MP automatic gas adsorption system was used. The system is dedicated to standard measurements of nano-structured materials by nitrogen sorption isotherms at 77K. Multi-point BET surface area measurement was done using AS1Win, version 1.5 software which supports the BET data reduction algorithm. All the samples were degassed at 150 °C under vacuum for at least 5 hours prior to the tests.

X-ray diffraction (XRD) was utilized for grain size and microstrain determination in the as-milled and the cycled samples. A Bruker-AXS, D8 Discover diffractometer system with an area detector and Cu-Kα radiation was used for the XRD experiments. XRD spectra were also analyzed for grain and lattice strain measurement. Integral breadth analysis (IBA) was utilized for de-convoluting the broadening effects of grain size and lattice strain for the powders. Using the following relation [86]: $(\delta 2\theta)^2/\tan^2\theta_0 = K\lambda/D(\delta 2\theta/\tan\theta_0 \sin\theta_0) + 16e^2$ and plotting $(\delta 2\theta)^2/\tan^2\theta_0$ versus $(\delta 2\theta/\tan\theta_0 \sin\theta_0)$, where $\delta 2\theta$ is the integral breadth of the peaks, and θ_0 is the position of the peak maximum, K is a constant taken as 0.9 and λ is the x-ray wavelength (1.54Å) the grain size (D) and microstrain (root mean squared strain) (e) can be calculated from the fitted line slope and ordinate intercept, respectively. The microstrain peak broadening is normally ascribed to the presence of non-uniform lattice

Table 3.1: Crystallographic data used for generating electron diffraction simulations.

Phase	Space Group	Unit Cell (nm)			Wyckoff Positions
		a	b	c	
α-MgH_2	$P4_2/mnm$ (136)	0.45176	0.45176	0.30206	Mg (2a): 0, 0, 0 H(4f): 0.304, 0.304, 0
γ-MgH_2	Pbcn (60)	0.45246	0.54442	0.49285	Mg (4c): 0, 0.3313, 0.25 H(8d): 0.2727, 0.1089, 0.0794
Mg	$P6_3/mmc$ (194)	0.32095	0.32095	0.52107	Mg (c2): 0, 0, 0
MgO	Fm-3m (225)	0.4227	0.4227	0.4227	Mg (4a): 0, 0, 0 O(4b): 0.5, 0.5, 0.5

strain due to dislocations. However twins are also known to contribute to the broadening as well [87]]. We used the first three α-MgH_2 peaks for the analysis. Instrumentation broadening was automatically accounted for in the analysis.

TEM analysis was performed using the JEOL 2010 and JEOL 2200FS microscopes, both operating at 200 kV accelerating voltage. Conventional bight field and dark field TEM analysis of α-MgH_2 was performed using a cryogenic holder held near 90 K. This was done to significantly increase the stability time of the hydride powder under the electron beam [122]. At cryogenic temperature, sample degradation occurred relatively slowly. Even in the milled sample, only slight weakening of the hydride reflections occurred after several minutes of beam exposure of one area. This was long enough to do the analysis. TEM samples were prepared by dry dispersing the powders onto amorphous carbon grids. We used the commercial software, Desktop Microscopist^{TM}, for simulating experimental electron diffraction (SAD) patterns. The crystallographic data reported in were used for generating the simulations. In the simulations hydrogen superlattice reflections were excluded since their intensity is significantly less than that of the magnesium atoms. The table provides the pertinent crystallographic information.

We utilized Raman spectroscopy to track the structural changes of the SWCNTs versus cycling. Raman spectra of the MgH_2 - SWCNT composites were obtained with a HORIBA iHR550 using 770.5 nm at 8 W, collected in the backscattering geometry at room temperature.

3.3 Results

Figures 3.1 - 3.3 provide information on the microstructure and the desorption behavior of the SWCNT-MgH_2 system and of the baseline MgH_2, both systems in the as-milled condition. While the remainder of the manuscript concerns the cycling behavior, these three figures are included to provide the proper background for the subsequent analysis. The as-received SWNCTs are in bundles that are de-agglomerated during high-energy mechanical milling [118]. Figure 3.1A shows a plot of the BET specific surface area versus milling time,

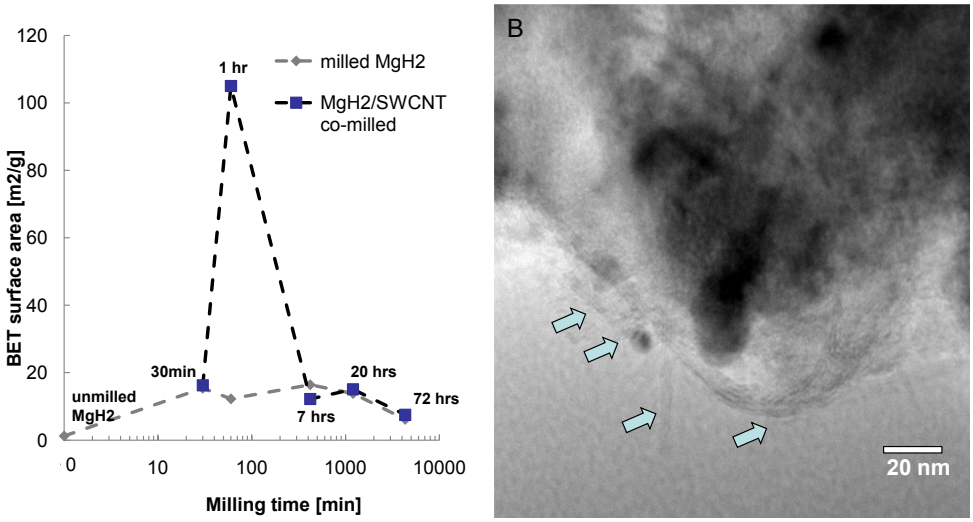

Figure 3.1: A) BET specific surface area versus milling time, for both the SWCNT-MgH_2 system and for the MgH_2 baseline. Optimum dispersion of the SWCNTs on the MgH_2 surfaces is achieved after 1 hour of co-milling, as evidenced by a sharp peak in the BET surface area. B) A TEM micrograph that illustrates the dispersion on the SWNCTs on the MgH_2 metal surfaces. The arrows in the figure point to the regions where the MgH_2 is clearly in contact with the SWCNTs.

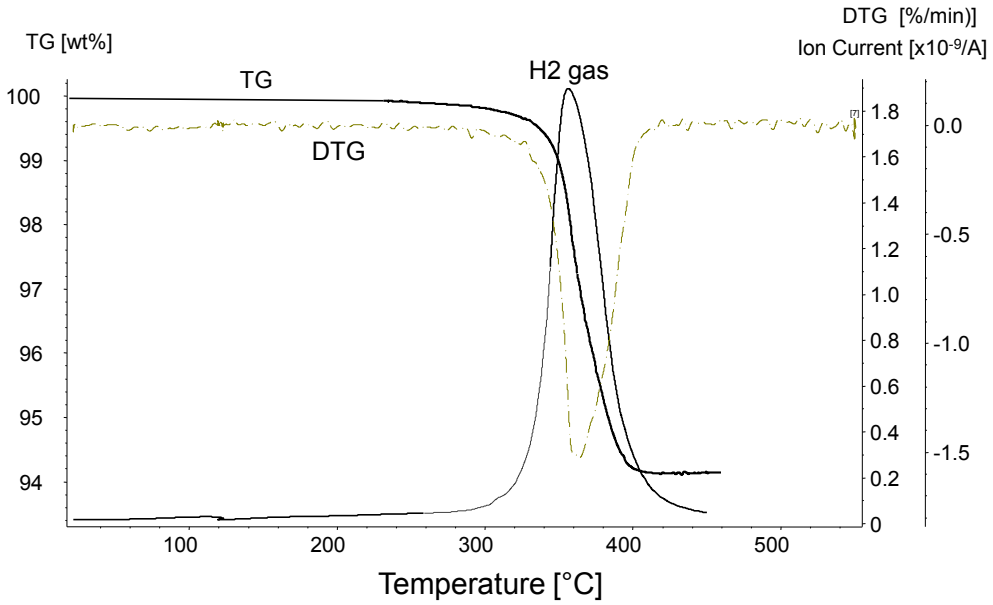

Figure 3.2: TGA 1 hour co-milled SWCNT-MgH_2 with mass 2 overlay and first order derivative of TG (DTG).

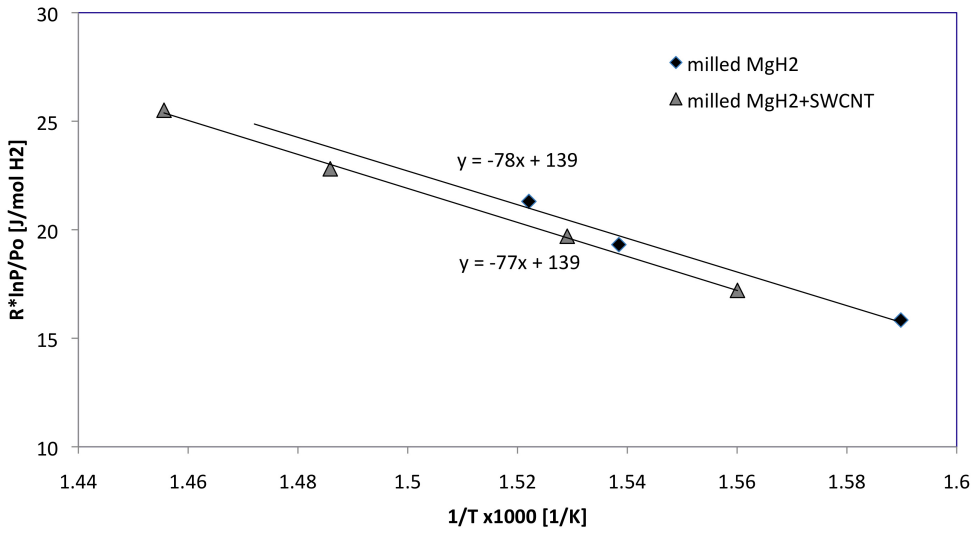

Figure 3.3: Van't Hoff plot for enthalpy of desorption comparing baseline MgH_2 and SWCNT-MgH_2 composites. The data was obtained from constant heating rate, variable pressure HP-DSC analysis.

for both the SWCNT-MgH_2 system and for the MgH_2 baseline. Optimum dispersion of the SWCNTs on the MgH_2 surfaces is achieved at 1 hour of co-milling, as evidenced by a sharp peak in the BET surface area. Co-milling for 1 hour also damages the SWCNTs, as evidenced by their Raman spectra [118]. The 1 hour co-milled process condition was the one used for the cycling experiments. At 7 hours of co-milling the SWCNTs are destroyed and the BET surface area decreases to the baseline level.

Figure 3.1B shows a TEM micrograph that illustrates the dispersion of the SWNCT's on the MgH_2 particle surfaces. The arrows in the micrograph point to the SWCNTs that are discernable in a two-dimensional projection of the TEM image. A metal nanoparticle attached to a nanotube (second arrow from the left) is also visible on the hydride surface. The SWCNTs along with the amorphous carbon and the metallic nanoparticles completely cover the hydride powder. Thus the system microstructure is that of a nanocomposite. As will be shown in the subsequent text and figures, the SWCNTs survive multiple hydrogenation/dehydrogenation cycles.

Figure 3.2 shows the gas evolution results of the SWCNT-MgH_2 nanocomposites after 1 hour of milling. The sample was heated to 120 °C at a rate of 10 °C/min, held at 120 °C for 20 minutes, heated to 550 °C at a rate of 10 °C/min, and then held at 550 °C for 30 minutes. Gas evolution was monitored by mass spectroscopy (MS). This experiment was repeated twice with nearly identical results. The peak rate of hydrogen desorption occurred at 360 °C. No hydrocarbon emission was detected at temperatures where hydrogen was evolved. The hydrogen loss in the composites was measured to be 5.7 wt.%. Figure 3.3 shows the HP-DSC results for both systems. As expected, co-milling MgH_2 with SWCNTs does not

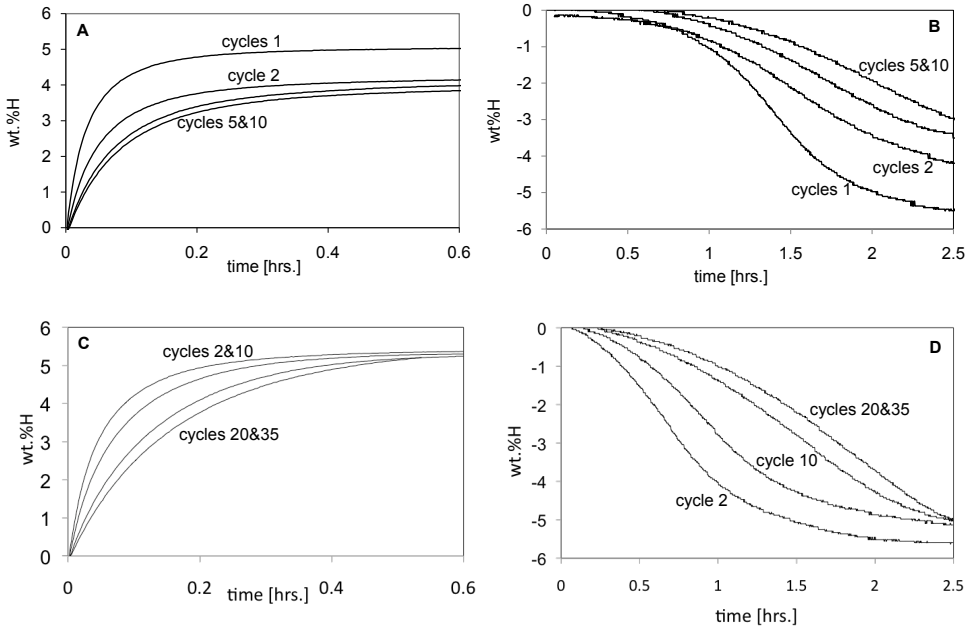

Figure 3.4: representative absorption and desorption cycling data for the baseline MgH_2 powder (A and B) and for the SWCNT-MgH_2 composites (C and D). The cycling experiments were performed at 300 °C. With increased cycling the kinetics degrade but at different rates for the two systems.

alter the enthalpy of magnesium hydride desorption. Thus we can state from the onset that the beneficial effects of the SWCNTs, which will be demonstrated in the subsequent figures, are related to kinetics and not to any changes in the system thermodynamics.

Figure 3.4 shows representative absorption and desorption cycling data for the baseline milled MgH_2 powder (A and B) and for the SWCNT-covered MgH_2 (C and D). The hydrogen sorption kinetics of both systems does degrade after prolonged cycling. However, the rate and the magnitude of the degradation are very different between the nanocomposite and the baseline. The baseline powder was desorption/absorption cycled 10 times. The nanocomposite powder was cycled up to 35 cycles using the same pressure conditions as the baseline. By cycle 10 the MgH_2 baseline is able to absorb(desorb) less than 4wt.% (3wt.%) hydrogen in 0.6 (2.5) hours. Conversely the nanocomposite powder still sorbs approximately 5 wt.% at the same time increments.

Figure 3.5 compares the times to absorb(desorb) 4wt.% hydrogen for the nanocomposite versus the baseline MgH_2. The nanocomposite was tested at two sets of pressure conditions. The SWCNT-MgH_2 samples that were tested for 35 cycles received the same sorption regiment as the baseline powder: 10 bar absorption and 0.1 bar desorption. These were the specimens whose microstructure was analyzed in detail. Later, a second set of experiments was performed where the SWCNT covered MgH_2 was cycled using more aggressive pressures: 11 bar absorption and 0.04 bar desorption. These samples were tested for 105

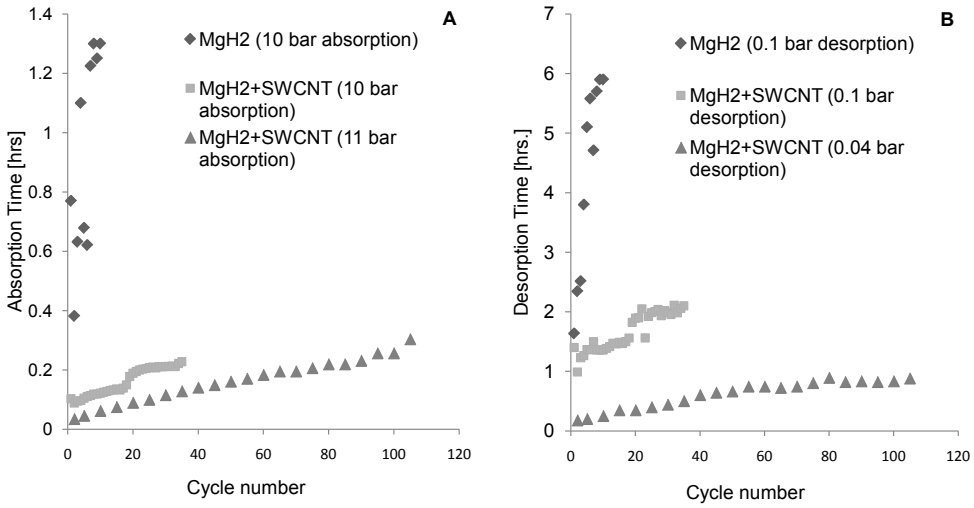

Figure 3.5: Absorption and desorption (4 wt.% hydrogen) cycling data for the baseline MgH_2 powder and for the SWCNT-MgH_2 composites. The cycling experiments were performed at 300°C. With increased cycling the kinetics degrade but at different rates for the two systems.

absorption/desorption cycles. However that microstructure was not analyzed.

Figure 3.5 shows that the kinetics of the baseline powder rapidly deteriorates during cycling. By cycle 10 the baseline takes approximately twice as long to absorb and four times as long to desorb as it did at the onset of testing. The SWCNT encapsulated powders not only sorb hydrogen at much higher rates but also maintain their stability for much longer times. For example, in the 35 cycled SWCNT-MgH_2 samples the time to absorb doubles after 35 cycles rather than after 10. Similarly in the SWCNT-MgH_2 powders the time to desorb only increases by a factor of two after 35 cycles. The SWCNT-MgH_2 samples tested at 11 bar absorption and 0.04 desorption showed much improved kinetics compared to the 10 bar absorption and 0.1 bar desorption specimens. This agrees with the known significant dependence of the hydrogen sorption rates on the deviation from equilibrium plateau pressure.

Figure 3.6 shows desorption activation energy plots obtained from the Kissinger analysis. The testing conditions include powders analyzed directly after milling as well as post sorption cycled specimens. The activation energy of as-milled MgH_2 is in the same range as previously reported [44] and is approximately 20 kJ/mol lower than that of identical but unmilled powder. Co-milling with the SWCNTs reduces the activation energy for desorption, implying a catalytic effect of the metal particle - nanotube combination. However the roughly 25 kJ/mol reduction in the activation energy is rather modest compared to previously reported fifty percent reduction in the presence of advanced metallic catalysts [68].

After 10 cycles the activation energies for desorption in baseline MgH_2 and in the nanocomposite are nearly identical. After prolonged cycling they all converge to the value

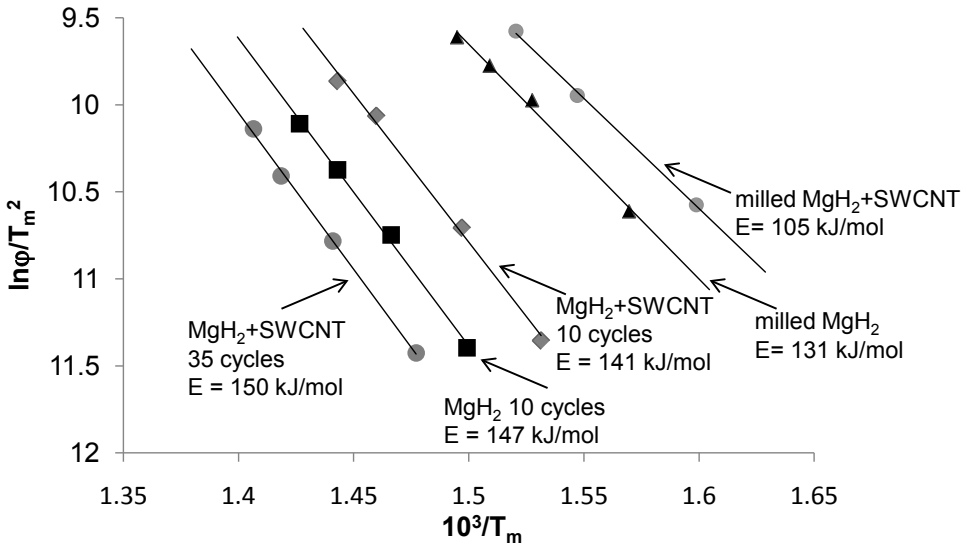

Figure 3.6: Activation energy of desorption obtained via Kissinger analysis. The powder history and activation energy are given on the graph.

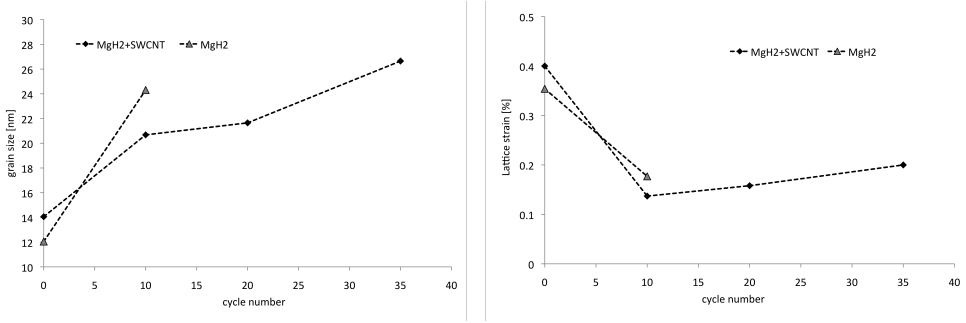

Figure 3.7: Grain size and lattice strain as a function of cycling.

for unmilled powder of roughly 150 kJ/mol [44]. This indicates a similarity in the desorption rate controlling steps despite a tremendous difference in the measured sorption times. The convergence of the activation energies also clearly indicates that any catalytic effect due to the metal nanoparticles is lost after prolonged sorption cycling.

Unfortunately we do not have sufficient information regarding the absorption activation energy to make a significant comparison of hydrogenation versus dehydrogenation behavior. However Figure 5 implies that starting at cycle 1 the nanocomposite microstructure does influence absorption more than desorption.

Figures 3.7 shows the grain size and lattice strain in the baseline and the nanocomposite materials as a function of cycle number. The data at zero cycles is for the as-milled powders prior to sorption testing. The grain size in both systems increases during cycling. Judging from the grain size values after 10 cycles the SWCNT encapsulated hydride coarsens slower

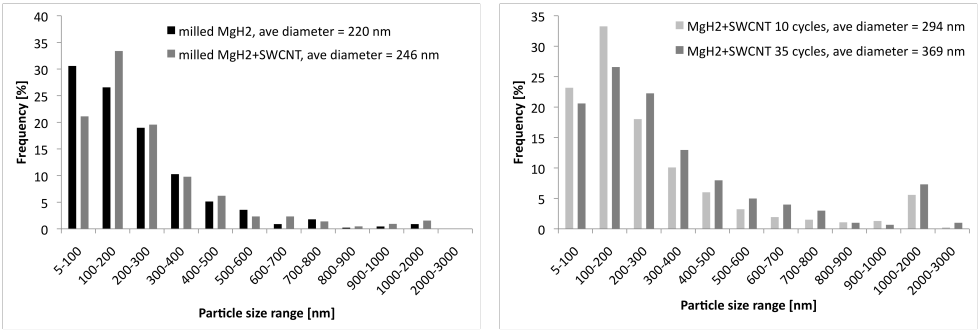

Figure 3.8: TEM-obtained particle size distributions for the as-milled powders and for the sorption cycled MgH_2-SWCNT composites. It is not possible to analyze the post-cycled baseline MgH_2 powder due to extensive sintering of the particles.

than the baseline. This is not unexpected since the kinetics of the SWCNT-MgH_2 system are faster, which in turn means that the composite spends less time at elevated temperature per sorption cycle. The two systems do not have significant differences in the lattice strain. This indicates that SWCNT coverage does not appreciably influence the strain in the hydride either during milling (cycle 0) or during subsequent sorption cycling.

Figure 3.8 shows histograms of the particle size distributions at various testing conditions. Approximately 500 particles were analyzed to generate each histogram. The size distributions were obtained directly from TEM analysis of the as-processed powders. The powders were not agglomerated and could be easily dispersed as a monolayer onto an amorphous carbon grid without incurring artifacts due to overlap. Figure 3.8A shows the particle size distributions for the as-milled baseline MgH_2 and for the as-milled SWCNT encapsulated MgH_2. The two batches have similar particle sizes and analogous size distributions. This confirms a previous claim [118] that any kinetic sorption enhancement obtained in the as-milled condition (not after cycling) is not due a particle size variation between the baseline and the co-milled powders.

It is not possible to obtain a size distribution for the baseline powders after cycling since the powders are very heavily agglomerated or sintered. Agglomeration is defined as a decrease in the total particle surface area without a net densification of the powder compact. Sintering is defined as a net densification of a powder compact with a corresponding decrease in the surface area. It is impossible to separate the two mechanisms without performing densification experiments of powder compacts coupled to surface area analysis. Conversely the SWCNT-covered MgH_2 did not agglomerate/sinter as drastically with the post-cycled particle size distributions were readily obtainable. This is shown in Figure 8B, after 10 and 35 cycles. The mean particle size did increase from 246 nm in the as-milled state to 294 nm after 10 cycles and 369 nm after 35 cycles. Figure 3.9A shows an SEM micrograph of a typical cluster of agglomerated/sintered powder particles in the MgH_2 baseline samples

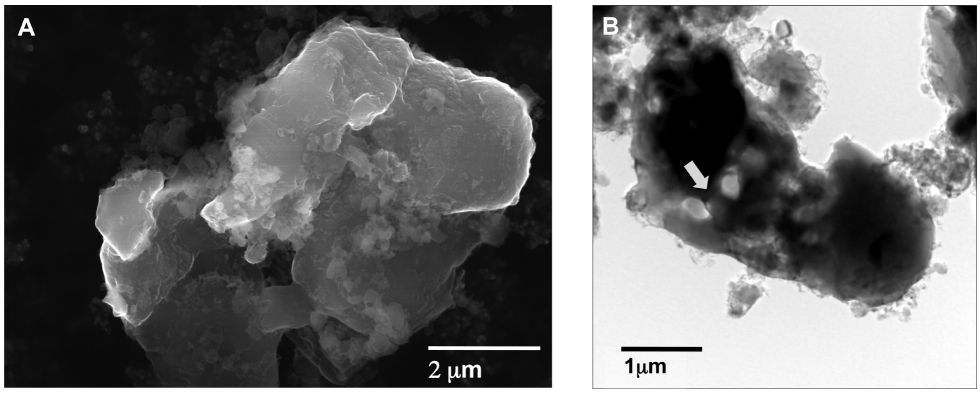

Figure 3.9: (A) Scanning electron micrograph of several agglomerated/sintered MgH_2 particles after 10 cycles. (B) Bright field TEM micrograph of several sintered MgH_2 particles representative of the size distribution found in the baseline MgH_2 after 10 cycles. Arrows point to the sintered interface between two previously separate particles.

after 10 cycles. The figure highlights the overall scale of the system after sorption cycling, which transforms from tens and one hundred nanometers to several micrometers. This dramatic size increase agrees with the established explanation regarding the reason for increased kinetic sluggishness of the metal hydride powders with prolonged high temperature sorption cycling. It is to avoid such a microstructurally coarse state that techniques like nano-encapsulation are being developed. Figure 9B shows a bright field TEM micrograph of several sintered hydride particles taken from the same batch. The micrograph shows an interface were it appears that two initially separate hydride particles have sintered/agglomerated together. The interface shows classic sintering/agglomeration behavior with the two particles forming a "neck" (arrowed) surrounded by porosity (lighter circular regions on each side). TEM analysis of other samples from the same batch confirmed that they too consisted of several initially smaller hydride particles that have sintered/agglomerated together. The sintering/agglomeration causes a loss in the total surface area for a given volume for the hydride(metal) and an increase in the diffusion distance for the hydrogen.

After 10 sorption cycles the hydride particles were too thick to allow for quantitative TEM analysis of bulk microstructural features. To perform quantitative characterization of the grains and defects found in cycled baseline powder it was necessary to mechanically break up the particles. This was achieved via manual mortar and pestle grinding followed by sonication. These de-agglomeration techniques were employed since they are known not to affect the bulk microstructure except for introducing a minor amount of additional strain. It is important to point out, however, that the particle sizes shown in Figures 10 and 11 are not representative of the post-cycled size distribution.

The *bulk* α-MgH_2 microstructure in the SWCNT covered hydride and the baseline powder was quite similar. The initial post-milled microstructures were characterized previously

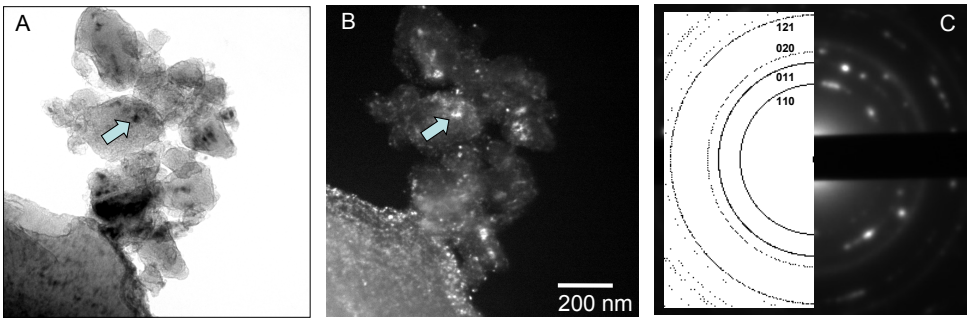

Figure 3.10: TEM micrographs highlighting the nanocrystalline microstructure of the baseline MgH_2 powder after 10 sorption cycles. A) Bright field micrograph of several differently oriented hydride particles. B) Dark field micrograph obtained using a portion of the 110 α-MgH_2 ring pattern highlighting numerous nanocrystalline grains. C) Corresponding selected area diffraction (SAD) pattern with a simulation insert. Arrows point to the same area in bright field and dark field micrographs.

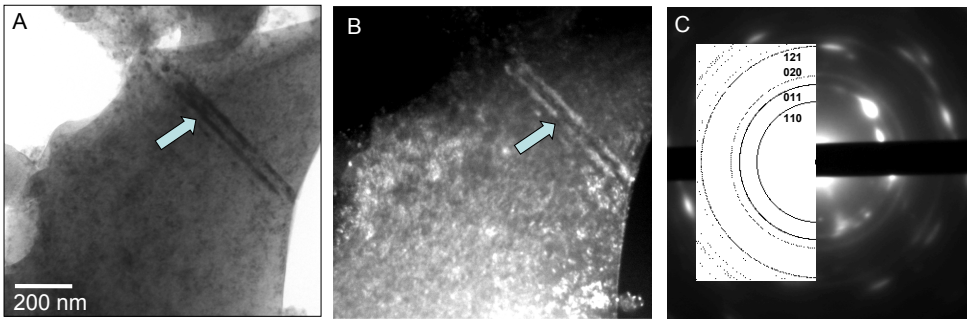

Figure 3.11: TEM micrographs highlighting the nanoscale twins (arrowed) present in the baseline MgH_2 powder after 10 sorption cycles. A) Bright field micrograph. B) Dark field micrograph obtained using a portion of the 011 α-MgH_2 ring pattern highlighting the twins. C) Corresponding selected area diffraction (SAD) pattern with a simulation insert.

[118]. The post-cycled microstructures are covered here. While the average grain size in the SWCNT covered powders was smaller than in the baseline, both systems are characterized by wide variations in the grain sizes from particle to particle. Some hydride particles consisted of one or several large α-MgH_2 crystallites. While the crystallites did occasionally contain defects such as twins or stacking faults, overall their number frequency was much lower than in the as-milled samples, implying that they were annealed out. Other hydride particles consisted of numerous truly nano-scale hydride grains. The selected area diffraction patterns (SAD's) reflected this difference, some being single zone axis spot patterns while others being discontinuous ring patterns.

Figure 3.10 highlights a large hydride grain in the post-cycled baseline sample that contains stacking faults (arrowed). Dark field micrograph shown in Figure 3.10B was obtained using the labeled 011 α-MgH_2 reflection. The corresponding SAD (not rotated) shows streaking. The grain shows non-uniform contrast presumably due to orientation variations. The crystallite is not in a symmetric zone axis and signal from adjacent grains very likely contributes to the SAD pattern as well. Additional variation in the contrast may arise from the surface oxide(hydroxide) which always forms on α-MgH_2 and contributes the thin continuous rings to the SAD.

Figure 3.11 highlights the other type of grain distribution commonly found in the powders. Figure 3.11 shows TEM micrographs of numerous truly nanocrystalline α-MgH_2 grains present in the baseline MgH_2 even after 10 cycles. Individual nanocrystalline grains showing strong Bragg contrast appear dark in the bright field image (Figure 3.11A). An arrow points to crystallites with such an orientation. Figure 3.11B shows numerous nano-scale α-MgH_2 grains, appearing bright, imaged using a portion of the 110 α-MgH_2 ring pattern. The pattern along with the simulation are displayed in Figure 3.11C. The size of the hydride crystallites varies quite significantly, though many particles are in the same 20 nm range as observed by XRD analysis. Figure 3.11 demonstrates that despite sorption cycling the microstructure does remain nanocrystalline. Rather it is the particle size that evolves the most.

Figure 3.12 shows a SWCNT covered hydride particle that is composed of relatively few (as evidenced by the SAD pattern) α-MgH_2 grains. This TEM specimen was of the nanocomposite that has received 20 sorption cycles. The two grains imaged in dark-field (Figure 3.12B) were obtained by using the two adjacent strong 110 type α-MgH_2 reflections. The stronger one, corresponding to the larger more intense crystallite on the left, is labeled in Figure 3.12C. The grains imaged in Figure 3.12B shows mottled (non-uniform, blocky) dark field contrast displayed in varying extent by all hydride grains. Such contrast was previously reported for highly deformed ionic minerals such as phyllosilicates [90, 91], though its origin (dislocations vs. beam damage) is still debatable.

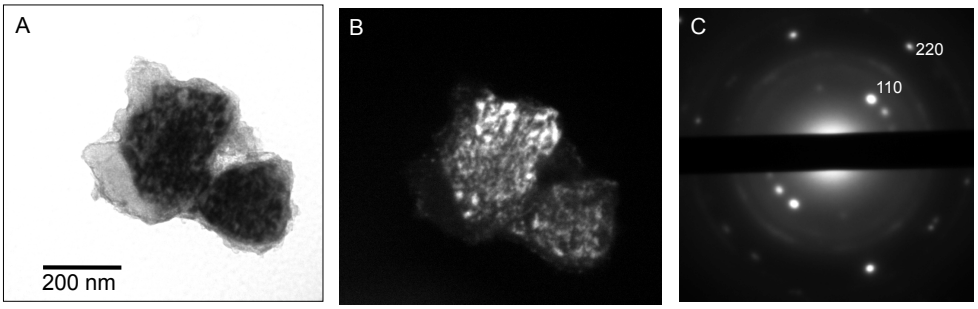

Figure 3.12: TEM micrographs highlighting a single larger a-MgH_2 crystallite in the SWCNT-MgH_2 composite after 20 sorption cycles. A) Bright field micrograph. B) Dark field micrograph obtained using a g =110 α-MgH_2 reflection. C) Corresponding selected area diffraction (SAD) pattern with a simulation insert.

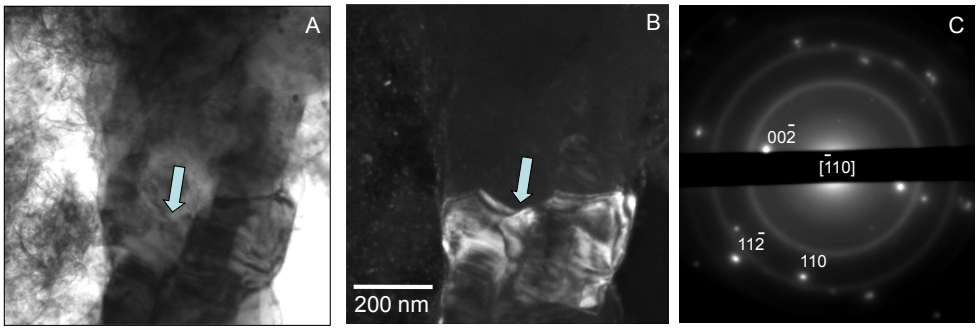

Figure 3.13: TEM micrographs highlighting unsorbed Mg particles in the MgH_2-SWCNT composite after 20 sorption cycles. A) Bright field micrograph. B) Dark field micrograph obtained using a g =200 Mg reflection. C) Corresponding selected area diffraction (SAD) pattern with a simulation insert.

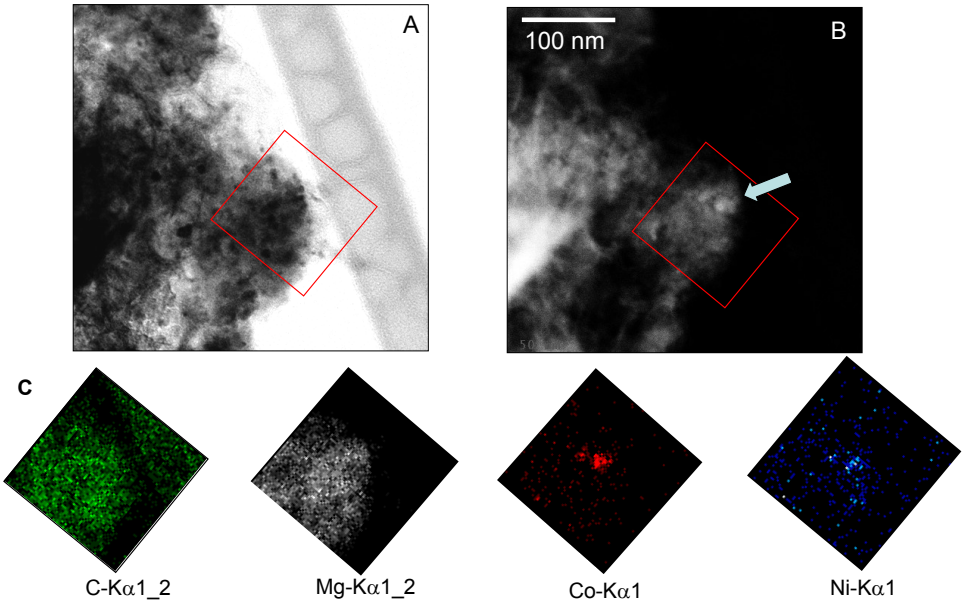

Figure 3.14: A and B) Z-contrast HAADF STEM micrographs of a metallic nanoparticle on the composite powder surface after 35 cycles. C) EDXS elemental maps of carbon, magnesium, cobalt, and nickel in the area marked by red square. The map demonstrates how the hydride particles remain encapsulated by carbon during the cycling.

Figure 3.13 shows an example of unsorbed metallic magnesium present in the SWCNT-covered powder. This sample was analyzed after the 20^{th} absorption cycle. With prolonged cycling the baseline MgH_2 powders displayed more metallic magnesium after absorption, agreeing with the volumetric results. Interestingly, we did not find any evidence of partially sorbed grains. Rather the situation seemed binary; particles were either fully hydrided or not at all. The metallic magnesium shows fundamentally different contrast compared to the hydride, and is readily distinguishable. The vertically aligned defect beginning directly below the arrow and strongly visible in dark field is either a grain boundary or a dislocation. The particular crystallite(s) imaged in Figure 3.13B is near the [-110] zone axis. The continuous rings visible in the SAD are not surprising and are from the oxide that always forms on the magnesium surface when exposed to even minuscule quantities of air or water vapor.

Figure 3.14 demonstrates how the carbon allotrope - metallic nanoparticle mixture still covers the hydride particles even after 35 cycles. Figure 3.14A shows a bright field STEM micrograph of the powder adjacent to a portion of the holey carbon grid holding the powder (holey carbon grids were used for analytical work, so as to eliminate the carbon background signal). Figure 3.14B shows the same area in Z-contrast High Angle Annular Dark Field (HAADF) mode. The region that is squared was analyzed using EDXS elemental mapping. The brighter region (arrowed) in Figure 3.14B is revealed in Figure 3.14C to be a Ni-Co nanoparticle. The elemental maps shown in Figure 3.14C highlight that the carbon coats

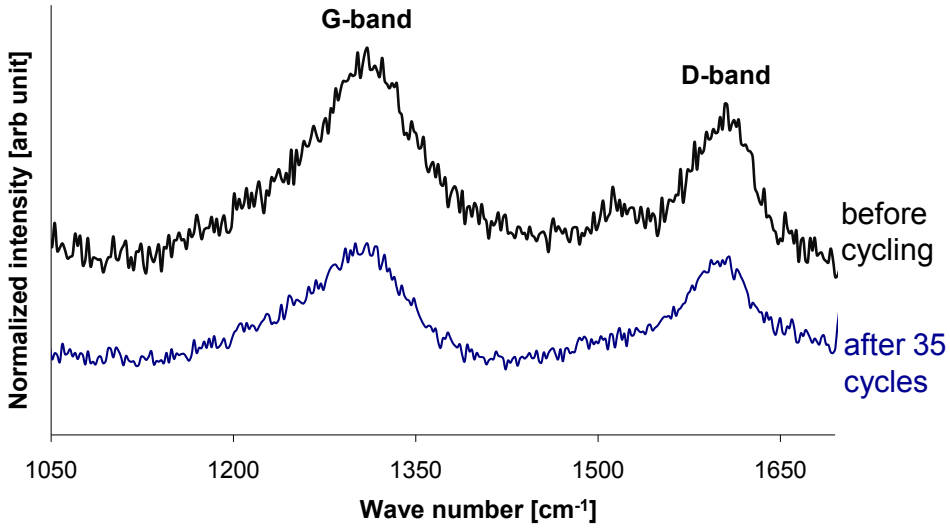

Figure 3.15: Raman spectra of the MgH_2+SWCNT composites before and after cycling, indicating that the SWCNTs have survived 35 absorption/desorption cycles.

the MgH_2 quite uniformly and completely. The dark region in the carbon map in between the hydride particle and the holey carbon grid indicates that the background carbon signal is negligible. Since EDXS provides no structural information, it is unclear whether the metallic particles are reacted with the magnesium to form alloys or intermetallics. Additional site-specific electron diffraction analysis would be necessary to answer that question. However it is known from the activation energy analysis (Figure 3.6) that all catalytic effects are lost after sorption cycling, implying that the particles did react.

Figure 3.15 shows the Raman spectra of the as-milled SWCNT covered hydride obtained directly after co-milling and after 35 sorption cycles. In the spectra the G-band is representative of the c-c graphite bonds and the D-band is representatives of the defects in the structure of carbon nanotubes. The spectra demonstrates that the defective (due to the ball milling) SWCNTs survive the sorption cycling without any additional noticeable degradation. Even after 35 cycles the SWCNTs still coat the hydride surface, preventing sintering and agglomeration.

3.4 Discussion

To summarize, the main and arguably only difference between the two samples' post-cycled bulk microstructures is the average grain size. We believe that this is due to the variation in the time spent at elevated temperature per sorption cycle for the nanocomposite versus the baseline MgH_2 powders. However these differences are not that large and cannot be responsible for the sorption kinetics variation. As was shown in the Results, sorption cycling

causes the activation energy of desorption in the nanocomposite and in the baseline MgH_2 to converge to a value of roughly 150 kJ/mol.

The MgH_2 to Mg phase transformation is still debatable. Several rate-limiting mechanisms have been proposed: 1) the high activation energy of hydrogen dissociation/reassociation on MgH_2 surface [100]. 2) the slowness of the Mg-MgH_2 phase boundary movement due to the slow diffusivity of the hydrogen ions primarily through the hydride but also perhaps through the metal [22, 93, 94, 95, 96]; 3) the diffusion of hydrogen along a metal-MgH_2 interface [97, 98]. In addition some have argued that surface passivation/poisoning due to adsorbed oxygen or sulfur - containing species may also be rate limiting [99]. Attempting to ascribe specific rate-limiting mechanisms that correspond to measured activation energies may not be that fruitful. A 150 kJ/mol activation energy for desorption may be attributed to any one of the above mechanisms. For example, it is well known that the activation energy for hydrogen recombination on pure α-MgH_2 surface is relatively high. The literature-quoted values include 144 kJ/mol and 172 kJ/mol (see reference [100] and the citations therein). Alternatively activation energy of 160 kJ/mol was recently reported to coincide to hydrogen diffusion through the α-MgH_2 phase being the rate-limiting step in desorption [23]. Moreover a recent modeling work also indicates that because of the interdependence of hydrogen diffusion and dissociation mechanisms a single rate-limiting step may not exist at all [123].

What does vary by orders of magnitude between the baseline and the SWCNT covered powder is the particle size. Without any additional catalytic enhancement, such a difference in the particle size will translate into a tremendous change in the time required to achieve a certain level of absorption/desorption. This is true both in terms of mechanism 1), i.e. the surface to volume ratio. It is also true in terms of mechanisms 2) and 3), i.e. the diffusion distances. Considering the latter, we can obtain a rough estimate of the effect of particle size on sorption times through the well-known shrinking core model [124, 125] . The model, which assumes a diffusion-controlled reaction, relates the fraction of material reacted f to the time t and the average particle radius of the reactant R. The difference in the rates of hydrogen diffusion through the metallic magnesium versus MgH_2 phases is incorporated the rate constant k, such that $k_{desorption} \neq k_{absorption}$. The most general form of the relationship is the following: $(1-f^{1/3}) = 1-kt^{1/2}/R$. This can be rearranged to provide an expression for the time to achieve a constant amount of sorption: $t = R^2(1-(1-f^{1/3}))^2/k^2$. The formula highlights the strong dependence of diffusion-controlled kinetics on the particle size and indicates why a secondary phase that coats the hydride and prevents particle sintering/agglomeration is so beneficial. For example a change in a particle diameter from 200 nm to 2 μm will result in two orders of magnitude increase in the time to react.

An implication of this work regards the possibility of stabilizing the nano-scale size of

a variety of hydrogen chemisorbing materials during elevated temperature sorption cycling. While numerous routes have been found to achieve initially nano-scale dimensions, very few routes - such as melt infusion into a porous matrix host - exist to preserve this structure at elevated temperatures after tens or hundreds of hydrogenation/dehydrogenation cycles. We have now shown that another, perhaps simpler route is available to achieve a similar result. High-energy milling is a well-established technique to reduce the particle size of powders or to achieve an intimate mixture of several phases. Workers who co-mill hydrides with carbon nanotubes recognized this method as a very good way to disperse the two phases but did not fully appreciate the implication for size stabilization. The SWCNT- amorphous carbon mixture is now shown to work, presumably due to the high structural and chemical stability and fine size of the nanotubes. However other carbon allotrope-catalyst combinations may be similarly effective and will be explored in future cycling studies.

3.5 Summary

In this study we detailed the hydrogen sorption cycling performance of SWCNT-magnesium hydride nanocomposites. A nanocomposite microstructure was achieved through high energy co-milling the hydride along with a mixture of SWCNTs, amorphous carbon and metallic nanoparticles. The nanocomposite and identically milled baseline MgH_2 (baseline) were volumetrically sorption cycled at 300 °C. The SWCNT covered MgH_2 displays a fundamentally different sorption cycling behavior compared to the baseline, though the activation energies for desorption are roughly identical. The kinetics of the baseline powder rapidly degrade, where by sorption cycle 10 it takes nearly 84 minutes to absorb 4 wt.% hydrogen and over 6 hours to desorb this quantity. Conversely the nanocomposites display a remarkable kinetic stability. At cycle 10 the time to absorb 4 wt.% hydrogen is 7 minutes, while the time to desorb is 80 minutes. Even at cycle 35 the time to absorb is only 14 minutes, while the time to desorb is right at 2 hours. A more aggressive (in terms of variation of the sorption pressure from the plateau pressure) sorption regime allowed SWCNT covered MgH_2 to be tested up to 105 absorption desorption cycles with only minor kinetic degradation.

TEM analysis confirms that nanocomposite microstructure stabilizes the MgH_2 particle size during cycling. At the onset of cycling the mean diameters of the SWCNT covered hydride and of the baseline are 246 and 220 nm, respectively. After 10 cycles the baseline MgH_2 powders sinter/agglomerate, becoming microns in scale. However the mean diameter of the SWCNT covered particles increases to only 294 nm after 10 cycles, and to 369 nm after 35 cycles. TEM analysis and Raman spectroscopy confirm that even after 35 cycles the hydride remains covered by the SWCNTs and the amorphous carbon.

4

Synergy of Elemental Fe and Ti Promoting Low Temperature Hydrogen Sorption Cycling of Magnesium

Material in this chapter has been submitted to: *Int J Hydrogen Energy*
List of authors: Shalchi Amirkhiz B, Zahiri B, Kalisvaart WP, and Mitlin D; Date submitted: 9 December 2010; Manuscript reference No.: HE-D-10-02943

4.1 Introduction

Magnesium hydride stores a large amount of hydrogen (7.6 wt.%) reversibly, but suffers from very slow kinetics and high thermodynamic stability (-77 kJ/mol H_2), both necessitating high temperatures around 300 °C for desorption. Many attempts have been made to alter the thermodynamics of magnesium hydride by incorporating alloying elements such as Ni, Cu, Al and Si [35, 36, 39, 126], but no viable way to produce large quantities of destabilized material has been found. As a consequence, most research efforts have been directed at improving the sorption kinetics of magnesium hydride.

Transition metals in particular have been intensively studied theoretically and experimentally as suitable catalysts for sorption of magnesium (hydride) [67, 68, 69, 70, 74, 127, 128, 129, 130]. It has been shown that co-milling 3d-metal catalysts with MgH_2 may result in lower activation energies and faster sorption kinetics; however the thermodynamics remains unchanged [67, 68, 69, 70].

Fe has been proposed as a strong catalyst towards hydrogen sorption of magnesium [40, 41, 68, 70, 71]. It is visually shown, with the aid of SEM, that the kinetics of MgH_2 desorption changes drastically in the presence of Fe catalyst particles; the nucleation of Mg phase occurs in the interface of MgH_2 and Fe [28]. Also, in Mg-Fe systems prolonged cycling

at temperatures of higher than 300 °C eventually resulted in formation of Mg_2FeH_6 [72].

Intermetallic compounds of transition metals are also considered as catalysts or destabilizing materials for magnesium (hydride). Efforts have been made to destabilize magnesium hydride by using intermetallic compounds with low heat of hydride formation; however, no significant change in the thermodynamics was achieved for these composites [40, 41, 42, 43]. The FeTi intermetallic compound has also been investigated as a catalyst towards hydrogen sorption of magnesium [40, 41, 42, 43, 74, 75, 131]. FeTi directly reacts with hydrogen to form FeTiH∼1 at room temperature and 10 atm hydrogen equilibrium pressure and form FeTiH∼2 at higher but not well defined plateau pressure [77, 78]. Nanocrystalline FeTi, can readily absorb hydrogen with no activation required [78].

A ternary magnesium based composite prepared by co-sputtering of magnesium, titanium and iron has exceptionally good cycling performance in terms of both the kinetics and stability against degradation compared to the baseline binary systems. These improvements are attributed to possible formation of a nano-crystalline/ amorphous FeTi phase or synergistic catalytic effect of titanium and iron [74, 132]. Most research efforts have been directed at improving the kinetics by mixing MgH_2 with different catalysts using high-energy ball-milling to achieve uniform dispersion of the catalyst. Also, it is known that milling has intrinsic effects on the activation energy for desorption and can reduce its value by up to 50% in the first desorption cycle through formation of deformation twins. However, annealing treatment and prolonged absorption/desorption cycling eliminates these defects and increases the activation energy back to 150 kJ/mol [66]. Therefore, it is important to check the activation energies both in the as-milled and cycled state, as the catalysts effectiveness may be reduced or even completely lost during extensive cycling [118].

The present work reports on the hydrogen cycling behavior of ball-milled MgH_2-Ti, MgH_2-Fe, MgH_2-Fe-Ti and MgH_2-FeTi mixtures. We characterize the dispersion of the catalyst before and after cycling to have a better understanding of the catalytic activity of each additive using elemental mapping of scanning transmission electron micrographs. The as-milled and as-cycled microstructure was characterized using X-ray diffraction. We incorporated differential scanning calorimetry (DSC) and Sievert's techniques to assess the desorption activation energies in both as-milled and cycled states, and sorption cycling kinetics. We employ JMA kinetics model to track the kinetics and rate limiting mechanisms as a function of cycling for these composites.

4.2 Experimental Techniques

Magnesium hydride (MgH_2) powder was 98% pure hydrogen storage grade purchased from ABCR GmbH & Co. KG, the balance being magnesium. Titanium powder was 99.7% pure, $< 150\mu$m average particle size purchased from Sigma-Aldrich®. Iron powder was

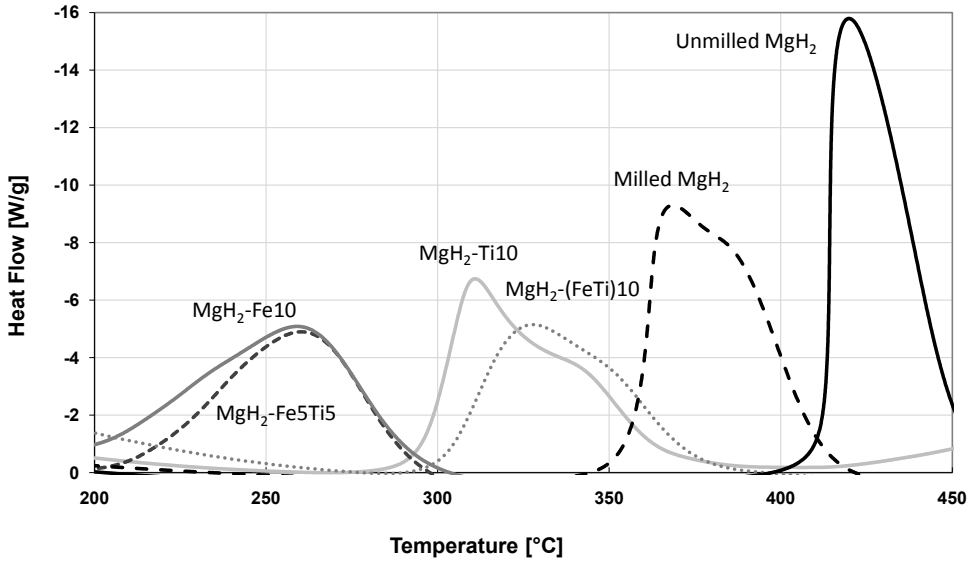

Figure 4.1: DSC curves showing the effect of different additives on desorption peak temperature of magnesium hydride.

99% pure, $< 212\mu$m average particle size purchased from Sigma-Aldrich®. FeTi intermetallic compound powder was high purity with $<150\mu$m average particle size purchased from Goodfellow®.

We made two kinds of ternary composites by combining the hydride powders with 5 at. % Fe - 5 at. % Ti and 10 at. % FeTi and we also made two binary composites of MgH_2 with 10 at. % Fe and 10 at. % Ti serving as the baseline. To achieve a reasonable dispersion of FeTi compound on MgH_2 particles we added 2.5 wt % multi-walled carbon nanotubes (MWCNTs) at the beginning of the milling experiment. Equal amounts of FeTi and MgH_2 powders were ball milled for 5 hours and subsequently MWCNTs and more MgH_2 were added up to make the composition MgH_2-10 at. % (FeTi)-2.5 wt % CNTs. For the sake of brevity we use the following nomenclature for these composites throughout the manuscript: MgH_2-5 at. % Fe-5 at. % Ti as MgH_2-Fe5Ti5, MgH_2-10 at. % (FeTi)-2.5 wt % CNTs as MgH_2-(FeTi)10, MgH_2-10 at. % Fe as MgH_2-Fe10 and MgH_2-10 at. % Ti as MgH_2-Ti10. Except for MgH_2-(FeTi)10, all the mixtures were milled for 10 hours in a Fritsch Pulverisette 6 planetary monomill. We used a 10:1 ball to powder weight ratio, with agate balls and vial at 600 rpm rotation speed for all the composites. Milling and all sample handling were performed inside a high-purity argon filled glovebox with the amount of oxygen and water vapor present being less than 0.1 ppm.

A small sample of about 10 mg from each composite was transferred to a calorimeter right after milling with minimum exposure to air. We used a combined differential scanning calorimeter (DSC) and thermogravimetric analyzer (TGA) (SDTQ600, TA Instruments)

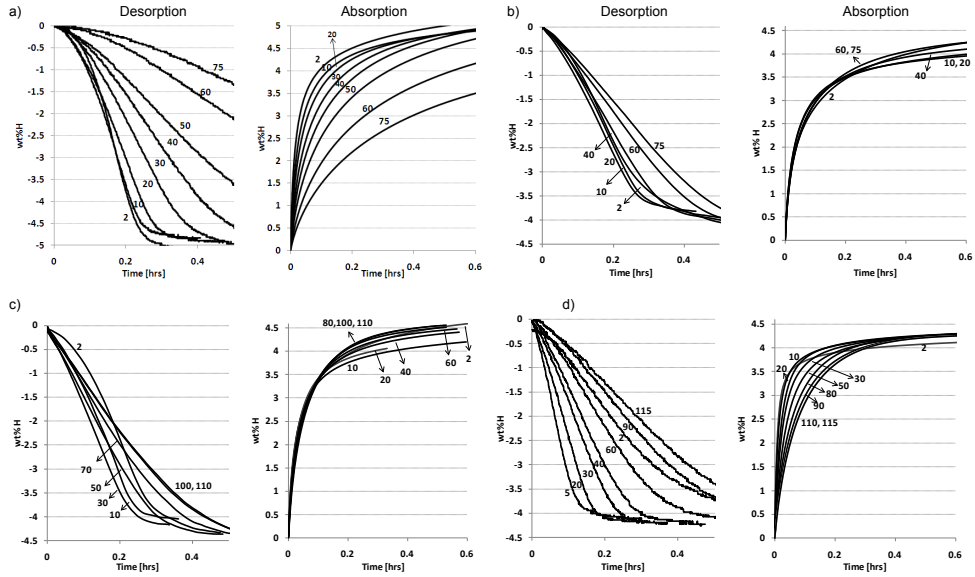

Figure 4.2: (a) Sievert's absorption and desorption cycles of MgH_2-Ti10 sample. First cycles are the fastest. (b) Sievert's absorption and desorption cycles of MgH_2-Fe10 sample. On absorption the kinetics improves through cycling whereas on desorption it accelerates first and slowly degrades after 30 cycles. (c) Sievert's absorption and desorption cycles of MgH_2-Fe5Ti5 sample. On absorption the kinetics improves through cycling whereas on desorption it accelerates first and slowly degrades after 30 cycles. (d) Sievert's absorption and desorption cycles of MgH_2-(FeTi)10 sample. On desorption the kinetics improves through first 10 cycles (activation). On absorption the performance degrades from the start through the end of cycling.

to determine the hydrogen desorption kinetics and activation energy measurements. The analysis was performed under a constant flow of high-purity (99.998% pure) argon to prevent oxidation.

Volumetric absorption and desorption measurements and also PCT measurements were performed using a Sievert's hydrogen sorption analysis system (Hy-Energy LLC. PCTPro 2000). All of the cycling measurements were carried out at 250 °C. The composite powders were analyzed aiming 100+ cycles and stopped earlier when degradation was apparent. Absorption started at a pressure of 2.5 bar (finishing at around 1 bar) and desorption at a starting pressure near 10 mbar (finishing at 20 mbar).

Transmission electron microscopy (TEM) was performed using the JEOL 2200FS microscopes, operating at 200 kV accelerating voltage. Scanning transmission electron microscopy (STEM) with a probe of a diameter of 1 nm was used. We used a high-angle annular detector to form high angle annular dark field (HAADF) images where the contrast is directly related to the atomic number Z. This technique coupled with energy-dispersive X-ray spectroscopy (EDS) with the capability of forming elemental maps was used to study the distribution of the catalyst material on magnesium (hydride) matrix. TEM samples were prepared by dry dispersing the powders onto amorphous holey carbon grids. We characterized samples at

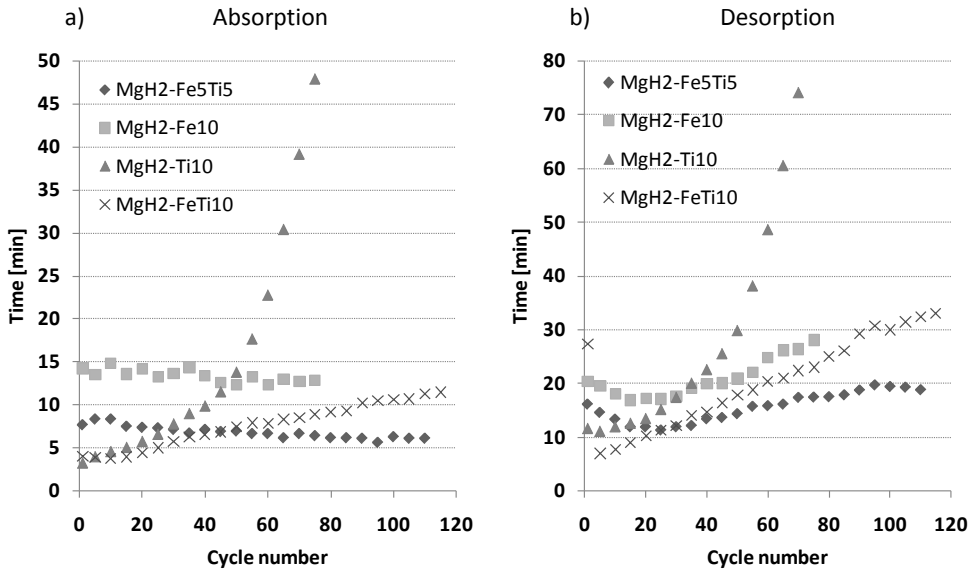

Figure 4.3: Time to reach 3.6 wt % capacity for the studies samples. Max Capacities of the composites are as follows: 5.3 wt % for MgH_2-Ti10, 4.5 wt % for MgH_2-Fe5Ti5, 4.5 wt % for MgH_2-Fe10 and 4.25 wt % for MgH_2-(FeTi)10

both as-milled and post cycled conditions. On post cycled samples, since it was not possible to do BET measurement, because of the small sample size, we performed image analysis using STEM bright field images. In order to have a proper statistical sample we measured the size of at least 200 particles from each composite.

4.2.1 Kinetics Measurements

Kissinger analysis [17] was employed to measure the activation energy of desorption. The method developed by Kissinger allows for obtaining the activation energy of a chemical reaction of any order by considering the variation of the temperature at the maximum reaction rate. In the case of endothermic hydride to metal transformation, the maximum reaction rate is straightforward to obtain from the constant heating rate DSC data and corresponds to the minimum of the desorption DSC peak. The Kissinger analysis can be expressed in the following form:

$$\ln \frac{\phi}{T_f^2} = \ln \frac{Rk_o}{E} - \frac{E}{RT_f} \tag{4.1}$$

where ϕ is the heating rate, T_f is the absolute temperature at the maximum reaction rate, E is the activation energy, k_o is the pre-exponential term for the rate constant $k = k_o \exp(-E/RT)$ and R is the gas constant. The activation energy is obtained from a linear plot of $\ln(\phi/T_f^2)$ versus $1/T_f$. For this analysis, the heating rates used were 5, 10, 20, and 25 °C min^{-1}.

To analyze the surface area of the composites and compare them to that of as-milled MgH_2 samples, a Quantachrome Autosorb 1 MP automatic gas adsorption system was used. The system is dedicated to standard measurements of nanostructured materials by nitrogen sorption isotherms at 77 K. Multipoint BET surface area measurement was done using AS1Win, version 1.5, software which supports the BET data reduction algorithm. All of the samples were degassed at 150 °C under a vacuum for at least 5 h prior to the tests.

A large number of kinetic models have been derived to explain solid-state phase transformations in metal-hydride systems. For MgH_2 the kinetic rate limiting step is typically either the dissociation/ recombination (chemisorption) transition between hydrogen gas and hydrogen atoms on the material surface [21, 22] or the nucleation and growth (NG) of the hydride during absorption or the metal phase during desorption [21, 23]. When hydriding involves a phase transformation from α to β, nucleation and growth is usually the dominant kinetic process [133]. Mintz and Zeiri have reviewed the most important NG models for hydrogen storage [25]; the two most applicable functional forms are the contracting volume (CV) models and the model developed by Avrami [26], based on the works of Kolmogorov, Johnson and Mehl [27]. The latter is typically referred to as the JMA or KJMA. The equation for the CV model is given by

$$f = 1 - (1 - kt)^{\eta} \tag{4.2}$$

where f is the fraction of the material undergone the $\alpha \rightarrow \beta$ transformation, k is the rate constant, η is a constant related to the dimensionality of the growth process; with $\eta = 3$ for three-dimensional and $\eta = 2$ for two dimensional growth, and t is time. For this model the assumption is that the initial nucleation on the surface is fast compared to the overall kinetics of growth and the surface nucleation layer is thin compared to the particle diameter [22, 28].

JMA analysis assumes random and constant nucleation rate or constant nuclei number, infinite sample volume and hard impingement between nuclei of the new phase [29]. The central equation of this model is given by

$$f = 1 - \exp(-(kt)^{\eta}) \tag{4.3}$$

where f is the fraction of the material undergone the $\alpha \rightarrow \beta$ transformation, k is the rate constant, η is a constant related to the dimensionality of the growth process, referred to as the Avrami exponent and t is time. For a constant number of nuclei, the value of η is typically interpreted as $\eta = \frac{d}{m}$ for constant nuclei number and as $\eta = \frac{d}{m} + 1$ for constant nucleation rate, where d is the growth dimensionality and $m = 1$ for interface-controlled and $m = 2$ for diffusion-controlled growth [30, 133]. For example, assuming a constant number of nuclei, $\eta = 3$ represents three dimensional - interface controlled growth and

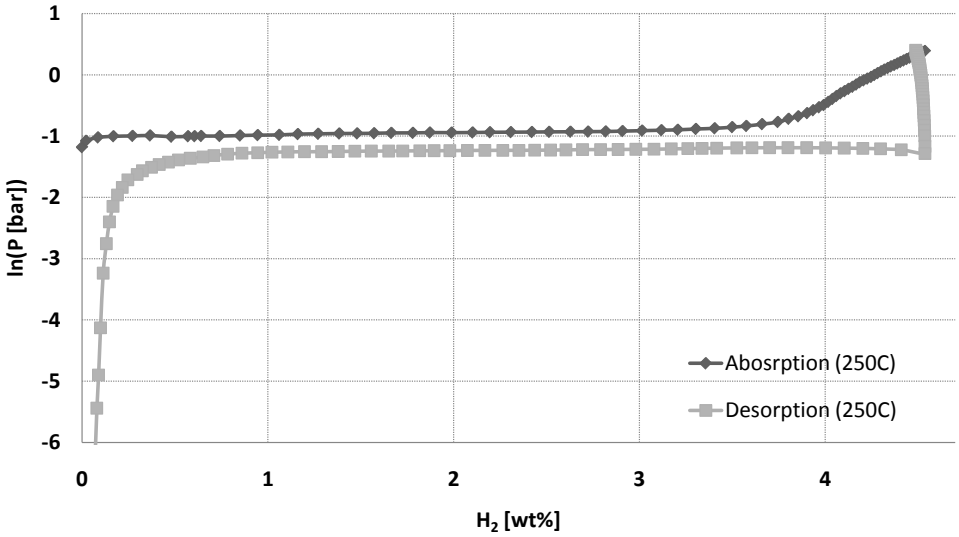

Figure 4.4: Pressure composition isotherms for MgH_2-Fe5Ti5 at 250 °C showing no thermodynamic change from that of pure magnesium / hydrogen system. The very similar graph was acquired for MgH_2-(FeTi)10 as well.

Table 4.1: BET- surface area of different composites after milling.

Sample	MgH_2 as is	MgH_2 Milled 10 hrs	MgH_2-Fe10	MgH_2-Ti10	MgH_2-(FeTi)10	MgH_2-Fe5Ti5
BET Surface Area $[m^2/g]$	2	12	20	16	16	40

$\eta = 1.5$ correlates with three dimensional - diffusion controlled growth, etc. [133]. Here the assumptions are that the initial size of a nucleus is small compared to that of the particle, the nucleation and growth of the new phase begins randomly in the bulk and at the surface, and there is sufficient and constant number of nuclei of the new phase within each particle.

Since activation usually takes place in the first few cycles we fit the Avrami equation to the first 5 cycles and consequently to cycles 10, 20 etc. Rate constant (k) values were plotted against cycle number to illustrate the general sorption kinetics through cycling. Also, Avrami exponent (η) was derived and corresponding rate controlling mechanisms were assessed.

4.3 Results

Figure 4.1 shows desorption properties of the as-milled composites. Adding Fe can drastically reduce the desorption peak temperature of magnesium hydride from around 420 °C to 255

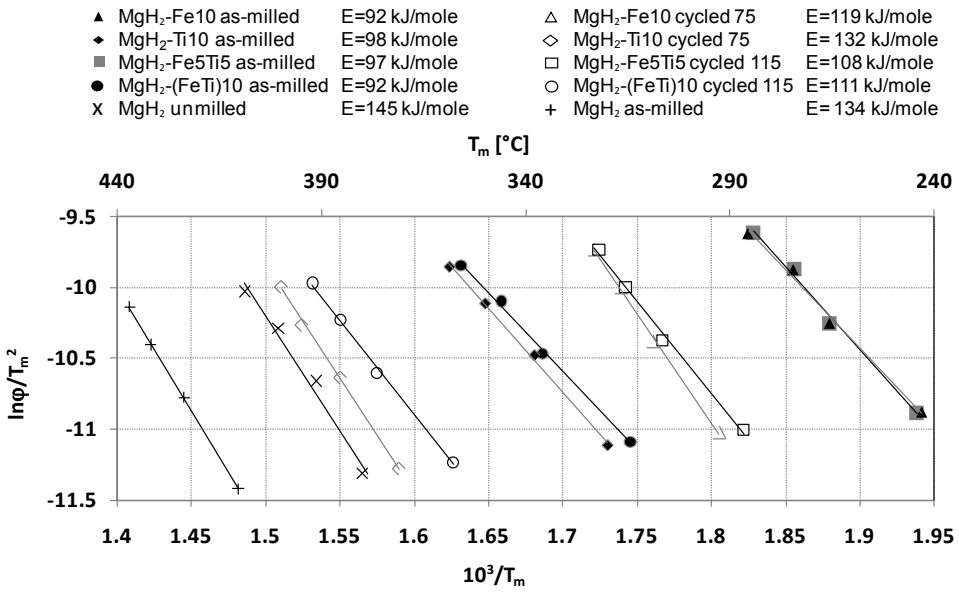

Figure 4.5: Activation energies before and after cycling measured using Kissinger analysis.

°C, where desorption starts below 200 °C. Adding Ti to MgH_2 reduced this temperature to 320 °C. Addition of (FeTi) resulted in a desorption peak temperature of 325 °C. For MgH_2-Fe5Ti5 this temperature is at around 255 °C, similar to the sample with Fe additive. It seems that the catalytic activity of Ti is obscured by that of Fe.

Figure 4.2 shows the result of sorption cycling of the studied composites. The results of desorption and absorption are shown in two separate graphs. These results are comparatively summarized in Figure 4.3 in the form of time-to-reach-3.6 wt % as a function of cycle number. The MgH_2-Fe5Ti5 composite has the best cycling performance in terms of both the kinetics and stability. The MgH_2-(FeTi)10 sample has quite fast kinetics at the start but deteriorates quite rapidly and eventually has sluggish kinetics.

Figure 4.4 shows the result of PCT measurement of the MgH_2-Fe5Ti5 sample at 250 °C. The equilibrium pressures, 370 mbar for absorbtion and 300 mbar for desorption, are similar to that of pure magnesium (ΔH= -77 kJ/mol H_2) which means that adding Fe and Ti has no effect on the thermodynamics of hydrogen sorption of the composite. Very similar results were achieved for MgH_2-(FeTi)10 sample (not shown here).

To further elucidate the catalytic activity of the additives we performed Kissinger analysis to measure the activation energies for desorption of hydrogen and the results are shown in Figure 4.5. The tests were done on as-milled composites as well as post cycled samples. Before cycling, the activation energies of desorption for these samples are almost identical; whereas after cycling, as the composite with Fe deteriorates faster the activation energy becomes larger in fewer number of cycles. For the composite with 10 at. % Ti, the measured

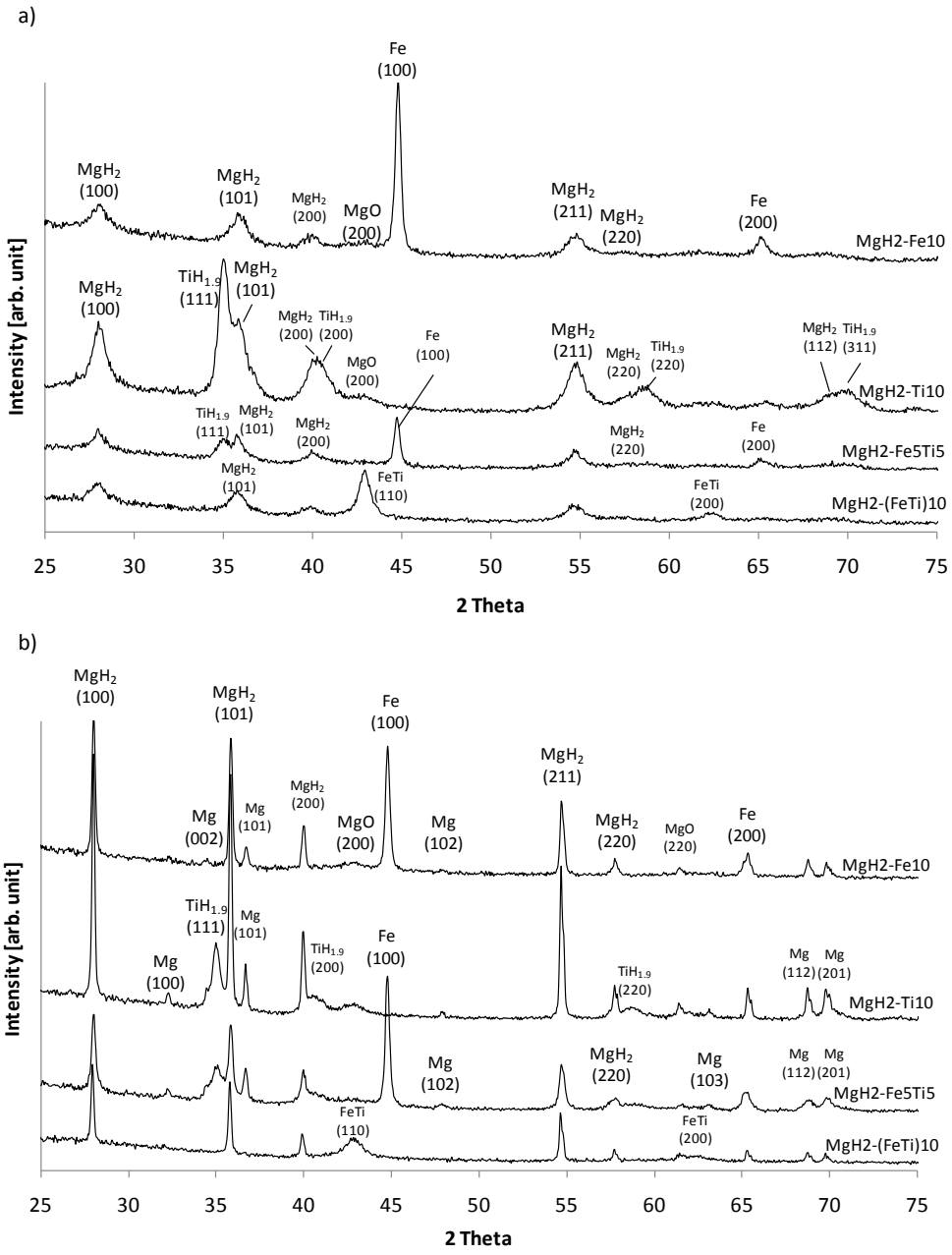

Figure 4.6: (a) X-ray diffraction patterns of the as-milled composites. (b) X-ray diffraction patterns of the as-cycled composites.

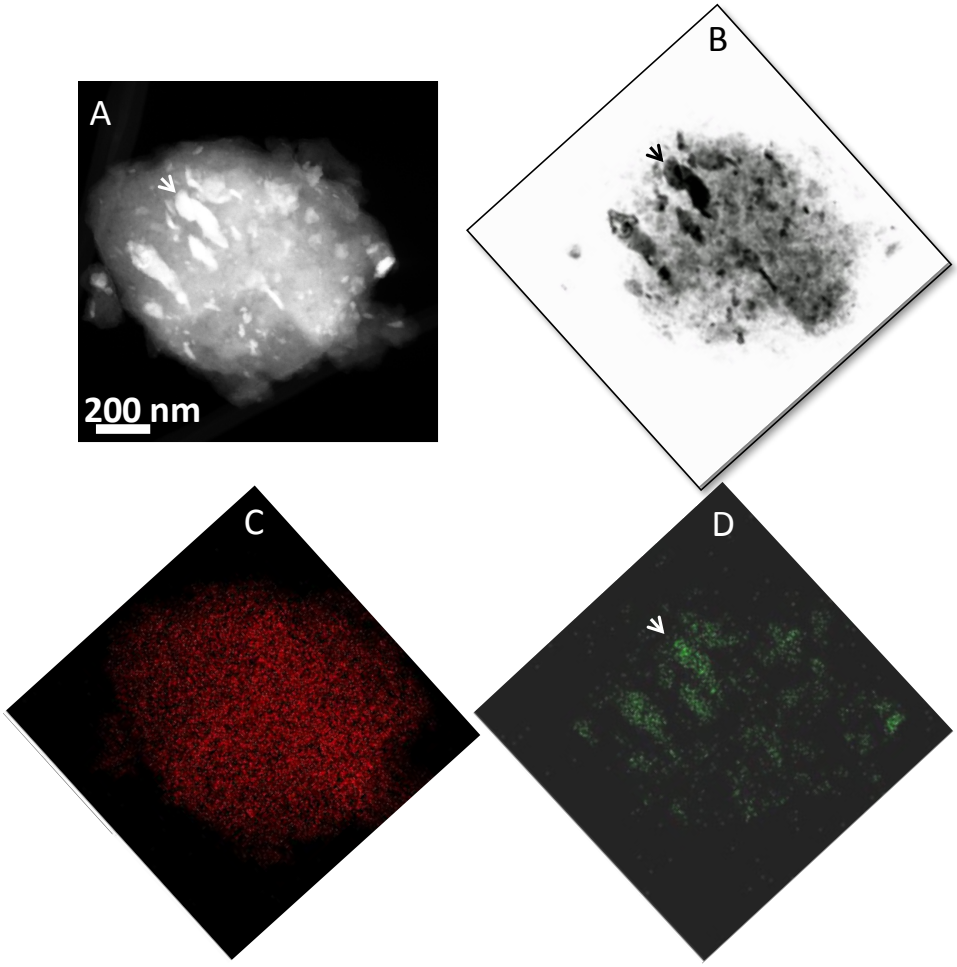

Figure 4.7: STEM - HAADF image (A) and STEM - bright field (BF) image of the mapped area (B) along with EDS elemental maps of Mg (C) and Fe (D) from a particle of MgH_2-Fe10 composite before cycling, showing uniform dispersion of Fe particles on Mg surface in nano scale.

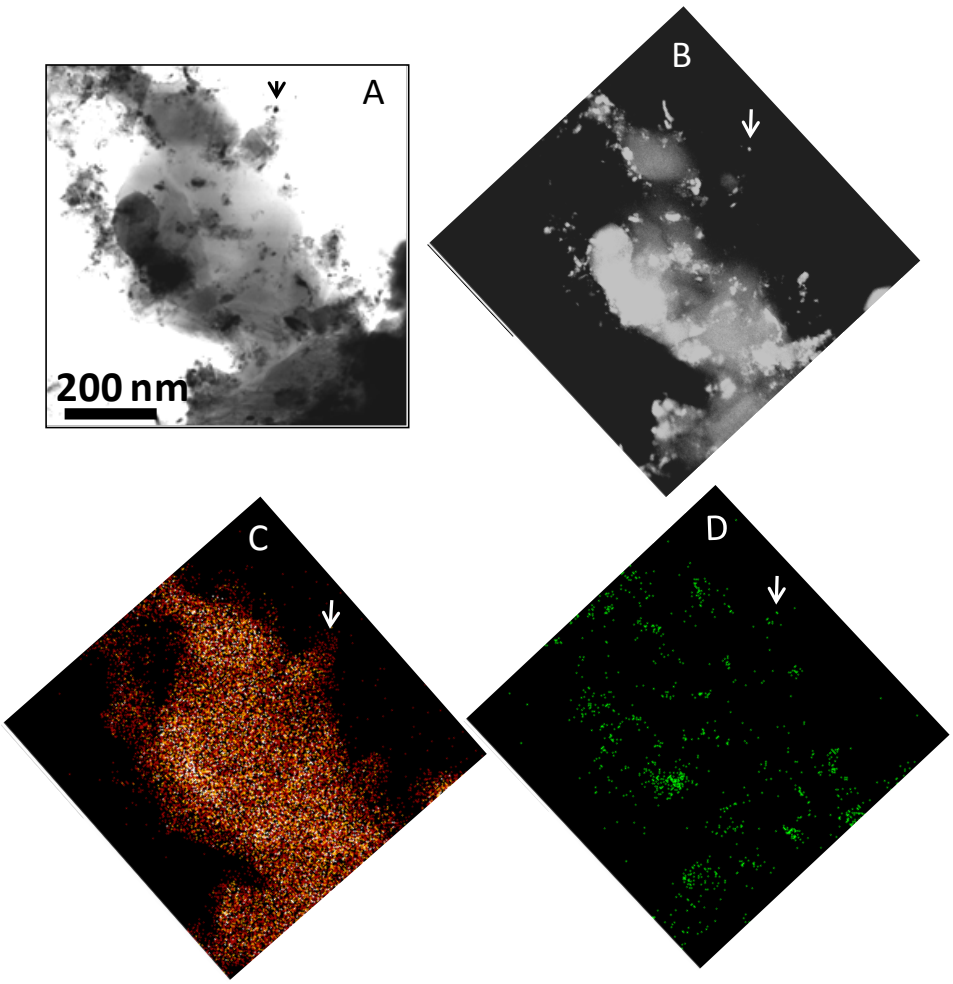

Figure 4.8: STEM BF (A) and HAADF image of the mapped area (B) along with EDS elemental maps of Mg (C) and Fe (D) from a particle of MgH_2-Fe10 composite after 75 cycles showing uniform dispersion of Fe particles on Mg surface.

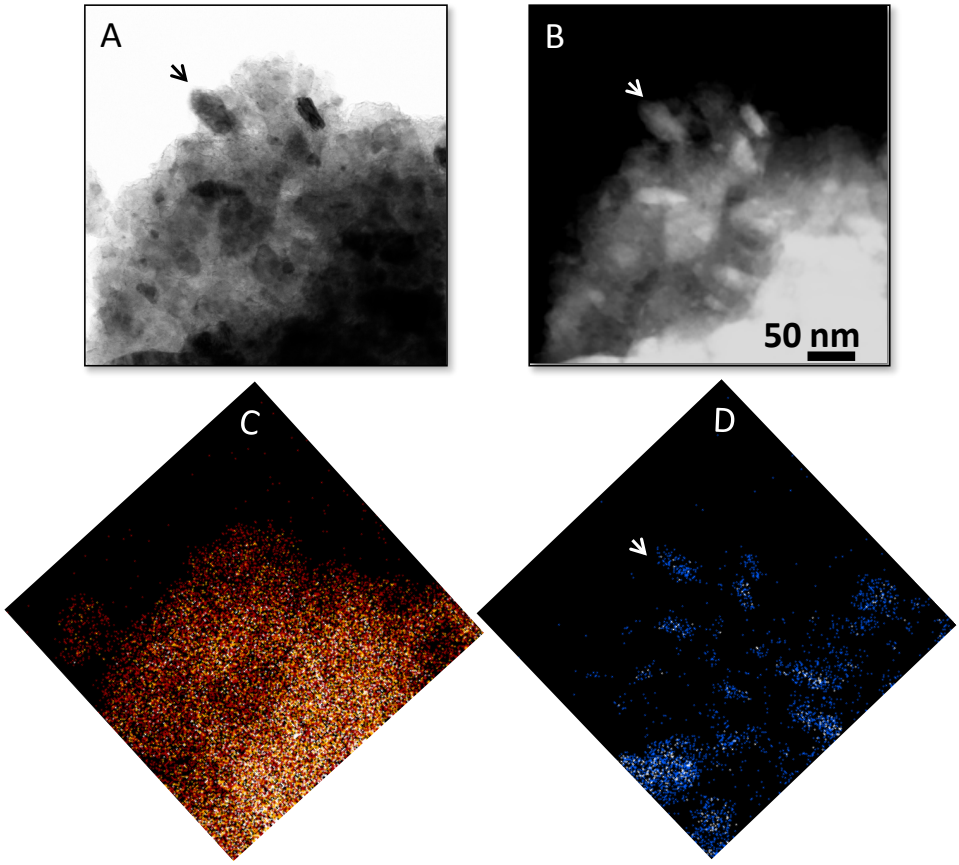

Figure 4.9: STEM - BF image (A) and STEM - HAADF image (B) along with EDS elemental maps of Mg (C) and Ti (D) from a particle of MgH_2-Ti10 composite before cycling showing uniform dispersion of Ti particles on Mg surface.

activation energy after cycling (132 kJ/mole) is identical to that of none-catalyzed MgH_2 as-milled powder (134 kJ/mole). The measured activation energy of desorption for MgH_2-(FeTi)10 sample after cycling is also very close to that of MgH_2-Fe5Ti5. It should be noted that although the activation energies after cycling are very close, the desorption peak temperatures (which are used to measure the activation energies) are different.

After cycling experiments the samples went through X-ray diffraction tests again and the results are shown in Figure 4.6. In Figure 6a, X-ray diffraction patterns of the as milled MgH_2-Fe5Ti5, MgH_2-(FeTi)10, MgH_2-Fe10 and MgH_2-Ti10 composites are shown. A prominent feature of the composites containing Ti is formation of $TiH_{1.92}$. General peak broadening due to the introduction of defects and grain size reduction is apparent. For MgH_2-Ti10 sample, a peak of $TiH_{1.92}$ represents titanium hydride formation during ball milling. The X-ray diffraction patterns of these composites after cycling are shown in Figure 6b. The peaks are sharpened due to prolonged exposure to elevated temperatures during cycling. No intermetallic formation is observed.

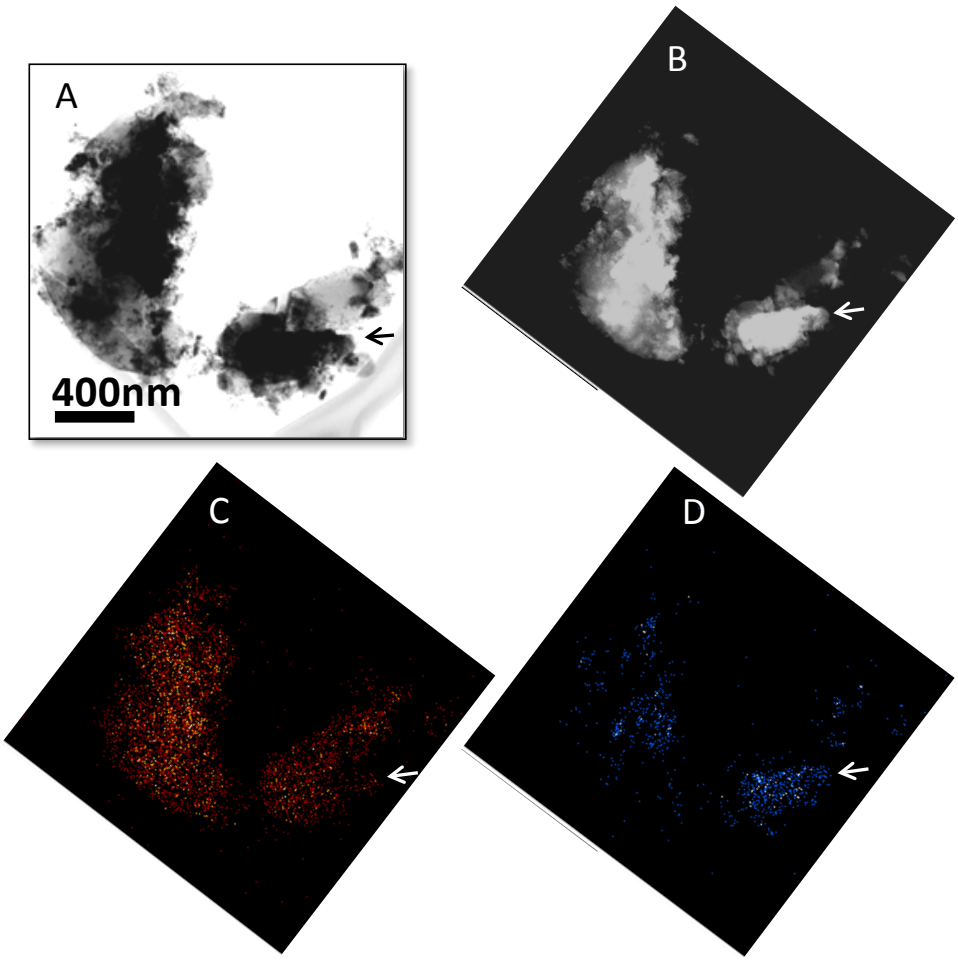

Figure 4.10: STEM - BF image (A) and STEM - HAADF image of the mapped area (B) along with EDS elemental maps of Mg (C) and Ti (D) from a particle of MgH_2-Ti10 composite after 75 cycles showing uniform dispersion of Ti particles on Mg surface.

The surface area of the as-milled samples along with that of as received MgH_2 is shown in Table 4.1. The composite MgH_2-Fe5Ti5 has the highest surface area (40 m^2/g), which suggests very good dispersion of Fe and Ti particles on the surface of MgH_2.

STEM images coupled with EDS elemental mapping of MgH_2-Fe10, MgH_2-Ti10, MgH_2-Fe5Ti5 and MgH_2-(FeTi)10 before and after cycling are shown in Figures 4.7 through 4.14. These images along with many others which are not shown here were used to assess the degree of dispersion of the catalyst material in MgH_2 matrix. Figures 4.7-4.8 and 4.9-4.10 clearly show the excellent dispersion of Fe and Ti on MgH_2 particles before and after cycling. No region found throughout these samples with bare magnesium having no catalyst covering. The ternary MgH_2-Fe5Ti5 system was also uniformly dispersed by nanosized Fe and Ti particles as is evident in Figure 4.11. Figure 4.12 shows that Fe and Ti remain on the surface uniformly during cycling.

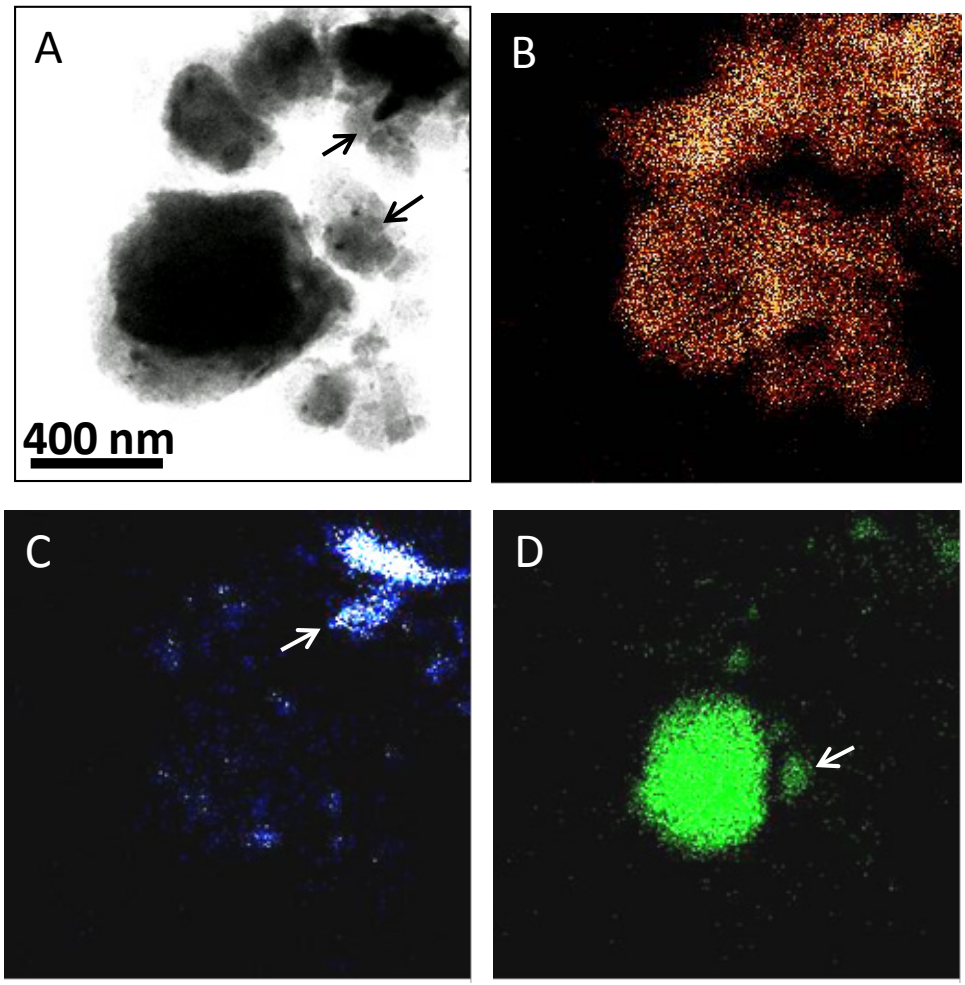

Figure 4.11: STEM - BF image (A) and EDS elemental maps of Mg (B), Fe (C) and Ti (D) from a particle of MgH_2-Fe5Ti5 composite showing uniform dispersion of Fe and Ti on Mg surface.

Our preliminary results showed a very poor dispersion of FeTi on MgH_2 matrix. In order to achieve a uniform dispersion of FeTi particles on the surface of MgH_2 particles, we added a small amount of purified multi-walled carbon nanotubes (MWCNTs) to the mixture. It has been shown that adding carbon nanotubes can improve the dispersion of the catalyst material on MgH_2 particles and also can improve the cycling stability of the ball-milled composites [118, 130, 134]. Figure 4.13 clearly shows how FeTi particles disperse on the surface of MgH_2 particles. Figure 4.14 shows that (FeTi) catalyst particles stay on the surface of magnesium hydride during cycling; and as also seen in XRD pattern of Figure 6b, the (FeTi) intermetallic does not decompose. However, it seems that the degree of dispersion is not as uniform as the other composites.

Figure 4.15 shows the results of image analysis on particle size distribution of the com-

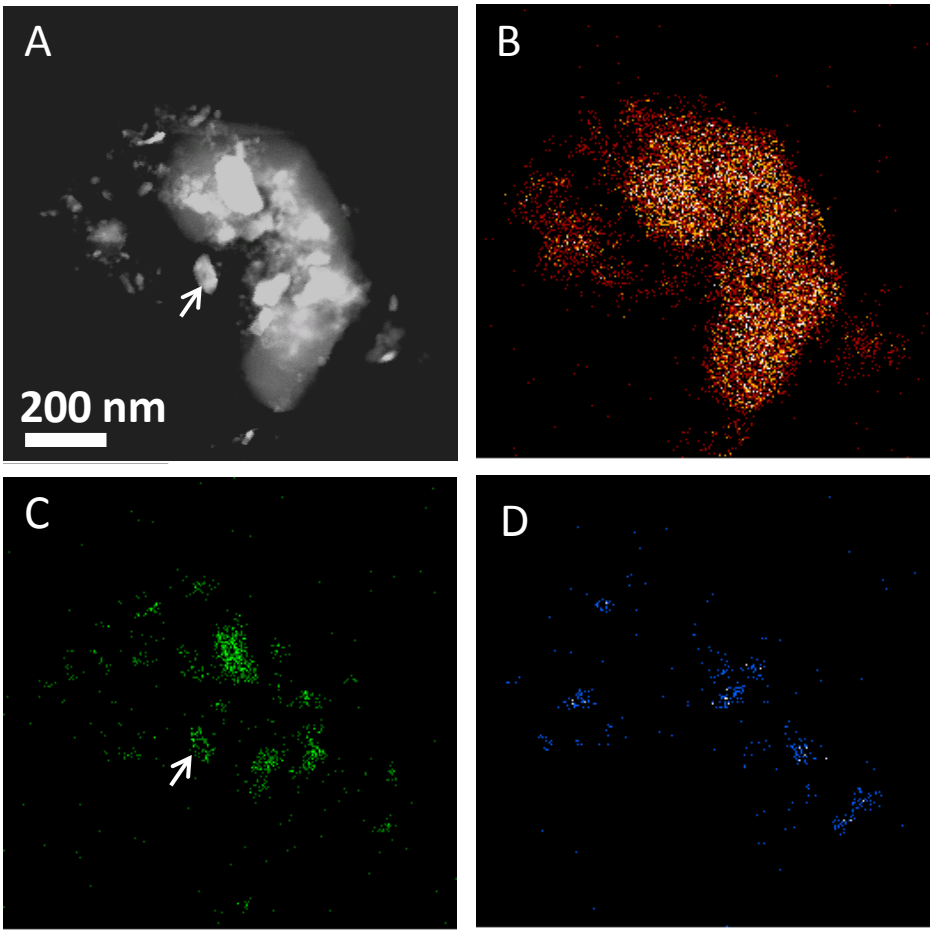

Figure 4.12: STEM - HAADF image of the mapped area (A) along with EDS elemental maps of Mg (B), Fe (C) and Ti (D) from a particle of MgH_2-Fe5Ti5 composite after 115 cycles showing uniform dispersion of Fe and Ti on Mg surface.

posites after cycling. Almost 47% of the particles of MgH_2-Fe-Ti composite are below 100 nm in size. This value is around 30% for all other post-cycled composites. The mean particle size for MgH_2-Fe5Ti5 is 200 nm which is the lowest compared to 326, 365 and 246 nm of MgH_2-Fe10, MgH_2-Ti10, and MgH_2-(FeTi)10, respectively. The smaller particle size in the latter is attributed to the presence of carbon nanotubes in this samples which can prevent agglomeration and sintering of the particles [134].

The JMA model fits the desorption curves quite well (with R-squared values of greater than 0.998). As an example, the fits for the desorption data of the MgH_2-Ti10 composite are shown in Figure 4.16. Figure 4.17 shows the rate constant (k) values as a function of cycle number for the studied composites. It clearly shows how the composites degrade through cycling. For sample MgH_2-(FeTi)10 the kinetics accelerates very quickly and is very fast at the beginning but immediately after the 5th cycles it starts degrading quite drastically. For

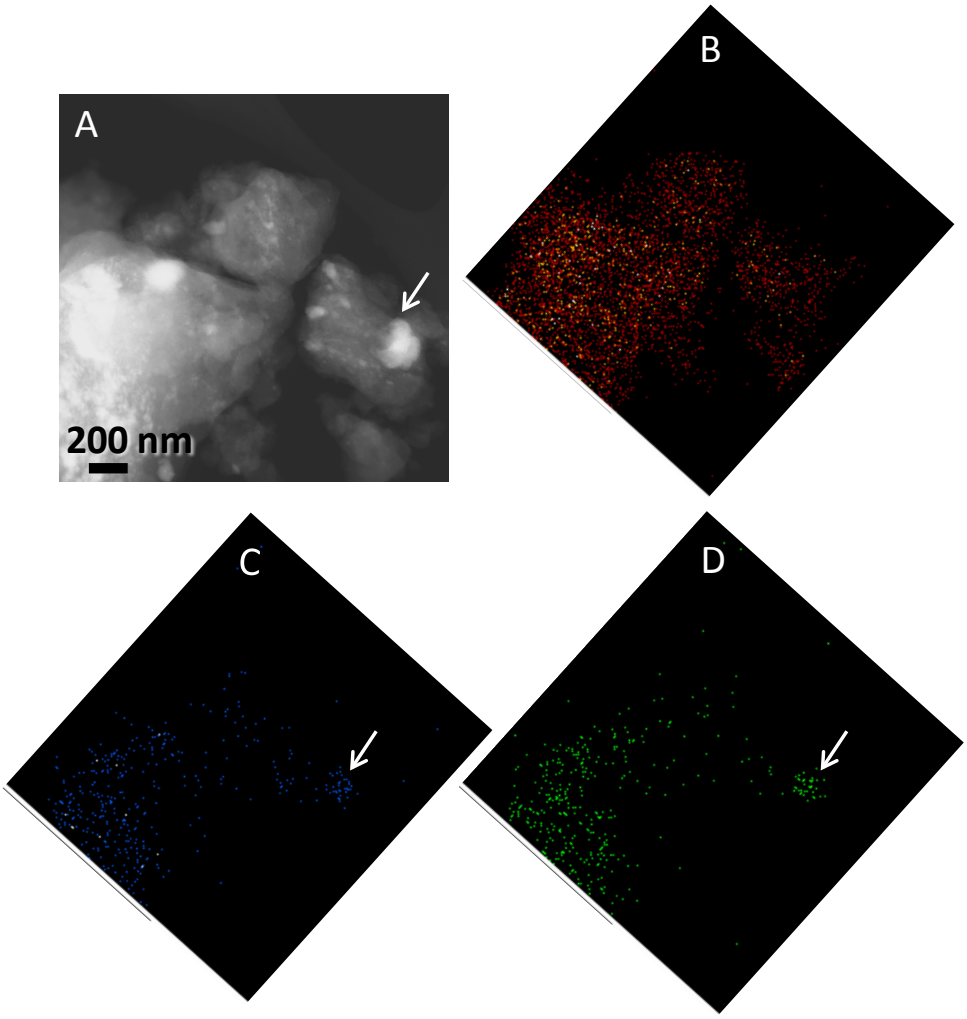

Figure 4.13: STEM - HAADF image (A) of the mapped area, EDS elemental maps of Mg (B), Fe (C) and Ti (D) from a particle of MgH_2-(FeTi)10 composite showing dispersion of FeTi particles on Mg surface. Fe and Ti appears on similar spots confirming their being in intermetallic compound form.

both MgH_2-Fe10 and MgH_2-Fe5Ti5 samples desorption kinetics accelerates up to 20 cycles and slows down slightly afterwards. The latter generally performs faster than the former. Sample MgH_2-Ti10 also accelerates at the very beginning and degrades quite quickly and overall shows the slowest kinetics. Again, it is apparent that after 40 cycles sample MgH_2-Fe5Ti5 becomes the fastest and the most stable mixture with minimal degradation. The trends in Figure 4.17 are in agreement with those of Figure 4.3.

We extracted the Avrami exponent values for different composites at different cycle numbers. For MgH_2-Ti10, as is also shown in Figure 4.16, during first few activation cycles the Avrami exponent $\eta \approx 3$. The JMA equation fits the rest of the cycles best when $\eta \approx 2$. For MgH_2-Fe10 and MgH_2-Fe5Ti5, the Avrami exponent remains constant at $\eta \approx 1.5$

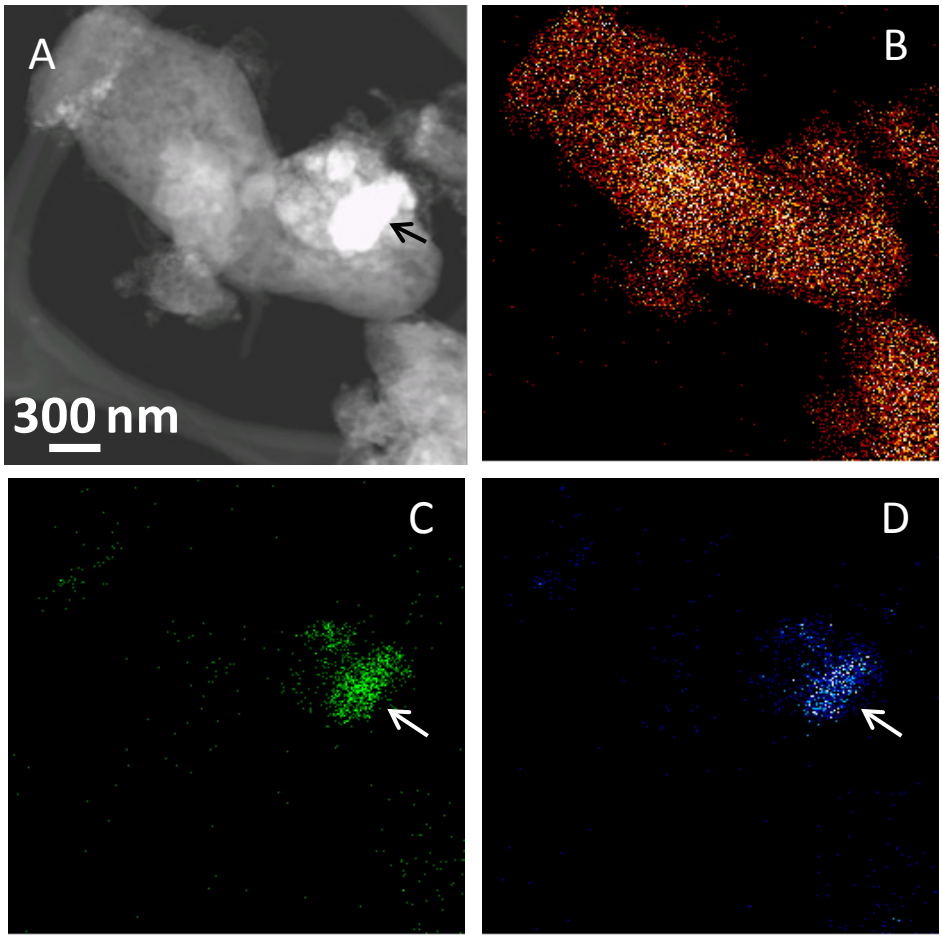

Figure 4.14: STEM - HAADF image of the mapped area (A) and EDS elemental maps of Mg (B), Fe (C) and Ti (D) from a particle of MgH_2-(FeTi)10 composite after 115 cycles showing dispersion of FeTi particles on Mg surface. Fe and Ti appears on similar spots confirming their intermetallic state.

during cycling. Finally, for MgH_2-(FeTi)10, in the first 5 activation cycles Avrami exponent changes from $\eta \approx 2.5$ to $\eta \approx 1.5$ quickly and it is constant for the rest of cycles. The rate limiting mechanisms will be further explained in the discussion section.

4.4 Discussion

Although being catalytically very active towards hydrogen dissociation (re-association), iron has not been practically used as a catalyst for magnesium hydride. During cycling at temperatures above 300 °C magnesium and Fe form the ternary hydride Mg_2FeH_6 of which the sorption is kinetically very slow. Here we performed the cycling test at 250 °C and showed that not only we can prevent formation of Mg_2FeH_6, the kinetics are satisfactorily fast; although degradation occurs to some degree during cycling. As shown in Figure 1,

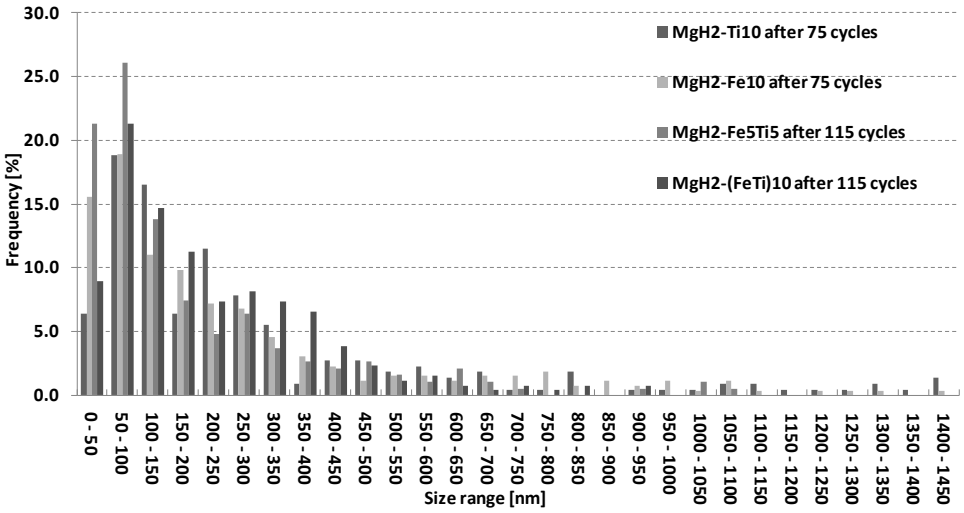

Figure 4.15: Particle size distribution of post cycled composites. The mean particle size for post cycled samples are 326, 365, 200, and 246 nm for MgH_2-Ti10, MgH_2-Fe10, MgH_2-Fe5Ti5 and MgH_2-(FeTi)10, respectively.

the composite of MgH_2 and Fe, with no prior activation, has a DSC desorption minimum of 170 °C lower than that of the as received magnesium hydride. Whereas, for MgH_2-Ti10 and MgH_2-(FeTi)10 composites the decrease in the desorption temperature is about 100 °C. However, a comparison between the performances of these catalysts can only be made during actual cycling after the activation step which occurs in the first few cycles. Figure 4.2 shows how degradation in MgH_2-Ti10 and MgH_2-(FeTi)10 is more pronounced compared to MgH_2-Fe10 and MgH_2-Fe5Ti5. This is shown more clearly in Figure 4.3 where time to reach 3.6 wt% of the maximum capacity is shown for various composites as a function of cycle number. However, since the composites have different hydrogen capacities, JMA rate constant values give a better means of comparing the kinetics of the composites as shown in Figure 4.17. Although MgH_2-Ti10 and MgH_2-(FeTi)10 start off faster they also degrade more dramatically than the other composites.

The composites with iron, with or without Ti, performed very similar in DSC desorption tests. Fe provides very low activation energy for hydrogen dissociation, so does Ti; however Ti unlike Fe has a high affinity for hydrogen atoms and hinders the diffusion of atomic hydrogen to the Mg matrix. Formation of titanium hydride through reaction of MgH_2 with Ti has been shown theoretically [74] and experimentally [68] before and was also found here from the XRD patterns in Figure 4.6 for both MgH_2-Ti10 and MgH_2-Fe5Ti5. Desorption and cycling data show that the composite with 10 at. % Ti degrades very fast.

Figures 4.7 to 4.17 show that the dispersion of catalyst material is in nanometric scale after milling and the catalyst materials stay on the surface of MgH_2 particles during subsequent cycling. Thus the most likely explanation for the fact that the sample with both

Fe and Ti performs better than the one with only Fe is that Fe acts as the catalytically active element and Ti is supposedly preventing the degradation of the kinetics through other mechanisms. We propose Ti hydride acts as a size control agent preventing the particle agglomeration and sintering of magnesium particles. Particle size distribution measurements and also kinetics analyses back this hypothesis as follows.

4.4.1 Kinetic analysis

BET surface area measurement coupled with TEM observation revealed a sub-micron structure of the composites. A nucleation and growth mechanism is expected for such microstructure. Sigmoidal sorption curves usually represent nucleation and growth mechanism. For absorption, no matter what type of catalyst we used, the CV model described in equation (2) applies to all the absorption curves with $\eta \approx 2$, which represents two-dimensional growth.

In analyzing the desorption curves, CV model did not fit our data, whereas JMA model described in equation (3) was able to fit the desorption curves with R-squared values of greater than 0.998. This is in accord with the findings by Barkhordarian et al. who, for Nb_2O_5 catalyzed MgH_2 composites, also found that absorbtion was accurately described by CV model while JMA model described the desorption [22]. Since the JMA kinetic model fits all the desorption curves quite satisfactorily, a graph of rate constant k as a function of cycle number is a very straightforward representation of the kinetics; since k is an equivalent measure for JMA kinetics with any Avrami exponent. By comparing the two graphs of time to reach 3.6 wt% of capacity and rate constant versus cycle number in Figures 4.3 and 4.17, a good agreement in the trends can be observed.

For MgH_2-Ti10, during first few cycles, the Avrami exponent is $\eta \approx 3$. The JMA equation fits the rest of the cycles best when $\eta \approx 2$. Avrami exponent of $2 < \eta < 4$ has been reported for pure magnesium and generally addition of catalyst results in reduction of the Avrami exponent by enabling instantaneous nucleation [28, 135, 136]. Here, as the catalyst is activated and nucleation sites are formed at the interface of the catalyst and MgH_2 particles, the change from $\eta \approx 3$ to $\eta \approx 2$ means a change from constant nucleation rate to constant nuclei number (instantaneous nucleation) and the rate limiting process for this composite is two dimensional - interface controlled. The degradation occurs maybe because of the detachment of titanium (hydride) particles from the surface. For MgH_2-Fe10 and MgH_2-Fe5Ti5, where there is a minimal activation required, the Avrami exponent remains constant at $\eta \approx 1.5$ during cycling which can be linked to three dimensional - diffusion controlled growth. For MgH_2-(FeTi)10 as FeTi activates and nucleation sites are formed at the interface between FeTi and MgH_2 particles and kinetics reaches its steady state, the Avrami exponent merges from $\eta \approx 2.5$ to $\eta \approx 1.5$. Again the rate limiting mechanism for this composite is three dimensional - diffusion controlled and the decrease in the Avrami

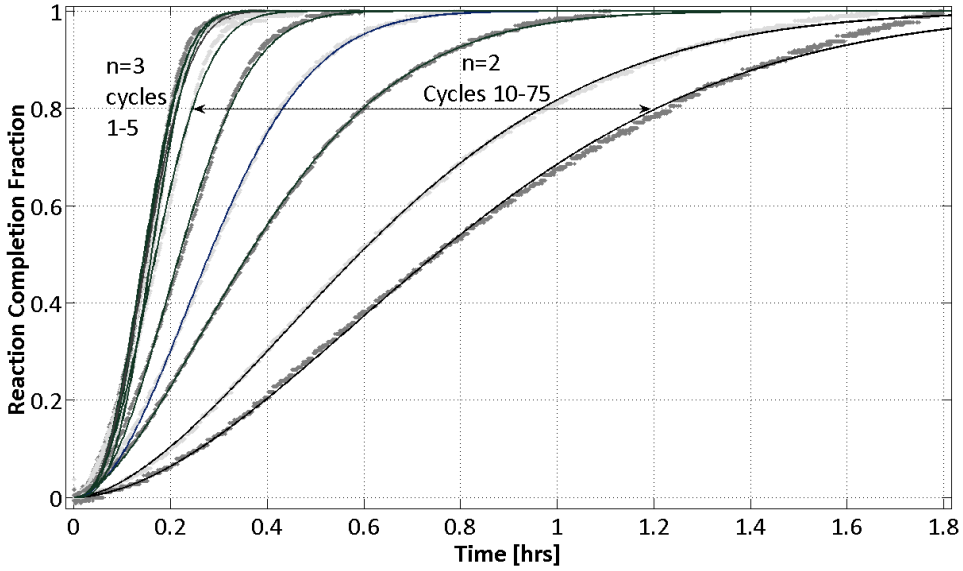

Figure 4.16: desorption kinetics data of MgH_2-Ti10 composite and corresponding JMA fits. The Avrami value is 3 for the first five cycles and it is 2 for the rest of cycles.

exponent is due to change from constant nucleation rate to constant neclei number. This is in accord with the literature, as already discussed in the introduction, that in order to be catalytically active, FeTi needs to be activated.

4.4.2 Role of Fe and Ti

From the BET surface area measurement of Table 1, MgH_2-Fe5Ti5 has the highest surface area (40 m^2/g) followed by MgH_2-Fe (20 m^2/g) and MgH_2-Ti (16 m^2/g). A high surface area can be interpreted as low particle size of MgH_2 and/or a large surface area enhancement by a high number of very small catalyst particles on the surface. By comparing the surface area data of the composites and that of as-milled MgH_2 it is concluded that Fe and Ti additions are responsible for the higher surface area or smaller particle size of MgH_2 particles. As a consequence, they must also have a better dispersion on the particles; this is confirmed by TEM observations in Figures 4.7- 4.14. According to particle size distribution measurement of Figure 15, after cycling at 250 °C, the mean particle size of MgH_2-Ti is smaller than that of MgH_2-Fe despite having a lower BET surface area at the start. This strongly supports our assumption of titanium hydride preventing the particles to agglomerate and or sinter together. MgH_2-Fe5Ti5 has the highest BET surface area in the as-milled state and still has the lowest average particle size (200 nm) after cycling; which further highlights the role of titanium hydride as a size control agent.

Addition of iron reduced the DSC desorption temperature of magnesium hydride (Figure 4.1). Also, it significantly reduced the activation energy for desorption of magnesium

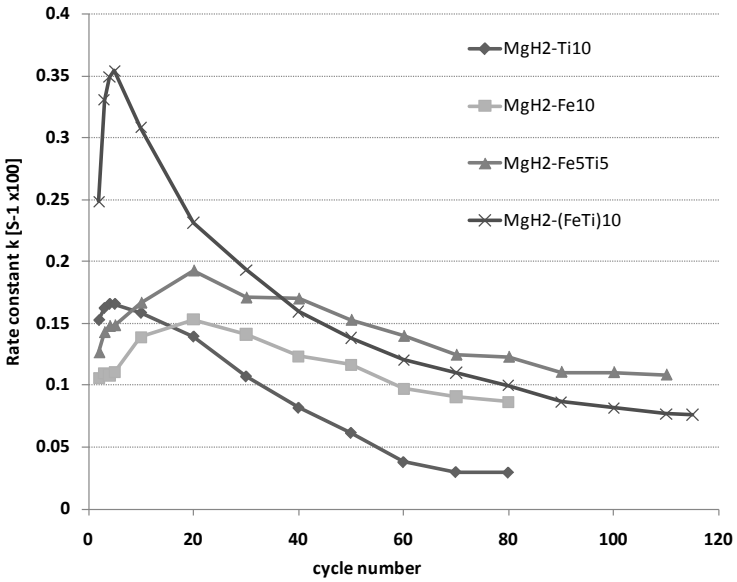

Figure 4.17: JMA rate constant (k) values as a function of cycle number

hydride, as evidenced by the Kissinger analysis shown in Figure 4.5. The activation energies for desorption of MgH_2-Fe10 and MgH_2-Fe5Ti5 are almost identical (92 and 97 kJ/mole respectively). For both composites, the desorption activation energies are higher after cycling. However for MgH_2-Fe10 composites, although undergoing less number of cycles (75 vs. 115), this value is higher at 119 kJ/mole compared to 108 for MgH_2-Fe5Ti5; which shows how the presence of Ti can effectively reduce degradation. This is further discussed in section 4.4.4.

4.4.3 Role of FeTi compound

As for MgH_2-(FeTi)10 sample, the heat of hydride formation of FeTi is -28 to -35 kJ/mol H_2 due to having multiple plateaus [137]. Based on Van't Hoff equation ($\ln \frac{P}{P_o} = \Delta H/RT - \Delta S/R$), the equilibrium pressure at 250 °C is greater than 9 bar. Thus, none of the FeTi hydrides are stable at the test conditions. Such dilute hydride phase can promote hydrogen uptake of magnesium [132, 138]. It should be noted that we clearly demonstrated with STEM/EDS combination that although we improved the dispersion of FeTi in the mixture, it was still inferior to that of Fe and Ti catalyzed composites. That might be what caused the fast deterioration of these composites. Nevertheless, this sample had low activation energy for desorption before cycling (92 kJ/mole) and the activation energy after cycling remains relatively low (111 kJ/mole). Thus, FeTi is suggested as a compound with high affinity toward hydrogen dissociation. There is a need for a special treatment to have nanosized FeTi uniformly and dispersed on the matrix particles.

4.4.4 Synergy of Fe and Ti

The values for activation energies of the three different composites, except MgH_2-Ti10, obtained using the Kissinger analysis shown in Figure 4.5 are very close. This also confirms a similarity in desorption rate controlling steps despite the difference in the measured sorption rates. The difference between activation energies for MgH_2-Fe10 and MgH_2-Ti10 before and after cycling is much larger (2-3 times) than the difference due to milling; that is between the as-received and the as-milled MgH_2 ($\sim$11 kJ/mol), whereas for MgH_2-Fe5Ti5 the difference between activation energies before and after cycling is exactly 11 kJ/mol. This shows that for the Fe + Ti mixture only the pure milling-induced effect is lost after cycling, which is quite compelling evidence for the 'synergetic effect' of Ti and Fe. Fe catalyzes hydrogen re-association while Ti prevents sintering and they both need to be present for either of them to be able to perform their designated function.

4.5 Summary

Co-milling of MgH_2 with Fe and Ti or FeTi does not change the magnesium hydride heat of formation but can substantially improve both desorption and absorption kinetics and lower the desorption temperature from that of pure MgH_2. For the composites with elemental Fe addition the shift in desorption peak was as high as 170 °C. We examined the cycling stability of all the studied composites. Except for the composites containing elemental Fe, a few sorption cycles are needed for the composites to fully activate the catalysts at 250 °C. Although the composites with only Fe or with Fe and Ti performed identically in DSC test after milling, they acted quite differently during cycling. We showed that a Fe + Ti mixture can synergistically catalyze the sorption of MgH_2: Fe acts as a very strong catalyst towards hydrogen sorption while Ti by forming titanium hydride acts as size control agent by preventing the agglomeration and sintering of Mg particles during sorption cycles. Using JMA kinetics model it was shown that for all the catalyst additives except titanium, the rate-limiting mechanism for desorption is three dimensional - diffusion controlled growth. For the composite containing Ti, the rate-limiting mechanism is two dimensional interface controlled growth. Fe, Ti and FeTi all have high catalytic activity towards hydrogen sorption. Although addition of Fe results in the finest and the most uniform dispersion on MgH_2 particles during milling, as evidenced by high angle annular dark field (HAADF) STEM imaging and EDS maps, (FeTi) initially shows higher sorption kinetics. As a dilute hydride phase, FeTi can promote hydrogen uptake of magnesium. In MgH_2-Fe5Ti5 composite synergy of Ti as a hydride former metal that can act as a size control agent and Fe as a strong catalyst results in a very stable hydrogen storage material with fast kinetics.

5

Conclusions

In my research I focused on accelerating the kinetics of MgH_2 sorption through addition of catalysts. Rather than looking for elemental metallic catalysts, I tried to combine existing catalysts in a way they can enhance the kinetics synergistically. First, I examined the role of a combination of SWCNTs and metallic nanoparticles on the hydrogen desorption properties of MgH_2 powders using high energy co-milling for various durations. Similarly, a bi-metallic Fe-Ti catalyst for magnesium hydride is introduced; where for the Fe + Ti mixture only the pure milling-induced effect is lost after cycling. Fe catalyzes hydrogen re-association while Ti prevents sintering and they both need to be present for either of them to be able to perform their designated function.

SWCNT-metallic nanoparticle additions catalyze the desorption of hydrogen, lowering the onset temperature by more than 30 °C over those of identically milled pure MgH_2 powders. However, co-milling for longer than one hour, degrades this effect, essentially yielding a similar sorption performance in the pure and the composite powders. Using Raman spectroscopy and HRTEM analysis, I showed that a significant portion of SWCNTs do survive up to 1 hour of milling, though becoming broken and defective in the process. At longer milling times the SWCNTs are completely destroyed and the enhancement is largely lost despite the continued presence of the metallic particles. X-ray diffraction analysis of the α-MgH_2 grain size and strain, and laser scattering analysis of the α-MgH_2 particle size, indicates that the addition of the SWCNT-metallic nanoparticles does not appreciably affect these parameters during milling. Cryo-stage TEM analysis confirmed that the majority of the hydride powder particles were polycrystalline, with nanoscale grain sizes. TEM also revealed that the larger hydride crystallites are multiply twinned.

Ozawa and Kissinger constant heating rate analysis conclusively demonstrated that in the optimum processed condition (1hour co-milled) the activation energy for hydrogen desorption is the lowest. Through the process of elimination it can be concluded that the catalytic effect of the SWCNTs is a result of one or a combination of the following effects: During mechanical milling the SWCNTs penetrate the thin surface hydroxide shell and act

as "hydrogen pumps"; or the surface dispersed and damaged SWCNTs reduce the high activation energy of hydrogen re-association on the MgH_2 surface.

Furthermore, I detailed the hydrogen sorption cycling performance of SWCNT-magnesium hydride nanocomposites. The SWCNT covered MgH_2 displays a fundamentally different sorption cycling behavior compared to the baseline, though the activation energies for desorption are roughly identical. The kinetics of the baseline powder rapidly degrade, where by sorption cycle 10 it takes nearly 84 minutes to absorb 4wt.% hydrogen and over 6 hours to desorb this quantity. Conversely the nanocomposites display a remarkable kinetic stability. At cycle 10 the time to absorb 4wt.% hydrogen is 7 minutes, while the time to desorb is 80 minutes. Even at cycle 35 the time to absorb is only 14 minutes, while the time to desorb is right at 2 hours. A more aggressive (in terms of variation of the sorption pressure from the plateau pressure) sorption regime allowed SWCNT covered MgH_2 to be tested up to 105 absorption desorption cycles with only minor kinetic degradation.

TEM analysis confirms that nanocomposite microstructure stabilizes the MgH_2 particle size during cycling. At the onset of cycling the mean diameters of the SWCNT covered hydride and of the baseline are 246 and 220 nm, respectively. After 10 cycles the baseline MgH_2 powders sinter/agglomerate, becoming microns in scale. However the mean diameter of the SWCNT covered particles increases to only 294 nm after 10 cycles, and to 369 nm after 35 cycles. TEM analysis and Raman spectroscopy confirm that even after 35 cycles the hydride remains covered by the SWCNTs and the amorphous carbon.

Co-milling of MgH_2 with Fe and Ti or FeTi does not change the magnesium hydride heat of formation but can substantially improve both desorption and absorption kinetics and lower the desorption temperature from that of pure MgH_2. For the composites with elemental Fe addition the shift in desorption peak was as high as 170 °C. I examined the cycling stability of all the studied composites. Except for the composites containing elemental Fe, a few sorption cycles are needed for the composites to fully activate the catalysts at 250 °C. Although the composites with only Fe or with Fe and Ti performed identically in DSC test after milling, they acted quite differently during cycling. I showed that a Fe + Ti mixture can synergistically catalyze the sorption of MgH_2. By measuring the activation energies of the ternary Mg-Fe-Ti composite and that of individual binary baseline composites a compelling evidence for the 'synergetic effect' of Ti and Fe was found. Fe catalyzes hydrogen re-association while Ti prevents sintering and they both need to be present for either of them to be able to perform their designated function.

Using JMA kinetics model it was shown that for all the catalyst additives except titanium, the rate-limiting mechanism for desorption is three dimensional - diffusion controlled growth. For the composite containing Ti, the rate-limiting mechanism is two dimensional interface controlled growth. Fe, Ti and FeTi all have high catalytic activity towards hydro-

gen sorption. Although addition of Fe results in the finest and the most uniform dispersion on MgH_2 particles during milling, as evidenced by high angle annular dark field (HAADF) STEM imaging and EDS maps, (FeTi) initially shows higher sorption kinetics. As a dilute hydride phase, FeTi can promote hydrogen uptake of magnesium. In MgH_2-Fe5Ti5 composite synergy of Ti as a hydride former metal that can act as a size control agent and Fe as a strong catalyst results in a very stable hydrogen storage material with fast kinetics.

Bibliography

[1] Züttel A. Materials for hydrogen storage. Mater today. 2003;6:24–33.

[2] Christmann K. Interaction of hydrogen with solid surfaces. Surf Sci Rep. 1988;9(1-3):1 – 163.

[3] Ogden J. Developing an infrastructure for hydrogen vehicles: a Southern California case study. Int J Hydrogen Energy. 1999;24(8):709–730.

[4] Analysis of the Transition to a Hydrogen Economy and the Potential Energy Infrastructure Requirements. Washington, DC: U.S. Department of Energy; 2007. Draft v.5-11-07.

[5] Darkrim F, Malbrunot P, Tartaglia G. Review of hydrogen storage by adsorption in carbon nanotubes. Int J Hydrogen Energy. 2002;27:193–202.

[6] Hirscher M, Becher M, Haluska M, Zeppelin F, Chen X, Dettlaff-Weglikowska U, et al. Are carbon nanostructures an efficient hydrogen storage medium? J Alloys Compds. 2003;356–357:433–437.

[7] Sakintuna B, Lamari-Darkrim F, Hirscher M. Metal hydride materials for solid hydrogen storage: A review. Int J Hydrogen Energy. 2007 6;32(9):1121–1140.

[8] Hirscher M, Becher M. Hydrogen storage in carbon nanotubes. J Nanosci Nanotech. 2003;3(1-2):3–17.

[9] Hoffman KC, Reilly JJ, Salzano FJ, Waide CH, Wiswall RH, Winsche WE. Metal hydride storage for mobile and stationary applications. Int J Hydrogen Energy. 1976;1(2):133–151.

[10] Buschow KHJ, Bouten PCP, Miedema AR. Hydrides formed from intermetallic compounds of two transition metals: a special class of ternary alloys. Rep Prog Phys. 1982;45(9):937.

[11] Gross KJ. Intermetallic Materials for Hydrogen Storage. University of Fribourg. Fribourg; 1998.

[12] Zaluski L, Zaluska A, Str JO. Nanocrystalline metal hydrides. J Alloys Compd. 1997;253-254:70 – 79.

[13] Klassen T. Nanocrystalline light metal hydrides for hydrogen storage. In: Hannink RHJ, Hill AJ, editors. Nanostructure Control of Materials. Woodhead Publishing Limited; 2006. p. 266Ű302.

[14] Barkhordarian G, Klassen T, Bormann R. Effect of Nb_2O_5 content on hydrogen reaction kinetics of Mg. J Alloys Compd. 2004 2/11;364(1-2):242–246.

[15] Lennard-Jones JE. Processes of adsorption and diffusion on solid surfaces. Trans Faraday Soc. 1932;28:333–359.

[16] Nørskov JK, Lang ND. Effective-medium theory of chemical binding: Application to chemisorption. Phys Rev B. 1980;21(6):2131–2136.

[17] Kissinger H. Reaction kinetics in differential thermal analysis. Anal Chem. 1967;29:1702–1706.

[18] Doyle CD. Series Approximations to the Equation of Thermogravimetric Data. Nature. 1965;207:290–291.

[19] Ozawa T. A new method of analysing thermogravimetric data. Bull Chem Soc Jpn. 1965;38(11):1881–1886.

[20] Ozawa T. Estimation of activation energy by isoconversion methods. Thermochim Acta. 1992;203:159–165.

[21] Martin M, Gommel C, Borkhart C, Fromm E. Absorption and desorption kinetics of hydrogen storage alloys. J Alloys Compd. 1996;238(1-2):193–201.

[22] Barkhordarian G, Klassen T, Bormann R. Kinetic investigation of the effect of milling time on the hydrogen sorption reaction of magnesium catalyzed with different Nb_2O_5 contents. J alloys compd. 2006;407(1-2):249–255.

[23] Fernandez J, Sanchez C. Rate determining step in the absorption and desorption of hydrogen by magnesium. J Alloys Compd. 2002;340(1-2):189–198.

[24] Rudman PS. Hydriding and dehydriding kinetics. J Less Common Met. 1983;89(1):93 – 110.

[25] Mintz M, Zeiri Y. Hydriding kinetics of powders. J Alloys Compd. 1995;216(2):159–175.

[26] Avrami M. Granulation Phase Change and Microstructure, Kinetics of Phase Change III. J Chem Phys. 1941;9:177–184.

[27] Burbelko A KW Fraś E. About Kolmogorov's statistical theory of phase transformation. Mater Sci Eng A. 2005;413:429–434.

[28] Vittori Antisari M, Aurora A, Gattia DM, Montone A. On the nucleation step in the Mg-MgH_2 phase transformation. Scr Mater. 2009;61:1064–1067.

[29] Pineda E, Crespo D. Microstructure development in Kolmogorov, Johnson-Mehl, and Avrami nucleation and growth kinetics. Phys Rev B. 1999;60(5):3104–3112.

[30] Kempen A, Sommer F, Mittemeijer E. Determination and interpretation of isothermal and non-isothermal transformation kinetics; the effective activation energies in terms of nucleation and growth. J Mate Sci. 2002;37(7):1321–1332.

[31] Zaluska A, Zaluski L, Str JO. Nanocrystalline magnesium for hydrogen storage. J Alloys Compd. 1999;288(1-2):217 – 225.

[32] Dornheim M, Doppiu S, Barkhordarian G, Boesenberg U, Klassen T, Gutfleisch O, et al. Hydrogen storage in magnesium-based hydrides and hydride composites. Scr Mater. 2007;56(10):841 – 846.

[33] Fecht HJ. Nanostructure formation by mechanical attrition. Nanostruct Mater. 1995;6(1-4):33 – 42.

[34] Koch CC. Synthesis of nanostructured materials by mechanical milling: problems and opportunities. Nanostruct Mater. 1997;9(1-8):13 – 22.

[35] Reilly J, Wiswall R. The reaction of hydrogen with alloys of magnesium and copper. Inorg Chem. 1967;6:2220–2223.

[36] Reilly J, Jr RW. The reaction of hydrogen with alloys of magnesium and nickel and the formation of Mg_2NiH_4. Inorg Chem. 1968;7:2254–2256.

[37] Bouten PCP, Miedema AR. On the heats of formation of the binary hydrides of transition metals. Journal of the Less Common Metals. 1980;71(1):147 – 160.

[38] Schlapbach L, editor. Hydrogen in Intermetallic Compounds I, Electronic, Thermodynamic, and Crystalline Properties, Preparation. vol. I of Topics in Applied Physics. Berlin: Springer-Verlag; 1988.

[39] Vajo J, Mertens F, Ahn C, Jr RB, Fultz B. Altering hydrogen storage properties by hydride destabilization through alloy formation: LiH and MgH_2 destabilized with Si. J Phys Chem B. 2004;108:13977–13983.

[40] Kondo T AMSY Shindo K. Microstructural and hydrogen absorption -desorption properties of MgTiFe0.92Mn0.05 composites prepared by mechanical milling. J Alloys Compd. 2004;375:283–291.

[41] Kondo T SY Shindo K. Dependence of hydrogen storage characteristics of MgTiFe0.92Mn0.08 composite on amount of TiFe0.92Mn0.08. J Alloys Compd. 2005;404-406:511–514.

[42] Mandal P, Srivastava O. Hydrogenation behavior of the new composite storage material Mg-xJ Alloys Compd. 1994;205:111–118.

[43] Vijay R, Sundaresanm R, Maiya M, Murthy S, Fu Y, Klein HP, et al. Characterization of Mg-xwtabsorbing material prepared by mechanical alloying. J Alloys Compd. 2004;382:283–295.

[44] Schulz R, Huot J, Liang G, Boily S, Lalande G, Denis MC, et al. Recent developments in the applications of nanocrystalline materials to hydrogen technologies. Mater Sci Eng A. 1999;267(2):240 – 245.

[45] Imamura H, Sakasai N, Fujinaga T. Characterization and hydriding properties of Mg-graphite composites prepared by mechanical grinding as new hydrogen storage materials. J Alloys Compd. 1997;253-254:34 – 37.

[46] Imamura H, Kusuhara M, Minami S, Matsumoto M, Masanari K, Sakata Y, et al. Carbon nanocomposites synthesized by high-energy mechanical milling of graphite and magnesium for hydrogen storage. Acta Mater. 2003;51(20):6407 – 6414.

[47] Huang ZG, Guo ZP, Calka A, Wexler D, Liu HK. Effects of carbon black, graphite and carbon nanotube additives on hydrogen storage properties of magnesium. J Alloys Compd. 2007;427(1-2):94 – 100.

[48] Huang ZG, Guo ZP, Calka A, Wexler D, Liu HK. Improvement in hydrogen cycling properties of magnesium through added graphite. Mater Lett. 2007;61(14-15):3163 – 3166.

[49] Shang CX, Guo ZX. Effect of carbon on hydrogen desorption and absorption of mechanically milled MgH_2. J Power Sources. 2004;129(1):73 – 80.

[50] Wu CZ, Wang P, Yao X, Liu C, Chen DM, Lu GQ, et al. Hydrogen storage properties of MgH_2/SWNT composite prepared by ball milling. J Alloys Compd. 2006;420(1-2):278 – 282.

[51] Chen D, Chen L, Liu S, Ma CX, Chen DM, Wang LB. Microstructure and hydrogen storage property of Mg/MWNTs composites. J Alloys Compd. 2004;372(1-2):231–237.

[52] Dehouche Z, Lafi L, Grimard N, Goyette J, Chahine R. The catalytic effect of single-wall carbon nanotubes on the hydrogen sorption properties of sodium alanates. Nanotechnol. 2005;16(4):402.

[53] Yao X, Wu C, Du A, Zou J, Zhu Z, Wang P, et al. Metallic and Carbon Nanotube-Catalyzed Coupling of Hydrogenation in Magnesium. J Am Chem Soc. 2007;129(50):15650–15654.

[54] Dresselhaus MS, Dresselhaus G, Saito R, Jorio A. Raman spectroscopy of carbon nanotubes. Phys Rep. 2005;409(2):47 – 99.

[55] Pierard N, Fonseca A, Colomer JF, Bossuot C, Benoit JM, Tendeloo GV, et al. Ball milling effect on the structure of single-wall carbon nanotubes. Carbon. 2004;42(8-9):1691 – 1697.

[56] Ákos Kukovecz, Kanyó T, Kónya Z, Kiricsi I. Long-time low-impact ball milling of multi-wall carbon nanotubes. Carbon. 2005;43(5):994 – 1000.

[57] Dehouche Z, Djaozandry R, Huot J, Boily S, Goyette J, Bose TK, et al. Influence of cycling on the thermodynamic and structure properties of nanocrystalline magnesium based hydride. J Alloys Compd. 2000;305(1-2):264 – 271.

[58] Dehouche Z, Klassen T, Oelerich W, Goyette J, Bose TK, Schulz R. Cycling and thermal stability of nanostructured MgH_2-Cr_2O_3 composite for hydrogen storage. J Alloys Compd. 2002;347(1-2):319 – 323.

[59] Huhn PA, Dornheim M, Klassen T, Bormann R. Thermal stability of nanocrystalline magnesium for hydrogen storage. J Alloys Compd. 2005;404-406:499 – 502.

[60] Schimmel HG, Huot J, Chapon LC, Tichelaar FD, Mulder FM. Hydrogen Cycling of Niobium and Vanadium Catalyzed Nanostructured Magnesium. J Am Chem Soc. 2005;127(41):14348–14354.

[61] Lillo-Ródenas MA, Guo ZX, Aguey-Zinsou KF, Cazorla-Amorós D, Linares-Solano A. Effects of different carbon materials on MgH_2 decomposition. Carbon. 2008;46(1):26–137.

[62] Dravid VP, Host JJ, Teng MH, Hwang BEJ, Johnson DL, Mason TO, et al. Controlled-size nanocapsules. Nature. 1995;374(10):602–602.

[63] Wang PJ, Fang ZZ, Ma LP, Kang XD, Wang P. Effect of SWNTs on the reversible hydrogen storage properties of $LiBH_4$-MgH_2 composite. Int J Hydrogen Energy. 2008;33(20):5611 – 5616.

[64] Fang ZZ, Kang XD, Dai HB, Zhang MJ, Wang P, Cheng HM. Reversible dehydrogenation of LiBH4 catalyzed by as-prepared single-walled carbon nanotubes. Scr Mater. 2008;58(10):922 – 925.

[65] Fang ZZ, Kang XD, Wang P, Cheng HM. Improved Reversible Dehydrogenation of Lithium Borohydride by Milling with As-Prepared Single-Walled Carbon Nanotubes. J Phys Chem C. 2008;112(43):17023–17029.

[66] Danaie M, Tao S, Kalisvaart P, Mitlin D. Analysis of deformation twins and the partially dehydrogenated microstructure in nanocrystalline magnesium hydride (MgH_2) powder. Acta Mater. 2010;58:3162–3172.

[67] Hanada N, Ichikawa T, Fujii H. Catalytic effect of nanoparticle 3d-transition metals on hydrogen storage properties in magnesium hydride MgH_2 prepared by mechanical milling. J Phys Chem B. 2005;109:7188–7194.

[68] Liang G, Huot J, Boily S, Nestea AV, Schulz R. Catalytic effect of transition metals on hydrogen sorption in nanocrystalline ball milled MgH_2 -Tm (Tm=Ti, V, Mn, Fe and Ni) systems. J Alloys Compd. 1999;292:247–252.

[69] Holtz R, Imam M. Hydrogen storage characteristics of ball-milled magnesium-nickel and magnesium-iron alloys. J Mater Sci. 1999;34:2655–2663.

[70] Kwon SN, Baek SH, Mumm DR, Hong SH, Song MY. Enhancement of the hydrogen storage characteristics of Mg by reactive mechanical grinding with Ni, Fe and Ti. Int J Hydrogen Energy. 2008;33:4586–4592.

[71] Welter JM, Rudman P. Iron catalyzed hydriding of magnesium. Scr Metall. 1982;16:285–286.

[72] Bogdanovic B, Reiser A, Schlichte K, Spliethoff B, Tesche B. Thermodynamics and dynamics of the Mg-Fe-H system and its potential for thermochemical thermal energy storage. J Alloys Compd. 2002;345:77–89.

[73] Zhou DW, Li SL, Varin RA, Peng P, Liu JS, Yang F. Mechanical alloying and electronic simulations of 2Mg-Fe mixture powders for hydrogen storage. Mater Sci Eng A. 2006;427(1-2):306 – 315.

[74] Zahiri B, Harrower C, Amirkhiz B, Mitlin D. Rapid and reversible hydrogen sorption in Mg-Fe-Ti thin films. Appl Phys Lett. 2009;95:103114.

[75] Guaoian L, Erde W, Shonshi F. Hydrogen absorption and desorption characteristics of mechanically milled Mg-35wt J Alloys Compd. 1995;223:111–114.

[76] Wang P, Wang AM, Ding BZ, Hu ZQ. Mg-$FeTi_{1.2}$ (amorphous) composite for hydrogen storage. J Alloys Compd. 2002;334(1-2):243 – 248.

[77] Reilly J, Jr RW. Formation and properties of titanium hydride. Inorg Chem. 1974;13:218–222.

[78] Zaluski L, Zaluska A, Tessier P, Ström-Olsen J. Hydrogen absorption by nanocrystalline and amorphous FeTi with palladium catalyst, produced by ball milling. J Mater Sci. 1996;31:695–698.

[79] Zaluski L, Tessier P ZASOJ Ryan DH. Amorphous and Nanocrystalline Fe-Ti prepared by ball milling. J Mater Res. 1993;8:3059–3068.

[80] Wang J, Ebner AD, Ritter JA. Kinetic Behavior of Ti-Doped $NaAlH_4$ When Cocatalyzed with Carbon Nanostructures. J Phys Chem B. 2006;110(35):17353–17358.

[81] Wu C, Wang P, Yao X, Liu C, Chen D, Lu GQ, et al. Effects of SWNT and Metallic Catalyst on Hydrogen Absorption/Desorption Performance of MgH_2. J Phys Chem B. 2005;109(47):22217–22221.

[82] Yao X, Wu C, Du A, Lu GQ, Cheng H, Smith SC, et al. Mg-Based Nanocomposites with High Capacity and Fast Kinetics for Hydrogen Storage. J Phys Chem B. 2006;110(24):11697–11703.

[83] Yoo Y, Tuck M, Kondakindi R, Seo CY, Dehouche Z, Belkacemi K. Enhanced hydrogen reaction kinetics of nanostructured Mg-based composites with nanoparticle metal catalysts dispersed on supports. J Alloys Compd. 2007;446-447:84 – 89.

[84] Kim KS, Cota-Sanchez G, Kingston CT, Imris M, Simard B, Soucy G. Large-scale production of single-walled carbon nanotubes by induction thermal plasma. J Phys D: Appl Phys. 2007;40(8):2375.

[85] Kissinger HE, Homer E. Reaction Kinetics in Differential Thermal Analysis. 1957;29:1702–1706.

[86] Klug HP, Alexander LE. X-ray Diffraction Procedures. 2nd ed. New York: John Wiley and Sons; 1974.

[87] Warren BE. X-Ray Studies of Deformed Metals. Prog Metal Phys. 1959;8:147–202.

[88] Vajeeston P, Ravindran P, Hauback BC, Fjellvåg H, Kjekshus A, Furuseth S, et al. Structural stability and pressure-induced phase transitions in MgH_2. Phys Rev B. 2006;73(22):224102.

[89] Grochala W, Edwards PP. Hydrides of The Chemical Elements for The Storage and Production of Hydrogen. Chem Rev. 2004;104:1283–1315.

[90] Bozhilov KN, II HWG, Dobrzhinetskaya L. Clinoenstatite in Alpe Arami Peridotite: Additional Evidence of Very High Pressure. Science. 1999;284(5411):128–132.

[91] Noe DC, Veblen DR. Mottled contrast in TEM images of mica crystals. Am Mineral. 1999;84(11-12):1932–1938.

[92] Tao Z, Geng H, Yu K, Yang Z, Wang Y. Effects of high-energy ball milling on the morphology and the field emission property of multi-walled carbon nanotubes. Mater Lett. 2004;58(27-28):3410 – 3413.

[93] Stander CM. Kinetics of decomposition of magnesium hydride. J Inorg Nucl Chem. 1977;39(2):221 – 223.

[94] Karty A, Grunzweig-Genossar J, Rudman PS. Hydriding and dehydriding kinetics of Mg in a Mg/Mg_2Cu eutectic alloy: Pressure sweep method. J Appl Phys. 1979;50(11):7200–7209.

[95] Rudman PS. Hydrogen-diffusion-rate-limited hydriding and dehydriding kinetics. J Appl Phys. 1979;50(11):7195–7199.

[96] Kelekar R, Giffard H, Kelly ST, Clemens BM. Formation and dissociation of MgH_2 in epitaxial Mg thin films. J Appl Phys. 2007;101(11):114311.

[97] Schober T. The Magnesium-Hydrogen System: Transmission Electron Microscopy. Nater Trans A. 1981;12:951–957.

[98] Zhdanov VP, Krozer A, Kasemo B. Kinetics of first-order phase transitions initiated by diffusion of particles from the surface into the bulk. Phys Rev B. 1993 May;47(17):11044–11048.

[99] Bloch J, Mintz MH. Kinetics and mechanisms of metal hydrides formation–a review. J Alloys Compd. 1997;253-254:529 – 541.

[100] Du AJ, Smith SC, Lu GQ. First-Principle Studies of the Formation and Diffusion of Hydrogen Vacancies in Magnesium Hydride. J Phys Chem C. 2007;111(23):8360–8365.

[101] Friedrichs O, Sanchez-Lopez JC, Lopez-Cartes C, Dornheim M, Klassen T, Bormann R, et al. Chemical and microstructural study of the oxygen passivation behaviour of nanocrystalline Mg and MgH_2. Appl Surf Sci. 2006;252(6):2334–2345.

[102] Ferre-Vilaplana A. Storage of Hydrogen Adsorbed on Alkali Metal Doped Single-Layer All-Carbon Materials. J Phys Chem C. 2008;112(10):3998–4004.

[103] Sagara T, Ganz E. Calculations of Dihydrogen Binding to Doped Carbon Nanostructures. J Phys Chem C. 2008;112(10):3515–3518.

[104] Wang L, Yang RT. Hydrogen Storage Properties of Carbons Doped with Ruthenium, Platinum, and Nickel Nanoparticles. J Phys Chem C. 2008;112(32):12486–12494.

[105] Chandrakumar KRS, Srinivasu K, Ghosh SK. Nanoscale Curvature-Induced Hydrogen Adsorption in Alkali Metal Doped Carbon Nanomaterials. J Phys Chem C. 2008;112(40):15670–15679.

[106] Shevlin SA, Guo ZX. High-Capacity Room-Temperature Hydrogen Storage in Carbon Nanotubes via Defect-Modulated Titanium Doping. J Phys Chem C. 2008;112(44):17456–17464.

[107] Liu W, Zhao YH, Li Y, Jiang Q, Lavernia EJ. Enhanced Hydrogen Storage on Li-Dispersed Carbon Nanotubes. J Phys Chem C. 2009;113(5):2028–2033.

[108] Contescu CI, Brown CM, Liu Y, Bhat VV, Gallego NC. Detection of Hydrogen Spillover in Palladium-Modified Activated Carbon Fibers during Hydrogen Adsorption. J Phys Chem C. 2009;113(14):5886–5890.

[109] Imamura H, Takesue Y, Tabata S, Shigetomi N, Sakata Y, Tsuchiya S. Hydrogen storage composites obtained by mechanical grinding of magnesium with graphite carbon. Chem Commun. 1999;p. 2277–2278.

[110] Bouaricha S, Dodelet JP, Guay D, Huot J, Boily S, Schulz R. Effect of carbon-containing compounds on the hydriding behavior of nanocrystalline Mg_2Ni. J Alloys Compd. 2000;307(1-2):226 – 233.

[111] Bouaricha S, Dodelet JP, Guay D, Huot J, Schulz R. Activation characteristics of graphite modified hydrogen absorbing materials. J Alloys Compd. 2001;325(1-2):245 – 251.

[112] Lillo-Ródenas MA, Aguey-Zinsou KF, Cazorla-Amoros D, Linares-Solano A, Guo ZX. Effects of Carbon-Supported Nickel Catalysts on MgH_2 Decomposition. J Phys Chem C. 2008;112(15):5984–5992.

[113] Ma LP, Dai HB, Liang Y, Kang XD, Fang ZZ, Wang PJ, et al. Catalytically Enhanced Hydrogen Storage Properties of $Mg(NH_2)_2$ + 2LiH Material by Graphite-Supported Ru Nanoparticles. J Phys Chem C. 2008;112(46):18280–18285.

[114] Gutowska A, Li L, Shin Y, Wang CMM, S LXH, C LJ, et al. Nanoscaffold Mediates Hydrogen Release and the Reactivity of Ammonia Borane. Angew Chem Int Ed. 2005;44(23):3578–3582.

[115] Balde CP, Hereijgers BPC, Bitter JH, de Jong KP. Facilitated Hydrogen Storage in NaAlH4 Supported on Carbon Nanofibers. Angew Chem Int Ed. 2006;45:3501–3503.

[116] Jongh PEd, Wagemans RWP, Eggenhuisen TM, Dauvillier BS, Radstake PB, Meeldijk JD, et al. The Preparation of Carbon-Supported Magnesium Nanoparticles using Melt Infiltration. Chem Mater. 2007;19(24):6052–6057.

[117] Gross AF, Vajo JJ, Van Atta SL, Olson GL. Enhanced Hydrogen Storage Kinetics of LiBH4 in Nanoporous Carbon Scaffolds. J Phys Chem C. 2008;112(14):5651–5657.

[118] Amirkhiz B, Danaie M, Mitlin D. The influence of SWCNT-metallic nanoparticle mixtures on the desorption properties of milled MgH_2 powders. Nanotechnol. 2009;20:204016.

[119] Berseth PA, Harter AG, Zidan R, Blomqvist A, Araújo CM, Scheicher RH, et al. Carbon Nanomaterials as Catalysts for Hydrogen Uptake and Release in $NaAlH_4$. Nano Lett. 2009;9(4):1501–1505.

[120] Wellons MS, Berseth PA, Zidan R. Novel catalytic effects of fullerene for $LiBH_4$ hydrogen uptake and release. Nanotechnol. 2009;20(20):204022.

[121] Rongeat C, Llamas-Jansa I, Doppiu S, Deledda S, Borgschulte A, Schultz L, et al. Determination of the Heat of Hydride Formation/Decomposition by High-Pressure Differential Scanning Calorimetry (HP-DSC). J Phys Chem B. 2007;111(46):13301–13306.

[122] Danaie M, Mitlin D. TEM analysis and sorption properties of high-energy milled MgH_2 powders. J Alloys Compd. 2009;476(1-2):590 – 598.

[123] Borgschulte A, Gremaud R, Griessen R. Interplay of diffusion and dissociation mechanisms during hydrogen absorption in metals. Phys Rev B. 2008;78(9):094106.

[124] Dinh LN, Cecala CM, Leckey JH, Balooch M. The effects of moisture on LiD single crystals studied by temperature-programmed decomposition. J Nucl Mater. 2001;295(2-3):193 – 204.

[125] Wan X, Markmaitree T, Osborn W, Shaw LL. Nanoengineering-Enabled Solid-State Hydrogen Uptake and Release in the $LiBH_4$ Plus MgH_2 System. J Phys Chem C. 2008;112(46):18232–18243.

[126] Zaluska A, Zaluski L, Ström-Olsen J. Structure, catalysis and atomic reactions on the nano-scale: a systematic approach to metal hydrides for hydrogen storage. Appl Phys A: Mater Sci Process. 2001;72:157–165.

[127] Pozzo M, Alfe D. Hydrogen dissociation and diffusion on transition metal (Ti, Zr, V, Fe, Ru, Co, Rh, Ni, Pd, Cu, Ag)-doped Mg(0001) surfaces. Int J Hydrogen Energy. 2009;34:1922–1930.

[128] Jin SA, Shim JH, Ahn JP, Cho Y, Yi KW. Improvement in hydrogen sorption kinetics of MgH_2 with Nb hydride catalyst. Acta Mater. 2007;55:5073–5079.

[129] Zahiri B, Amirkhiz B, Danaie M, Mitlin D. Bimetallic Fe-V catalyzed magnesium films exhibiting rapid and cycleable hydrogenation at 200°C. Appl Phys Lett. 2010;96:013108.

[130] Aminorroaya S, Liu H, Chob Y, Dahle A. Microstructure and activation characteristics of Mg-Ni alloy modified by multi-walled carbon nanotubes. Int J Hydrogen Energy. 2010;35:4144–4153.

[131] Dutta K, Mandal P, Ramakrishna K, Srivastava O. The synthesis and hydrogenation behaviour of some new composite storage materials: Mg-x wt.% FeTi(Mn) and La_2Mg_{17}-x wt.% $LaNi_5$. Int J Hydrogen Energy. 1994;19:253–257.

[132] Kalisvaart WP, Harrower CT, Haagsma J, Zahiri B, Luber EJ, Ophus C, et al. Hydrogen storage in binary and ternary Mg-based alloys: A comprehensive experimental study. Int J Hydrogen Energy. 2010 3;35(5):2091–2103.

[133] Rudman P. Hydriding and dehydriding kinetics. J Less Common Met. 1983;89:93–100.

[134] Amirkhiz B, Danaie M, Barnes M, Simard B, Mitlin D. Hydrogen sorption cycling kinetic stability and microstructure of single-walled carbon nanotube (SWCNT) magnesium hydride (MgH_2) nanocomposites. J Phys Chem C. 2010;114:3265–3275.

[135] Huot J, Liang G, Boily S, Neste AV, Schulz R. Structural study and hydrogen sorption kinetics of ball-milled magnesium hydride. J Alloys Compd. 1999;293–295(495–500).

[136] Bazzanella N, Checchetto R, Miotello A. Catalytic effect on hydrogen desorption in Nb-doped microcrystalline MgH_2. Appl Phys Lett. 2004;85:5212–5214.

[137] Alefeld G, Völkl J. Topics in applied physics. In: Hydrogen in metals I - basic properties. vol. 28. Springer-Verlag; 1978. p. 266–273.

[138] Pasturel M, Wijngaarden R, Lohstroh W, Schreuders H, Slaman M, B BD, et al. Influence of the chemical potential on the hydrogen sorption kinetics of Mg2Ni/TM/Pd (TM=transition metal) Trilayers. Chem Mater. 2007;19(3):624–633.